AD A
097187

⑫ **LEVEL** *II*

RADC-TR-80-368
Final Technical Report
January 1981

ADVANCED WAVEFRONT SENSOR CONCEPTS

Adaptive Optics Associates, Inc.

J. K. Bowker   L. Schmutz
J. Feinleib   M. Shao
          S. J. Tubbs

DTIC
S ELECTE D
APR 1 1981
B

ROME AIR DEVELOPMENT CENTER
Air Force Systems Command
Griffiss Air Force Base, New York 13441

81 4 01 023

AD A097187

DTIC FILE COPY

This report has been reviewed by the RADC Public Affairs Office (PA) and is releasable to the National Technical Information Service (NTIS). At NTIS it will be releasable to the general public, including foreign nations.

RADC-TR-80-368 has been reviewed and is approved for publication.

APPROVED: *[signature]*

PATRICK J. MARTONE, 1/Lt, USAF
Project Engineer

APPROVED: *[signature]*

FRANK J. REHM
Technical Director
Surveillance Division

FOR THE COMMANDER: *[signature]*

JOHN P. HUSS
Acting Chief, Plans Office

SUBJECT TO EXPORT CONTROL LAWS

If your address has changed or if you wish to be removed from the RADC mailing list, or if the addressee is no longer employed by your organization, please notify RADC.(OCSE) Griffiss AFB NY 13441. This will assist us in maintaining a current mailing list.

Do not return this copy. Retain or destroy.

REPORT DOCUMENTATION PAGE	READ INSTRUCTIONS BEFORE COMPLETING FORM

1. REPORT NUMBER	2. GOVT ACCESSION NO.	3. RECIPIENT'S CATALOG NUMBER
RADC-TR-80-368	AD-A097484	

4. TITLE (and Subtitle)	5. TYPE OF REPORT & PERIOD COVERED
ADVANCED WAVEFRONT SENSOR CONCEPTS	Final Technical Report. Jan - Sep 80
	6. PERFORMING ORG. REPORT NUMBER
	N/A

7. AUTHOR(s)	8. CONTRACT OR GRANT NUMBER(s)
J. K. Bowker M. Shao J. Feinleib S. J. Tubbs L. Schmutz	F30602-80-C-0063

9. PERFORMING ORGANIZATION NAME AND ADDRESS	10. PROGRAM ELEMENT, PROJECT, TASK AREA & WORK UNIT NUMBERS
Adaptive Optics Associates, Inc. 12 Prentiss Street Cambridge MA 02140	62702F 45061424 14

11. CONTROLLING OFFICE NAME AND ADDRESS	12. REPORT DATE
Rome Air Development Center (OCSE) Griffiss AFB NY 13441	Jan 81
	13. NUMBER OF PAGES
	183

14. MONITORING AGENCY NAME & ADDRESS(if different from Controlling Office)	15. SECURITY CLASS. (of this report)
Same	UNCLASSIFIED
	15a. DECLASSIFICATION/DOWNGRADING SCHEDULE N/A

16. DISTRIBUTION STATEMENT (of this Report)

Approved for public release; distribution unlimited.

17. DISTRIBUTION STATEMENT (of the abstract entered in Block 20, if different from Report)

Same

18. SUPPLEMENTARY NOTES

RADC Project Engineer: Patrick J. Martone, 1Lt, USAF (OCSE)

19. KEY WORDS (Continue on reverse side if necessary and identify by block number)

Adaptive Optics
Wavefront Sensors
Hartmann Sensor
Atmospheric Turbulence

20. ABSTRACT (Continue on reverse side if necessary and identify by block number)

The objective of this effort was to investigate advances in wavefront sensor technology for use in future adaptive optics systems. The improvements sought over presently developed adaptive optics systems are preliminary in the areas of componenet efficiency and sub-system complexity, since this would have potential for major operational simplicity and reduced cost.

(Cont'd)

DD FORM 1473 EDITION OF 1 NOV 65 IS OBSOLETE

The concept under study in this effort is the Large Scale Integrated Imaging Irradiance (LSI^3) sensor. This is based on the Integrated Imaging Irradiance (I^3) sensor (U.S. Patent No. 4,141,652). The I^3 sensor is based on the Hartmann concept, but does not suffer from the optical alignment problems inherent to previously developed Hartmann sensors. Another of the major advantages of the LSI^3 sensor over other Hartmann sensors (including the previously developed I^3-sensor) is that the LSI^3 sensor utilizes the full aperture of the system in dividing the input photon flux into the respective quadrants which results in better diffraction - limited resolution. The LSI^3 sensor is based on an optical system that is independent of the number of sub-apertures selected.

The major tasks of this study included the conceptual design of a small version (approximately 20 channels), a large scale (approximately 200 channels) wavefront sensor, and the evaluation of the expected performance, complexity, and cost of these prototype models. During the course of the study, major design modifications were introduced which appeared to greatly improve the performance of the LSI^3 concept of the I^3 sensor, and finally showed a significant performance improvement over previously developed wavefront sensors including the shearing interferometer. At the same time, these design changes appear to have greatly reduced the complexity of the electronic processing required, simplified the optical system to a few critical elements and allowed large diode array detectors such as photomultipliers to be utilized without a significant performance loss.

The result of these design advancements is a new wavefront sensor (LSI^3) which could provide cost and performance advances for future adaptive optics systems.

Accession For	
NTIS GRA&I	☑
DTIC TAB	☐
Unannounced	☐
Justification	
By	
Distribution/	
Availability Codes	
Dist	Avail and/or Special
A	

SUMMARY

This final report describes the results of a nine month effort by Adaptive Optics Associates, Inc. (AOA) on Rome Air Development Center (RADC) Contract F30602-80-C-0063 for an "Advanced Wavefront Sensor Concepts" (AWSC) study. The objective of this study was to investigate advances in wavefront sensor technology for use in future adaptive optics systems, and, in particular, to advance the technology over the Compensated Imaging System (CIS)[1] presently being developed for open space surveillance application. The improvements sought are primarily in the area of component efficiency and subsystem complexity, since this would have potential for major operational simplicity and reduced cost. The technical performance projected for CIS is near optimum and only small improvements, if any, were contemplated at the start of this program.

To meet the objectives of this program, AOA proposed to analyze and evaluate the design and performance of a new wavefront sensor concept based on a proprietary[2] sensor, the Integrated Imaging Irradiance (I^3) sensor, developed and tested under other Air Force programs[3,4]. The concept under study here will be referred to as the LSI^3, or Large Scale I^3, sensor throughout this report.[5]

The major tasks of this study included the conceptual design of a small version (approximately 20 channels) and a large scale (approximately 200 channels) wavefront sensor, and the evaluation of the expected performance, complexity and cost of these proto-type models. The study was undertaken using the baseline LSI^3 proposed. During the course of the study, major design modifications were introduced which appeared to greatly improve the performance of the LSI^3 concept over the I^3 sensor, and finally showed a significant performance improvement over that projected

for the CIS. At the same time, these design changes greatly reduced the complexity of the electronic processing required, simplified the optical system to a few critical elements and allowed large diode array detectors, instead of individual quantum detectors such as photomultipliers, to be utilized without a significant performance loss.

As a result of these design advancements, the AWSC investigation met all program objectives, and this final report describes in detail the design and analysis of a new wavefront sensor which could provide cost and performance advances for future CIS systems.

REFERENCES

1. References will be made available to qualified military and government agencies on request from RADC (OCSE) Griffiss AFB NY 13441.

2. U. S. Patent No. 4,141,652.

3. AFWL-TR-78-65.

4. Reference will be made available to qualified military and government agencies on request from RADC (OCSE) Griffiss AFB NY 13441.

5. Patent pending.

TABLE OF CONTENTS

LIST OF ILLUSTRATIONS

4

LIST OF TABLES

6

7

EVALUATION

The value and significance of this effort includes many design advancements incorporated in a new wavefront sensor (Large Scale Integrated Imaging Irradiance LSI^3) which could provide cost and performance advances for future adaptive optics systems.

The results of this effort are applicable to Electro-Optics Advanced Systems Analysis.

Applications of this Advanced Wavefront Sensor include future Compensated Imaging Systems for Space Defense applications, and laser beam control systems such as the Stragegic Laser Communications Uplink program.

PATRICK J. MARTONE, 1/Lt, USAF
Project Engineer

8

1.0 INTRODUCTION AND BACKGROUND

1.1 Compensated Imaging Wavefront Sensing Problem

The development of real-time wavefront sensing has produced three techniques of measurement: interferometric, successfully embodied in the shearing interferometer which measures phase shifts in the pupil; geometric, embodied in the Hartmann test, which measures wavefront tilts; and spread function analysis, which obtains the pupil phase distortion by Fourier transformations. The first of these has been completely developed by Itek under contract to RADC which produced the Real Time Atmospheric Correction (RTAC)[1], a 21-channel system. Later, after a design competition with Perkin Elmer, which espoused a Hartmann system under another CIS program, Itek developed a 250-channel digital sensor for CIS. Because of these contracts, other techniques have not been developed extensively.

The design contest between Itek Corporation and Perkin Elmer which knocked the Hartmann test out was won by Itek, in part because the Hartmann test was optically and electronically too sensitive to misalignment and drift -- so sensitive, in fact, that a system could not be demonstrated. The appreciation of these difficulties was the basis for the invention of the I^3 sensor, patented and developed by AOA[2].

The CIS wavefront sensing problem is severe because the targets are dim, large, complex and moving rapidly. In consequence, the sensor measurement must be insensitive to object shape, must be able to operate with as few as one photon/cycle on the average, and must provide a correction bandwidth as great as 1 kHz.

---

1. Reference will made available to qualified military and government agencies on request from RADC (OCSE) Griffiss AFB NY 13441.

2. U.S. Patent No. 4,141,652.

Target size and shape effect have been crucial in determining whether a sensor will work or not, and these have generally made adaptive function necessary in the design of sensors. For example, if the target subtends more resolution elements over its area than the system has subapertures, then the target will be resolved by the subapertures. The shearing interferometer signal visibility will drop and π phase error occurs due to interference effects. The classic Hartmann test will lose sensitivity, often dropping to zero, if the target has multiple bright spots. The shearing interferometer (SI) can adapt to these difficulties by decreasing the shear and reducing sensitivity. The Hartmann test cannot adapt and is vulnerable to object-induced failure.

The I^3 sensor, although based on the Hartmann test, uses an AC algorithm and, in essence, uses edge information as well as the broad radiant distribution. Thus, response becomes less dependent on object size and signal strength. The adaptive features of the proposed sensor are used to optimize sensitivity and to prevent performance anomalies such as those embodied by the dead zone of the dumbbell response of the Hartmann or by the visibility nulls with 2π ambiguity and π phase flips of the SI.

The LSI^3 sensor is a major advance of the I^3 sensor for applications requiring a large number of subaperture measurements. It embodies all of the optical efficiencies of the Hartmann sensor and the I^3 insensitivity to target shapes.

The major advantages are as follows.

- Fundamental performance improvement over the shearing interferometer by up to a factor of two for simple targets of all sizes and ranges.

- An optical system that is independent of the number of subapertures selected, unlike the I^3 sensor.

- An optical system that is independent of the detector configuration, unlike the I^3 sensor.

- An optical system design that can be used with pulsed or CW actively illuminated targets as well as passive illuminated targets.

- A versatile optimum processing algorithm that can be adapted to maximize performance for unusual target shapes.

- An electronic processor architecture that requires only four pipeline serial processors to service 256 subapertures, as opposed to 1024 parallel processors.

- A selection of three different intensified serial detector array configurations which would maintain an optical efficiency exceeding that projected for the current CIS and that are compatible with the pipeline processor.

- A system design that incorporates all the performance advantages in a small lightweight optical package using few components and simple to align.

- A system design with low component count, compact electronics processing package that promises high reliability.

These features will be discussed in detail in the following sections.

1.2 I^3 Sensor Concept

The I^3 sensor[1,2,3] is a wavefront sensing concept based on

---

1. Julius Feinleib et al., "The I^3 Sensor: A New Method for Real-Time Wavefront Mensuration," Proc. SPIE Tech. Symp. East, Washington, D.C.(1979).

2. J. K. Bowker et al., "I^3 Sensor Wavefront Performance," SPIE Vol 190 (1979).

3. L. E. Schmutz et al., "Experimental Performance of the I^3 Wavefront Sensor for Closed-Loop Adaptive Optics," Proc. SPIE Tech. Symp. East, Washington D.C. (1980).

the Hartmann technique. In the Hartmann test, the shape of an
optical wavefront is estimated by measuring the mean tilts
at each of a set of small subapertures in the pupil aperture,
and then fitting a smooth curve to the tilt samples. Dynamic
Hartmann sensors, designed to measure wavefront changes at rates
comparable to atmospheric turbulence variations, have been
attempted but have not succeeded due to severe problems of
optical alignment stability, and to a fairly high sensitivity to
image shape in cases where the source object is resolved by the
subaperture.

Ref. 1 (p.11) is an introduction to the I^3 sensor concept
and describes some of its performance advantages. Figure 1 is
a schematic of the concept and shows the changes from a basic
Hartmann technique. The two major innovations which make the
I^3 sensor a practical, high sensitivity wavefront measuring
technique are:

(1) the addition to the input wave of a local plane
wave which acts as an internal optical tilt reference, and

(2) a conical scan, or nutation modulation of the
combined signal and reference beam.

1.2.1 Optical reference. The use of a local reference
provides enormous flexibility in the design of a practical
measuring instrument. Once combined, the signal and reference
beams are equivalently affected by internal optical misalignments,
which might be due to thermally or vibrationally induced compo-
nent movement, or to finite specification tolerances of the
optical elements. In the subaperture image plane, tilts in the
input wavefront are given by the difference between the reference
and signal focal spot positions. The differential character of
the I^3 measurement is useful with any kind of position sensing
detector, be it a quad cell, lateral cell, CCD or diode array,
video imager, etc.

12
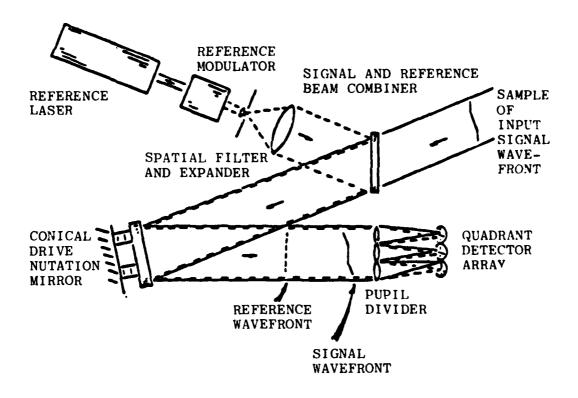
Figure 1. Simplified I^3 sensor optics.

13

1.2.2 Nutation. When coupled with the quadrant
detector configuration, nutation modulation permits the use
of some extremely powerful and efficient detection and processing
techniques. Several performance advantages can be obtained,
which include optimal SNR performance, AC carrier generation, and
the ability to discriminate between signal and background radia-
tion in the complex scenes.

Nutation modulation impresses an AC carrier on
the optical input power by utilizing spatial variations on the
image itself. It differs from both the AC shearing interfero-
meter and the chopped Hartmann type of system in that the input
photon flux is never interrupted by a chopped or rotating grating.
In those systems, uniform illumination from the object background
is modulated along with the object signal power which is limited
by field stops of the detector.
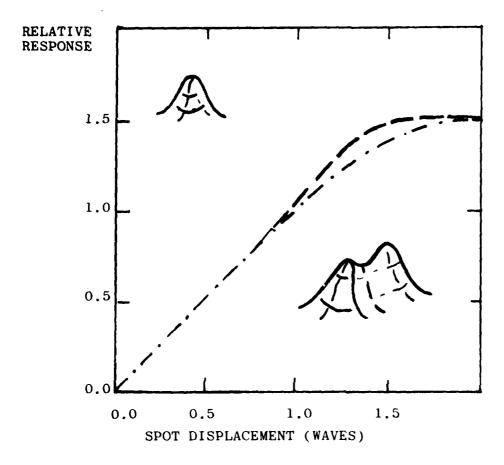
However, when nutation is used, uniform background
power is _not modulated at all_, since the relative power falling
on each quadrant of the detector is unchanged during the course of
a nutation cycle. In addition, locally generated radiation,
either from scattering or thermal sources, does not appear at the
AC carrier frequency. This has been found experimentally to have
very significant advantages, particularly when using infrared
(IR) sensitive detectors.

Another more subtle consequence of nutation
modulation is the ability of the I^3 sensor to operate with equal
facility using objects of either positive or negative contrast.
That is, the object may be a bright spot against a dark back-
ground _or_ a dark spot in a bright background. In both cases,
correct signs for the wavefront tilt response are retained (a
crucial result for closed-loop operation).

1.2.3 Image insensitivity. The unique features of
nutation modulation extend also to the way in which the I^3
sensor responds to complex shapes resolved by the subaperture,
which is a problem quite relevant to imaging systems. One
manifestation of the problem occurs in the change of the transfer
function of the sensor for different image shapes. In a closed-
loop system this amounts to changes in loop gain for different
input scenes, complicating the problem of obtaining unconditional
loop stability. For the shearing interferometer, image periodi-
cities related to the grating period cause significant signal
variations, while in simple quad Hartmann systems, a "dumbbell"
image, or pair of bright spots located in separate quadrants,
results in near-zero signal regardless of spot intensity.

The I^3 sensor responds to the slope of the image
edges, rather than to the centroid of the image power. In
a properly designed instrument, the edge slope of the subaperture
image is dominated by the point spread function of the subaper-
ture. That is, the I^3 sensor transfer function is determined by
the pupil of the instrument, rather than by the spatial extent
of the input image.

Figure 2 shows the response of the I^3 sensor to
two drastically differing image distributions. These results
are taken from extensive simulation, verified by systematic ex-
perimentation, already completed at AOA. The dashed line shows
the sensor response due to displacement of a Gaussian-shaped spot
along a quadrant detector axis. The quadrant detector is 2.25
spot radii square, with a nutation radius of one spot radius.
The broken line is the response to a pair of spots oriented at
45° to the quad detector axes, and displaced along the x-axis.
The spot shapes have the same Gaussian shapes, and the system
response is the same for both images until detector edge effects
become important at large displacements. Similar analysis for

Figure 2. Responsivity of the I^3 sensor to two different image plane intensity distributions. The results are obtained using a high level computer simulation developed by AOA which duplicates the I^3 processing steps as well as a variety of possible input optical distributions. The 2 distributions are a single circularly symmetric peak with Gaussian edges, chosen to emulate an unresolved image point, and a double-lobed "dumbbell" distribution having 3 times the lateral extent along the dumbbell axis and the single spot but with the same Gaussian edge slopes. The dumbbell is oriented 45° to the quad cell axis with one lobe in quadrant 1, the other in quadrant 3. The displacements occur in the +x direction and the outputs are seen to be essentially identical for both distributions.

other even more complex shapes show similar results: the I^3 sensor response has a very high degree of insensitivity to image shape.

1.2.4 Summary. The I^3 sensor has a large variety of operating characteristics that make it a very competitive wavefront sensing technique. There include the following.

(1) Fundamental signal-to-noise ratio (SNR) performance comparable to that of the AC shearing interferometer and the DC quad Hartmann; all three approach theoretically optimal performance limits.

(2) The internal reference in the I^3 sensor allows great flexibility in the detailed optical design of a specific instrument.

(3) With the use of proper electronic processing, nutation modulation provides an AC carrier in a highly efficient way, yields operation with both positive and negative contrast objects, and gives a very high degree of system gain insensitivity to object shape and extent. In addition, the nutation modulation technique does not chop a uniform background, which considerably reduces the dynamic range problems at the front end processing stages.

1.3 LSI^3 Sensor Concept

The LSI^3, which is the baseline system described in this study for a visible light sensor, is based on the I^3 sensor concept studied extensively for use in IR adaptive optics systems where a relatively small number of subaperture measurements are required for compensation of atmospheric turbulence effects. Although the LSI^3 sensor has a completely different and more efficient optical configuration, the processing algorithms and sensor behavior is much like that of the I^3 sensor. Therefore,

17

many of the sensor characteristics proven to be of importance for the I^3 sensor are projected to carry over into the LSI^3 performance. These characteristics obtained by analysis, simulation and experimental measurements are summarized briefly here and are described in detail in the final report of Reference 4. The important advantages of this system are the motivation for incorporating them into the LSI^3 sensor design.

1.4 Design Goals

As discussed in Section 1.1, any alternative technology to that currently employed in the CIS must retain high speed and must approach quantum limited sensitivity. However, if really large (e.g., greater than 200 subapertures) compensation systems are to be built, some alternative to fully parallel sensing and processing must be found.

The cost of expanding the current CIS in a parallel fashion is, no doubt, well studied. We have made similar estimates of the cost and complexity of constructing a completely parallel I^3 sensor, using the most current electronic technology. Assuming either a set of small PMT's at the input or an intensified quadrant detector, and employing some advanced processing components such as the Intel 2920 signal processing chip, the detection and processing stages would cost approximately $1,500 per channel. The channels would contain no analog circuitry requiring any adjustment, and would be relatively compact (perhaps one 3" X 5" PC board per processor). The cost for a large system is thus $300K for detection and processing alone.

There is another major cost component for large systems, and that is in the optics required for pupil division into the measurement subapertures. For a Hartmann-type system, even a

cleverly designed system becomes intricate and somewhat
sensitive (even using a referencing technique). In a parallel
shearing interferometer, the problem is one or precise regis-
tration of 800 individual detectors in the conjugate pupil
plane.

From these considerations, our design goals have
centered on the following.

(1) Eliminating the complex pupil division optics
which becomes increasingly cumbersome with scale.

(2) Employing a monolithic detection array to reduce
the problems of size, cost, and alignment sensitivities.

(3) Attempt a parallel/serial hybrid processing
scheme which eliminates the need for a strict processor per
channel correlation.

In the following section, a wavefront sensor design
which meets each of these criteria is presented. The detection
system is based on the use of intensified diode arrays which
also act as pupil dividers for the system. Furthermore, the
characteristics of the array elements are used as part of the
processing stage, so that only a single, fairly simple processor
would be required to operate a full 256 subaperture system. A
fivefold to tenfold cost reduction should be realized with this
approach, with complexity at the 256 subaperture level _less_ than
that for a 21 subaperture CIS.

1.5 Parallel/Serial System Design

Figure 3 is a simplified layout showing the basic
features of the proposed optical system. At the input to the
system, the input signal wavefront is combined with the locally
generated reference plane wave, giving the highly desirable
optical and electronic self-calibration capability. The

19

INPUT WAVEFRONT FROM TELESCOPE

REFERENCE
WAVEFRONT

GALVANOMETER NUTATION MIRRORS

INTENSIFIED
CCD ARRAYS

QUADRANT
DIVIDER

Figure 3. Simplified optical layout.

20
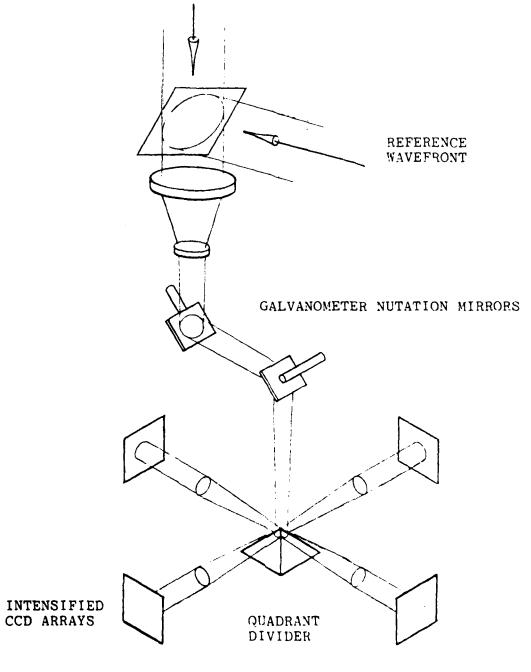
CAPTION FOR FIGURE 3

Figure 3.   Simplified optical layout for the proposed
            wavefront sensing system. The conventional
            Hartmann-type pupil divider and discrete
            quadrant detector array has been replaced
            by a quadrant divider and four monolithic
            detector arrays. The input wavefront is
            combined with a reference wave and passed
            through a pair of galvanometer mirrors,
            which impart the circular nutation. The
            primary focus occurs at the tip of the
            prismatic quadrant divider, which reflects
            the beam into four detector channels.
            Final lenses project the input pupil onto
            the detector array, which also acts as a
            pupil divider. The number of subapertures
            is determined solely by the number of
            detectors in each array; otherwise the
            optical arrangement is the same for any
            size system.

reference is modulated in the time domain so that it can be
discriminated from the signal. In order that shot noise from
the reference not degrade the system performance, the reference
is switched on for one nutation cycle out of every ten or more,
so that most time is spent observing signal power. In the sys-
tems which have already been constructed at AOA, a ratio of
about one reference cycle for every 32 signal cycles has been
used with good result.

The circular tilt or nutation modulation is provided by
a pair of sinusoidally driven resonant galvanometer mirrors
locked in phase quadrature. AOA has developed and operated
such systems at 10 kHz, which provides ample sampling rate to
give the required 1 kHz information bandwidth.

The innovations in this design occur in the next stage.
Instead of placing a quadrant detector in the image plane, a
prismatic quadrant divider is placed at the focus of the full
aperture. This element acts to simultaneously divide all sub-
aperture areas into four channels for detection and processing.

After the optical divider, the four quadrant beams are
collimated and fall onto four separate detector arrays. Because
the arrays are in a plane conjugate to the input pupil, the
individual detector elements behave as subaperture masks. This
is illustrated more directly in Figure 4. By projecting the
detector array pattern back through the optical system, it is
seen that each detector maps into an input subaperture.

For every subaperture there are four conjugate detec-
tors, one in each quadrant plane. The outputs of these detec-
tors then act exactly as the outputs of a single quad cell in
the focal plane of the selected subaperture would in a conven-
tional Hartmann system. Therefore, any processing techniques
which work in the Hartmann system are applicable in this
configuration also.

SUBAPERTURE

INPUT PUPIL
PLANE

f_1

f_1

SUBAPERTURE
DETECTOR

SUBAPERTURE
DETECTOR

CONJUGATE
PUPIL PLANE

f_2

f_2

QUADRANT
DIVISION
PRISM
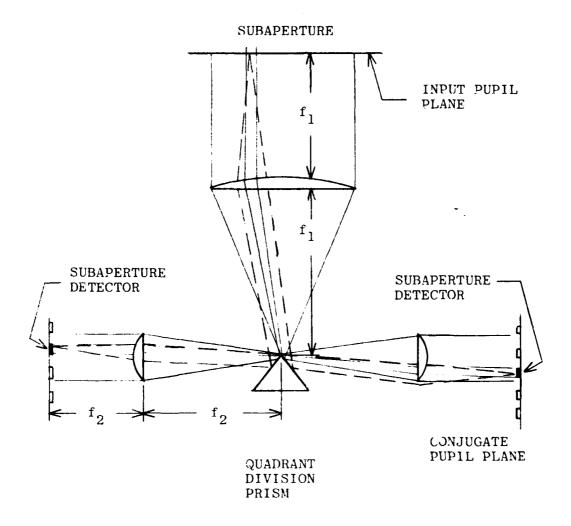
Figure 4.   Detector arrays used as pupil dividers.   In each
quadrant channel a single detector element is pro-
jected onto the input pupil plane and defines a
subaperture. The 4 detector elements, one from
each channel, which map onto the same input sub-
aperture, form a quadrant detector which may then
be used to determine the wavefront tilt in that
subaperture.

23

Thus, the I^3 sensor processing algorithms with nutation modulation are immediately applicable to the LSI^3 processor. The processing algorithms proposed for the LSI^3 sensor are optimized versions of the infrared I^3 sensor algorithms for use in quantum limited systems.
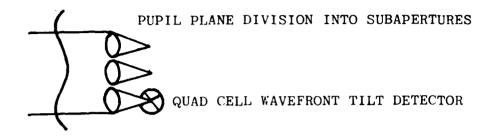
2.0 THE LSI^3 SENSOR CONCEPT

The LSI^3 wavefront sensor promises significantly improved performance and lower cost than first generation wavefront sensors. This has been made possible by several basic advances in wavefront sensor technology that will be described in this chapter.

The advances in performance are due to the optical configuration of the wavefront sensor which combines the advantages of the Hartmann, I^3 and shearing interferometer wavefront sensors, and the signal processing algorithm using modern estimation theory. Quantitatively the LSI^3 sensor is approximately a factor of two more sensitive than first generation photon noise limited wavefront sensors, like the shearing interferometer and I^3 sensor, when operated under identical conditions. This factor of two is explained in greater detail later.

2.1 LSI^3 Optical configuration

The LSI^3 wavefront sensor has some of the properties of a Hartmann sensor and the I^3 sensor modification of it, and some of the properties of a shearing interferometer. Figures 5a, 5b, and 5c are optical schematics of these wavefront sensors. The LSI^3 is like a Hartmann and I^3 sensor in that a quadrant divider is used to measure the centroid of the target to determine subaperture wavefront tilt. It is similar to the shearing interferometer in that the subapertures are defined at a conjugate pupil plane. Where the I^3 sensor required a reference beam to avoid the catastrophic problem of aligning n quad cells with their respective subaperture optical axes as in the traditional Hartmann sensor, the LSI^3 sensor uses a single 4-sided pyramid divider instead of n quad cells, and avoids that alignment problem entirely. By using a quadrant scheme for centroid location as in the I^3 sensor, the same photons are

25

PUPIL PLANE DIVISION INTO SUBAPERTURES

QUAD CELL WAVEFRONT TILT DETECTOR

(a) Hartmann sensor.

ROTATING
GRATING

PUPIL
PLANE
WAVEFRONT
DIVISION
INTO
SUBAPER-
TURES

(b) Shearing interferometer.

ABERRATED WAVEFRONTS

NUTATOR

FOUR-SIDED PYRAMID
WAVEFRONT TILT
DETECTOR

ONE OF FOUR
DETECTOR ARRAYS
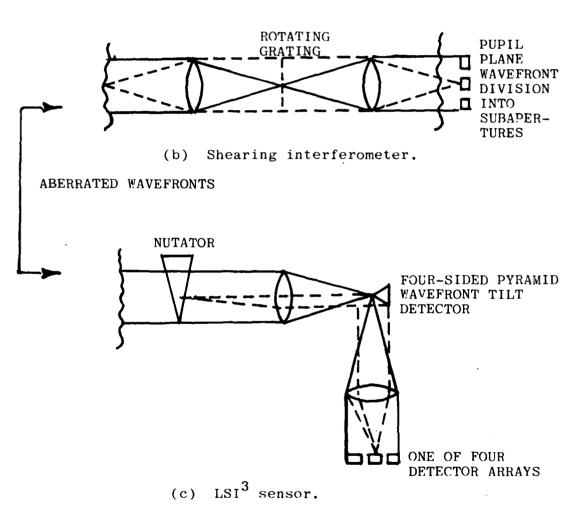
(c) LSI^3 sensor.

Figure 5. Hartmann, SI and LSI^3 sensors.

used for x tilt and y tilt measurements resulting in greater
sensitivity than the shearing interferometer; this is explained
in detail later in this chapter. In short, the LSI^3 sensor of-
fers the advantages of both the Hartmann and shearing interfero-
meter sensors without the disadvantages that are peculiar to
either.

Light from the target goes through a nutator, P1, and is
focused onto the pyramid. From the pyramid, the light is recol-
limated by a lens. The detector array, which defines the sub-
apertures, is placed behind the collimator. In the case of Fig-
ures 5b and 5c, the pupil division is performed at a plane
that is a conjugate of the P1 plane in front of the first lens.

The nutator is shown schematically in Figure 5c as a ro-
tating wedge of glass (in practice galvanometer nutators are
used, as in the I^3 sensor). The effect of the nutator is to move
the image of the target in a circular pattern at plane P2, where
the four-sided pyramid is located. This nutation modulates the
intensity of the light arriving at the detectors. The output
of the detectors is then demodulated to give the subaperture
wavefront tilt. The nutation in a practical wavefront sensor
is performed by two resonant galvanometer driven mirrors (see
Section 6) located near a conjugate image of the primary. The
nutation radius, the LSI^3 sensor's version of shear, is elec-
tronically controlled by varying the drive voltage to the gal-
vanometers.

A simplified description of the operation of the wavefront
sensor may be understood by masking the P1 plane in Figure 5c
to a single subaperture and ignoring the nutator. Figure 6
shows how wavefront tilt is measured. Light from a single sub-
aperture is focused on the tip of the pyramid; light from the
central subaperture will only fall on the central detector in
each of the four detector arrays. Also note that if the sub-

27

(a)

WAVEFRONT TILT

(b) Light from
    single subaperture

DETECTOR ARRAY 2

(c)

DETECTOR ARRAY
III

DETECTOR ARRAY I

DETECTOR ARRAY IV
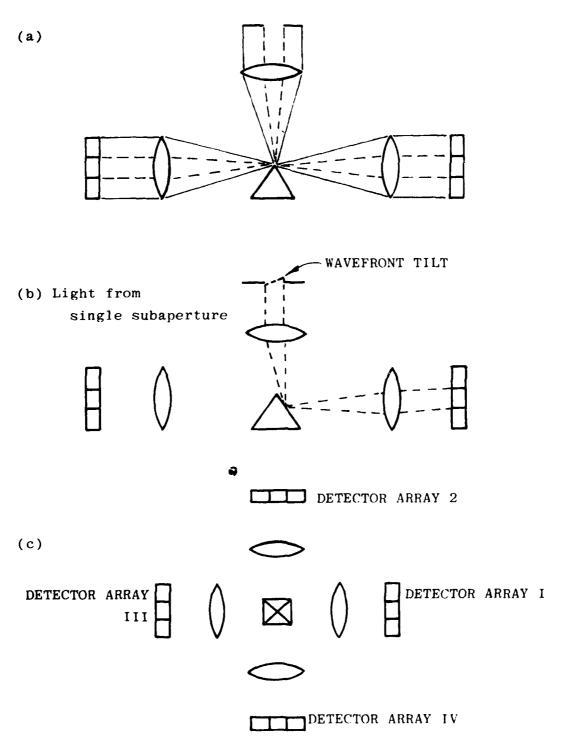
Figure 6.   Measurement of wavefront tilt.

28

aperture wavefront is tilted, its image will be shifted at the plane of the pyramid. As a result, more light will be detected by the detector on the right side than the left, as shown in Figure 6.

The difference between the LSI^3 and the I^3 sensor is clear. In the I^3 sensor, as in the Hartmann sensor of Figure 5a, the wavefront is first divided into n subapertures by an optical divider and each subaperture tilt measured by four detector elements in a quad cell configuration. In the LSI^3 sensor, the quad cell measurement is provided by a single 4-sided optical divider and then the wavefront is divided into subapertures for detection by 4 detector elements for each subaperture. In the LSI^3 configuration, the detector elements are not clumped together as quad cells; therefore a uniformly spaced detector array may be utilized. However, the signal processing algorithms are similar in the I^3 and LSI^3 since quad cell centroiding and nutation modulation are used for the basic subaperture tilt measurements. This is the principle behind the LSI^3 sensor.

2.2 Signal Processing

Without nutation, the signal processing algorithm is simply the Hartmann quad cell algorithm.

$$Tilt_i = \frac{D_{I,i} + D_{III,i} - D_{II,i} - D_{IV,i}}{D_{I,i} + D_{II,i} + D_{III,i} + D_{IV,i}} , \tag{1}$$

where tilt i is the tilt in the i'th subaperture, $D_{x,y}$ is the output of the yth detector in the xth array; a similar formula is used for tilt in the orthogonal direction.

With nutation, the detector outputs are a function of nutation radius and phase. The outputs of four detectors over a complete nutation cycle are needed to derive subaperture tilt. The basic concept is the same as equation 1. The numerator of equation 1 is a term that is linearly related to the wavefront tilt for small tilts and linearly related to target brightness. The denominator is independent of tilt and linearly related to target brightness.

The ratio is then linearly related to tilt and independent of target brightness.

The formula for demodulation with nutation is

$$\text{tilt} = \frac{\int_0^2 \sum_{j=1}^4 D_J(\theta) N_J(\theta) d\theta}{\int_0^2 \sum_{j=1}^4 D_J(\theta) P_J(\theta) d\theta} \tag{2}$$

where $D_J(\theta)$ is the Jth detector output as a function of nutation phase, $P_J(\theta)$ is a correlation function that extracts total power, $N_J(\theta)$ is a correlation function that extracts tilt and power.

A number of different P_J's and N_J's were investigated. These properties are discussed in Section 6. It was decided that, because a number of demodulation algorithms worked, it might be profitable to use modern estimation theory to find an optimal algorithm, given target size and shape and a statistical description of the noise. Photon noise limited and detector noise limited conditions were investigated.

The major result is that with the optimized algorithms the LSI[3] sensor, for most target scenarios, is predicted to have a factor of two higher phase accuracy for a given target signal power and equivalent detectors than the theoretical performance of the shearing interferometer CIS. The details of these calculations are given in Section 3.

2.3 Detector Selection

The AWS optical configuration, in which the quadrant or reticle elements precede the detectors, provides two unique virtues for the design of the detectors: the optical system is independent of the detector configuration except for the final collecting optics; the optical system is independent of the number of subapertures into which the pupil is divided. As a result, both the detector and optical design can be optimized separately. This is not true with a quad Hartmann type design of the I^3 sensor, in which the detector arrangements and subapertures dictate the optical arrangement. The interface between the sensor optics and detectors is an imaging system which divides the pupil images into subapertures. The final AWS optical design presented in Section 4 creates 16 mm diameter images of the pupil.

This pupil is imaged directly on arrays which then divide the pupil. The arrays that can be used are

(1)   area CCD's or self scanned diode area arrays preceded by intensifiers for direct detection and subaperture division, or

(2)   lens arrays which condense the light in the subaperture to an array of small points which can be used as input to optical fibers, or which can be made to match detectors directly or through an intensifying device.

The fibers can be spread out to large detectors or rearranged to convert from area to a linear format to permit the use of small linear CCD or self scanned diode arrays.

The results of the study produced three recommended detector systems for a 256 element array, and a photomultiplier array for a reduced scale 21 subaperture breadboard. These systems and their specifications in order of preference are as follows.

(1) EB mode detector, internal optics

    (a) Characteristics (see Figure 47)

        - Intensification with a 256 element linear self scanned diode array
        - Optical input; lenticular array, fiber optic area linear converter
        - Internal ellipsoid focusing fiber optic output on opaque GaAs cathode
        - Electron optics; 4:1 reduction and 15 - 20 kV
        - Reticon 256 element array; 10 MHz sample rate, 10 KHz frame rate for processed tilts

    (b) Performance

        - Highest possible efficiency in using solar spectrum (16.8% of all solar photons)

(2) EB mode detector, external optics

    (a) Characteristics (see Figures 49a,b,c)

        - Same as (1), but uses external optics for input to opaque cathode

    (b) Performance

        - Less than (1) because optics are less efficient

(3) EB mode detector, clamshell optics

    (a) Characteristics (see Figure 50)

        - Direct image input

- Straightforward intensifier design,
  2 to 3 coupled stages with P-24
  phosphors
- Transparent GaAs photocathodes
- Fiber optically coupled CCD
  buried channel array
- Limited array size by selective
  gating; samples taken in 32 x 36
  element blocks
- All elements commercially available,
  no special design required

(b) Performance
- 15% of solar flux utilized, more
  efficient input compensates for lower
  cathode sensitivity
- Poorer accuracy because of large
  noise factor (1.2)

(4) Breadboard (21 channel)

(a) Characteristics
- PMR's 1/2" diameter
- Lenticular array input to fiber
  optics which spread out to tubes
- Photon counting for low noise fac-
  tor

(b) Performance
- Bialkali photocathode comparable
  with CIS, potentially 5% of solar
  photons collected

The reasons given for these choices and a large variety of alternate schemes are given in Section 6 and the above performance data is summarized in Table 11.

The major advantages of the designs presented here are as follows.

(1) Intensified detectors provide photon limited signals for the highest theoretical accuracy.

(2) The ability of the LSI^3 sensor to use the wide solar spectra without loss of accuracy due to a loss of visibility permits the use of the new wide band GaAs cathodes. The variance for the best LSI^3 over that of the best shearing interferometer is a factor of 2.76 smaller.

(3) The combined improvement over theoretical CIS due to the algorithm and the efficiency of detection is equivalent to 1.63 magnitudes increased sensitivity.

2.4 Signal Processing Electronics

The LSI^3 optical system requires four separate detector arrays for each subaperture output as a quadrant output signal. In each detector array there will be at least one detector element per subaperture. For the large scale subaperture division, up to 256, the detector systems selected all use integrated circuit detector arrays.

These detector arrays accumulate photoelectrons and this charge accumulation replaces analog circuit integrators for signal processing. Furthermore, the integrated arrays take the subaperture optical data and transform it into 10 MHz serial electronic data. This charge accumulation and parallel-serial conversion reduces the analog circuitry requirements from four preamplifier-integrators per subaperture (1024 per system) to 1 preamplifier per array (4 per system) for up to

a 256 subaperture system. These 4 preamplifiers are each
followed by a 10 MHz pipelined digital processor and the
4 parallel outputs are then processed by a single processor
programmed with the optimum algorithm. The output from the
processor is a serial stream of tip/tilt error signals from
each subaperture.

The LSI^3 sensor electronic processor design is
intended to minimize operator intervention. Novel features
of the LSI^3 are exploited to permit automatic system calibra-
tion, extensive self test, and automatic dynamic alignment
during system operation. These extraordinary capabilities
are in addition to a signal processor architecture which
totally eliminates subaperture level electronic components
and adjustment. This proprietary architecture results in a
considerable reduction in circuitry compared to the tradition-
al processor per subaperture approach. The details of the
design are described in Section 5.

3.0 SIGNAL PROCESSING AND PERFORMANCE EVALUATION

3.1 Introduction

This section describes the various algorithms for deriving subaperture tilts from the output of the detectors. Several algorithms were developed in the course of this program. These algorithms, in addition to the original I^3 sensor algorithm (the SCS algorithm) were examined as part of this program. In order to facilitate the comparison of these algorithms with each other and with the AC shearing interferometer, a uniform mathematical notation is adopted.

The optical layout of the I^3 sensor has been described in previous sections. Basically, a divider is placed in a plane where an image of the target would be formed. After the divider, the light is recollimated and a detector array is placed in a plane that is conjugate to the pupil of the optical system. For each subaperture there are 2 to 4 detectors, one for each facet of the divider. The outputs of the detectors for each subaperture are demodulated to find the centroid of the image in the divider plane. The difference between the various I^3 algorithms and the shearing interferometer is that each algorithm is a different mathematical description of the centroid.

Because of the similarity of the various wavefront sensors, a single model for all of them is easily constructed. Figure 7 is an optical schematic of a generalized wavefront sensor. For a shearing interferometer, the mask is a Ronchi grating. For an LSI^3 sensor, each detector array has a different mask. The mask transmits the light in one quadrant of the plane. The target is imaged onto the reticle. The different type sensors have different reticles and different demodulation algorithms.

The image on the reticle is a convolution of the true

MASK

DETECTOR

TO DETECTOR
ARRAY NO.

2	1
3	4

SHEARING
INTERFEROMETER

MSI^3 SENSOR
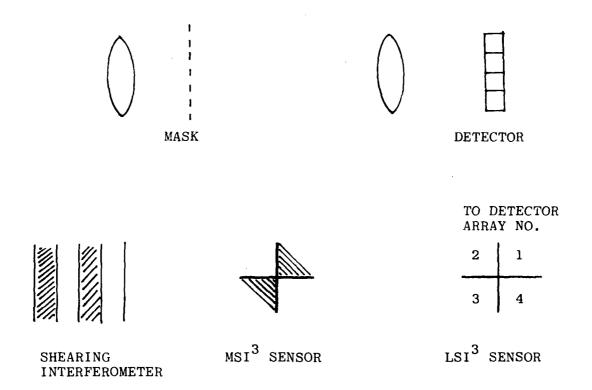
LSI^3 SENSOR

Figure 7. Optical schematic.

object, the diffraction limited point spread function of the telescope, and the atmospheric point spread function. We will now describe the AC shearing interferometer, the LSI^3 sensor, and the MSI^3 sensor.

3.2 LSI^3, MSI^3 and Shearing Interferometer

For all these types of wavefront sensors, the output of the detector is eq. 3.

$$\text{Detector output} = \int_{-\infty}^{\infty} dx \int_{-\infty}^{\infty} dy \quad M(x-f, y-g) T(x,y) \qquad (3)$$

where $T(x,y)$ is the effective irradiance distribution of the target (convolution of true object and atmospheric point spread function (PSF) and diffraction PSF); $M(x,y)$ is the mask function; f, g are the modulation functions.

Table 1   lists the types of masks and modulation functions for the three types of wavefront sensors.

Equation 3 is different from the traditional formula for a shearing interferometer derived using Fourier optics. In effect, it says that the difference between the various sensors are the masks and modulation patterns, and that these are the only differences, since the subapertures are divided in the same way. Hence, difference in the signal-to noise ratios (SNR) of the various sensors may be accurately derived from equation 3.

In an LSI^3 system, there are four detectors per sub-aperture. Because of nutation, the outputs of these detectors change with time. This is also true for the shearing interferometer. In addition to different mask functions and modulation functions, the demodulation algorithms for the shearing interferometer and I^3 sensors are different. For a shearing interferometer, the centroid is at zero phase for a single spatial

TABLE 1. MASKS AND MODULATION FUNCTIONS.

Sensor	Mask	f, g
SI	(for x) $M = 1$ for $x > 2nD$, $x < (2n + 1)D$ $= 0$ elsewhere and n is an integer, D is ½ grating period	$f = \frac{D}{\pi}\theta$, $g = 0$ $\theta = 2nfT$
MSI^3	$M = 1$ $\quad x > 0$ and $y > 0$ $= 1$ $\quad x < 0$ and $y < 0$ $= 0$ $\quad$ elsewhere	$f = r \sin \theta$ $g = r \cos \theta$ r is nutation radius
LSI^3	for quad 1 $\quad M = 1$ $\quad x > 0$ $\quad y > 0$ $= 0$ $\quad$ elsewhere	same as MSI^3

39

frequency component of the target. Phase is defined by equation 4.

$$\phi_x = \tan^{-1} \frac{\sum\limits_{i=1}^{4} \int\limits_{0}^{2\pi} S_i O_i \, d\theta}{\sum\limits_{i=1}^{4} \int\limits_{0}^{2\pi} C_i O_i \, d\theta} \qquad (4)$$

where O_i represent the outputs of the 4 detectors, S_i is a correlator function which extracts the sine of the phase from the detector output, and C_i the cosine extraction.

For a conventional radial grating interferometer, separate detectors are used for x tilt and y tilt and hence for ϕ_x two of the correlation functions are 0 for x tilt and the other two are 0 for y tilt.

In an I^3 sensor, the tilt is defined by equation 5.

$$\text{tilt} = \frac{\sum\limits_{i=1}^{4} \frac{1}{2\pi} \int\limits_{0}^{2\pi} N_i O_i \, d\theta}{\sum\limits_{i=1}^{4} \frac{1}{2\pi} \int\limits_{0}^{2\pi} D_i O_i \, d\theta} \qquad (5)$$

where O_i is the output of the detectors, N_i; and D_i are correlation functions. As explained in Section 2, the numerator is a term that is proportional to the tilt and target brightness, while the denominator is a term that is proportional to target brightness.

Table 2 shows the various demodulation functions for the three wavefront sensors.

TABLE 2. DEMODULATION FUNCTIONS.

Sensor	Numerator function for x tilt	Denominator function
Shearing Inter. (Ronchi grating)	$\sin\theta$	$\cos\theta$
MSI[3]	$\sin\theta$	$\sin 2\theta$ both x & y
LSI[3]	There are 4 different demodulation algorithms for the LSI[3] optical configuration. See text for details	
DC (x tilt)	$N_1 = N_4 = 1$ $N_2 = N_3 = -1$	$N_i = +1$
SCS (original I[3])	$N_1 = \sin\theta$ $N_2 = -\sin\theta$ $N_3 = N_1$ $N_4 = N_2$	$D_1 = \sin\theta$ $D_2 = N_i$ $D_3 = -\sin\theta$ $D_4 = -N_3$
MS (This algorithm is equivalent to the MSI[3] sensor)	$N_1 = \sin\theta$ $N_2 = -N_1$ $N_3 = N_1$ $N_4 = -N_1$	$D_1 = D_3 = \sin 2\theta$ $D_2 = D_4 = -\sin 2\theta$
ACDC	$N_1 = 1 - \cos\theta$ $N_2 = -1 + \cos\theta$ $N_3 = N_2$ $N_4 = N_1$	$D_1 = 1$ $D_2 = 1$ $D_3 = 1$ $D_4 = 1$

These correlation functions are optimal in the sense that for a Gaussian object and nutation radius equal to the width of the object.

The noise in the derived tilt is a minimum for a given level of photon noise.

41

3.3 Performance Evaluation

Once we have a description of the various wavefront sensors (equations 3, 4, and 5), it is possible to evaluate the relative SNR's of the sensors.

In order to calculate the noise equivalent tilt of a sensor, we must determine the responsivity of the sensor, the change in the derived tilt (equation 4 or 5) for a given change in the centroid of the target, as well as the expected fluctuations in the derived tilt due to measurement noise. When the target is centered, the numerator terms of equations 4 and 5 are zero. For small changes in the target position the numerator term will change significantly, while in first order, the denominator term will not change. As a result, all of the following calculations will concentrate on the numerator term. For practical purposes, the SNR of the numerator is the SNR of the ratio. This is shown below.

$$\partial R/\partial X = (1/D)(\partial N/\partial X) - (N/D^2)(\partial D/\partial X) \qquad (6)$$
$$\text{or } (1/D)(\partial N/\partial X)$$

where R_a is the ratio of two numbers, N or O (small), $\frac{\partial D}{\partial X}$ or O (small), and x is the displacement of the target centroid.

Equation 6 shows that the responsivity of the ratio R is dependent primarily on the first term in equation 6, the second term being very small. Similarly, the fluctuations in R_a in equation 7 due to measurement noise are dependent primarily on the numerator.

$$\partial R_a/\partial n = (1/D) (\partial N/\partial n) - (N/D^2)(\partial D/\partial n) \qquad (7)$$

where n is a random variable of which N and D are functions.

Since N is small, only the first term in equation 7

is important. The variance of R_a due to fluctuations in n are then equation 8.

$$\sigma_R = \frac{1}{D} \cdot \left[\sum_n (\partial N / \partial n)^2 \left\langle (\Delta n)^2 \right\rangle \right]^{1/2} \qquad (8)$$

where Δn are the fluctuations due to noise and the summation is over the random variables. Consequently, the SNR of Ra ratio is equal to the SNR of the numerator.

The numerators of equations 4 and 5 have the form of equation 9.

$$\text{Num} = \sum_{n=1}^{4} (1/2\pi) \int_0^{2\pi} d\theta \quad C_i(\theta) O_i(\theta) \qquad (9)$$

where C_i is the correlation function for the ith detector, O_i is the output of the ith detector.

In the photon noise limited case, equation 10 is true; in a detector noise limited case, 11 is true.

$$\sigma_O^2(\theta) = O(\theta) \qquad (10)$$

where the variance of $O(\theta)$ is $O(\theta)$ for photon noise.

$$\sigma_O^2(\theta) = \text{constant} \qquad (11)$$

for detector noise limited operation.

Using standard error propagation formulae, the SNR is Equation 12 for photon noise.

$$(SNR)^2 = \frac{\left[\sum \frac{1}{2\pi} \int_0^2 C_i(\theta)R_i(\theta)d\theta \right]^2}{\sum \frac{1}{2\pi} \int_0^2 C_i{}^2(\theta)O_i(\theta)d\theta} \qquad (12)$$

where $O_i(\theta)$ is defined by equation 3, and $R_i(\theta)$ is defined by equation 13.

$$R(\theta) = \int_{-\infty}^{\infty} dx \int_{-\infty}^{\infty} dy \; M\left[x-f(\theta), \; y-g(\theta)\right] \; \nabla T(x,y) \cdot \hat{x} \qquad (13)$$

The difference between 3 and 12 is that $T(x,y)$ the effective target irradiance distribution in equation 3 is replaced by the slope of the irradiance distribution. The numerator of equation 12 is the square of the responsivity, while the denominator is the variance due to photon noise. In the following graphs and tables, the data was generated from equations 3 & 13. The integrals were evaluated numerically.

The assumptions for the calculations are listed in the figures. A Hartmann sensor is also evaluated. The main difference between the Hartmann sensor and the LSI[3] sensor is that the effective target irradiance distribution in the Hartmann system is the convolution of the subaperture diffraction pattern and the true target while for the LSI[3] and shearing interferometer, the effective shape is the convolution of the full aperture dif-

fraction pattern and the true target.

The atmosphere was ignored in these calculations for two reasons. One was to simplify the calculations. The second was to make the comparison with other published data* which compared the shearing interferometer to the Hartmann sensor.

The effect of the atmosphere is to limit the usable shear on the shearing interferometer to approximately r_o, the atmospheric phase coherence length. The result of including the atmosphere in calculating the data for the figures would be to reduce the advantage of the LSI^3 and SI over the Hartmann sensor for very small targets or very distant targets. We repeat that the results in this report do not conflict with other published data*.

3.4 Optimal Correlator and Object Size Determination

While evaluating the relative SNR of several I^3 demodulation algorithms, it was decided that it would be profitable to analytically determine an optimal correlation function for equations 4 and 5. Here we use the word optimal correlator to mean a function $C_i(\theta)$ that will result in a minimum variance tilt estimate given a known noise in the detector output $O(\theta)$.

For photon noise limited operation, the optimal correlation is found by setting the variational derivative of equation 12 to zero and solving for the correlation function $C_i(\theta)$. The answer is equation 14.

$$\text{Optimal } C_i(\theta) = \frac{R_i(\theta)}{O_i(\theta)} \qquad (14)$$

---

* Reference will be made available to qualified military and government agencies on request from RADC (OCSE) Griffiss AFB NY 13441.

45

where R is defined by equation 13 and O is defined by equation 3.

In all the figures in this section*, the graphs labeled optimal I^3 use the correlation function defined by equation 11. Note that the optimal correlator changes with object size, shape as well as nutation radius.

Another topic that was studied as part of the AWS program was the measurement of object size by proper demodulation of the outputs of the wavefront sensor detectors. The effective object size of a combination of atmospheric seeing blur and true object size is an important parameter in a shearing interferometer wavefront sensor because the highest tilt accuracy is achieved when the shear is matched to the object size, when the grating period was twice the object size. While Figure 9 shows that for a Gaussian object, the accuracy of a tilt measurement is not a strong function of nutation radius when an optimal correlator is used, the measurement of object size is still important. The reason is that some of the I cubed demodulation algorithms are object size dependent, in the sense that the derived tilt in radians is a function of the angular size of the object. Table 3 lists the size dependence of various algorithms.

*Figures 7 through 12

16
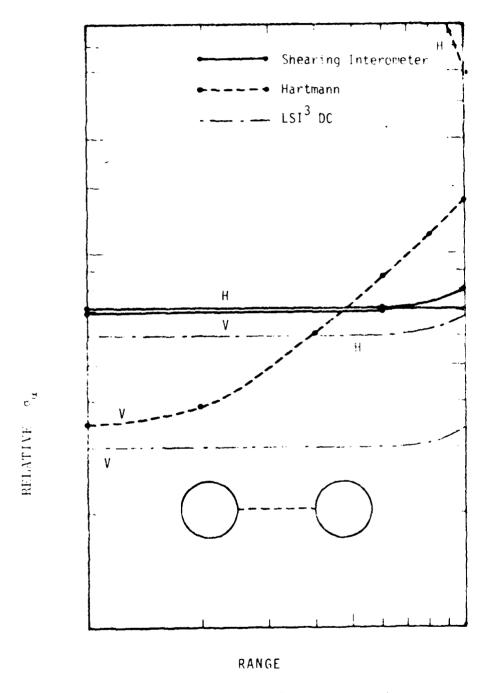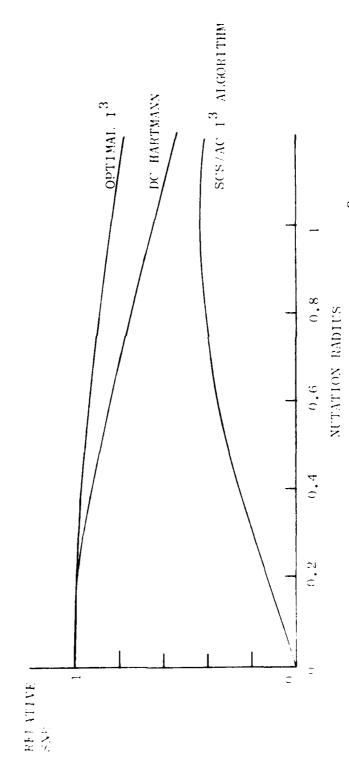
Figure 8. Relative phase variance vs. relative range for several wavefront sensors.

CIRCULAR GAUSSIAN SHAPED OBJECT

PHOTON NOISE LIMITED OPERATION

OPTIMAL I^3

DC HARTMANN

SCS/AC I^3 ALGORITHM

RELATIVE
SNR

1

0

0.2   0.4   0.6   0.8   1

NUTATION RADIUS

Figure 9.   Relative SNR vs. nutation radius for various I^3 algorithms.

18
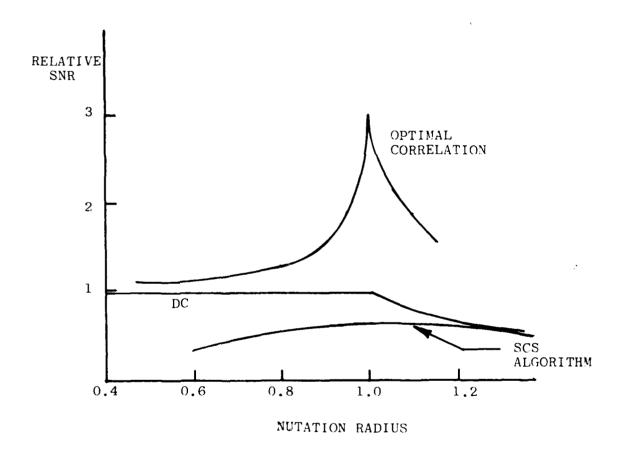
Figure 10. Relative SNR vs. nutation radius for a
square object.

49

CIRCULAR OBJECT, 4 μRAD DIA.
ATMOSPHERE PSF IGNORED
DIFFRACTION PSF << 4 μRAD

o SI SET FOR OPTIMAL
                  SHEAR

X LSI^3 DC ALGORITHM
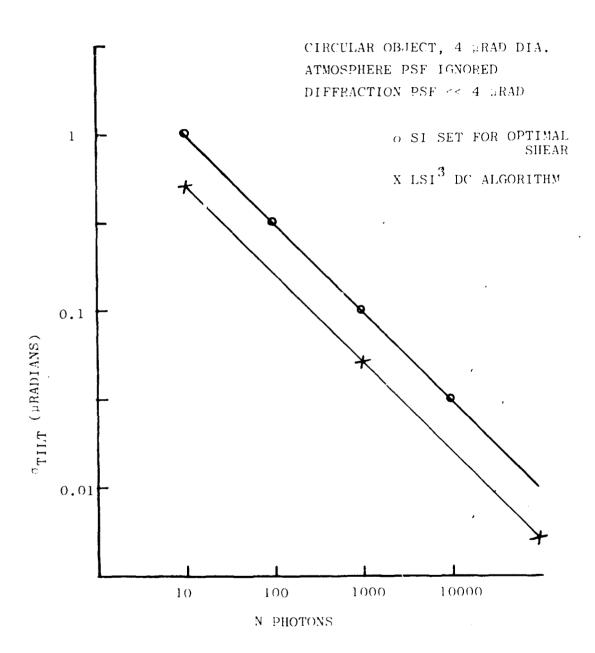
Figure 11.   Tilt noise as a function of number of
             detected photons.
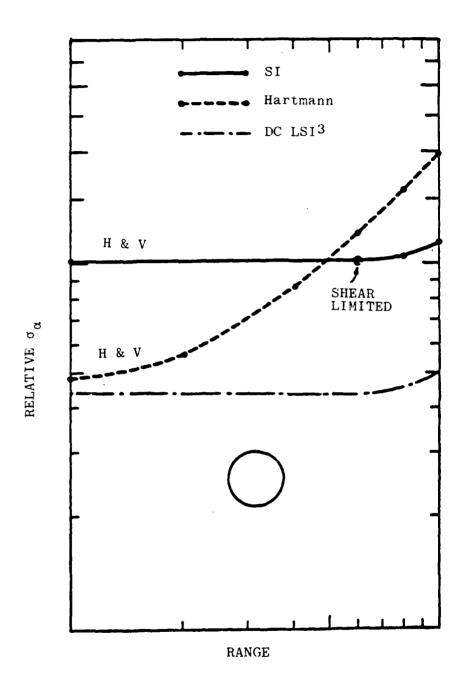
Figure 12. Relative variance vs. relative range for
several wavefront sensors.

TABLE 3. SIZE DEPENDENCE OF VARIOUS ALGORITHMS.

TERM	OBJECT SIZE DEPENDENCE $W/2 \geq r$	$W/2 >> r$	TYPE OF MEASUREMENT
SCS/MS Numerator	$1/W^2$	1	AC
SCS Denominator	$1/W$	1	AC (10 kHz)
MS Denominator	$1/W^2$	1	AC (20 kHz)
DC Numerator	$1/W$	1	DC
DC Denominator	1	1	DC
Optimal Numerator	$1/W$	1	DC & AC

52

As an illustration, we note that in the classical quad cell Hartmann system (DC numerator and denominator) the ratio is proportional to 1/W. In other words, if the wavefront tilt is 1 μrad and the width of the object is 10 μrad, the output of the DC algorithm would be ∿ 2/10; if the object size was 100 μrad, a 1 ; rad tilt would give an output of 2/100. On the other hand, use of the DC numerator and SCS denominator would produce a number that was independent of object size, depending only on nutation radius. This is the case with the shearing interferometer where the output represents a given wavefront tilt that depends on the shear but not on object size. In general, the size of the object will not change on a fast line scale, e.g. 10kHz. As a result, the object size may be measured with very high accuracy using several tens of milliseconds of data. The preferred method of measuring size is to use the SCS denominator and the MS denominator.

Object size may in theory be measured with a shearing interferometer by monitoring fringe visibility. This technique, however, has a drawback. The fringe visibility formula that is usually presented in descriptions of the shearing interferometer ignores the effect of scintillation. Because of this fringe visibility, measurements are unreliable. Currie et al.* have solved the problem by measuring the apparent visibility as well as the scintillation and correcting the visibility results in the data analysis. The problem is due to the fact that fringe visibility is in effect the ratio of the AC optical power to the DC optical power. Modulating at 10kHz there are no scintillation effects at 10kHz but there are at DC.

With an I^3 sensor, which compares the AC power at 10kHz (SCS denominator) to AC power at 20 kHz (MS denominator), scintillation is not a significant source of error.

---

*Currie et al., Astrophys. J. 187, 131(1974).

4.0 OPTICAL SYSTEM DESIGN

The design of the AWS optical system is less demanding than might be expected because the instrument uses a reference beam to define a perfect wavefront. By measuring the difference between the reference and target point positions, the errors of the common mode optics are removed from the measurement of the wavefront. In consequence, it would seem that any optical system would be adequate. However, the effect of an inferior optical system will be to reduce the performance in detecting and correcting the wavefront for small objects. For a 2 arc second object (α_0), the response will be reduced to 90% if the standard deviation of the spread function σ is 0.86 arc seconds.

If we assume Gaussian spread functions and compute the change in peak intensity to be $i(P) = (\sigma_0/\sigma_{SF})^2$, where $\sigma_0{}^2$ is the diffraction limited spread function which is given approximately by $(0.375_\delta \lambda/D)^2$, and where $\sigma_{SF}{}^2$ is the variance of the allowed spread function for 90% response to a target, we can use the expression for peak intensity or the Strehl Ratio, to yield a required rms phase error for the sensor optical system. Thus

$$i(P) = (\sigma_0/\sigma_{SF})^2 = \left\{ 1 - \left[(2\pi/\lambda)^2 (\Delta\lambda)^2 \right] \right\} = e^{-(2\pi\Delta\lambda/\lambda)^2}$$

(15)

or

$$J_0{}^4(2\pi\Delta\lambda/\lambda) \text{ for large arguments}$$

for $\bar{\lambda} = 0.64$ μm (because of the use of GaAs cathodes) at $D = 1.6$ m, $i(P) = 0.0304$, and the rms phase error $\Delta\lambda$ allowed is $\lambda/3.3$. The allowed peak to peak error is about one wave.

This is not a difficult requirement for an f/16 optical system, and it will permit some latitude in handling difficulties due to nutation, pupil imagery and chromatic aberrations. The optical systems that have been designed began as refracting sys-

54

tems. The evolution of the detector design has extended the range of colors to such an extent that a reflecting system became desirable.

The first problem is to design a system which prevents subaperture smearing.

The nutation device is the major geometrical constraint on the system. In order to operate at 10 kHz, the beryllium mirrors are limited to dimensions of approximately 5 x 7 mm. For a system to have no nutation-induced subaperture smearing, the telescope primary should be imaged onto the nutator mirrors and then onto the detector array, while the object should be imaged onto the divider plane. These operations are accomplished by the configuration in Figure 13. In this type of system, the maximum number of resolved subapertures is diffraction limited. If f/4 lenses are used with 5 mm mirrors, the maximum number of subapertures is approximately $(5 \text{ mm}/1.2 \ \lambda f)^2 \simeq 1.6 \times 10^7$.

This is not an important constraint, therefore, and we may consider simpler optics.

The configuration of Figure 14 shows the nutation mirrors displaced from conjugate pupil planes, eliminating a lens. The primary is considered to focus at L1 with a speed of f/20. The focal length of L3 is chosen to match the detector size to pupil size.

For a typical system, assume the following.

(1) A 10 cm subaperture size, which gives an angular nutation radius of approximately 1 arc sec at the pupil. The lateral shift at the conjugate pupil plane between nutators is

$$F_4/F_3 d \sin(1 \text{ arcsec}) \qquad (16)$$

DETECTOR
ARRAY

RETICLE/
PYRAMID

2ND
NUTATOR

1ST
NUTATOR
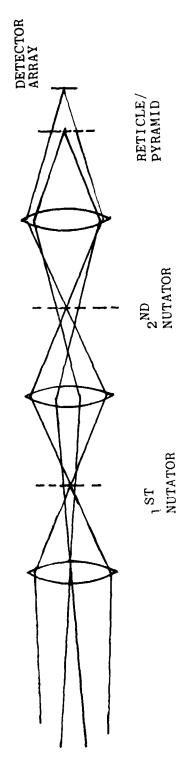
Figure 13. Double pupil image optics.

DETECTOR
ARRAY

DIVIDER
RETICLE /
PYRAMID

2ND
NUTATOR

1ST
NUTATOR

d

ℓ_1 — d_1 → | ← d_2 → ℓ_2 ← d_3 →
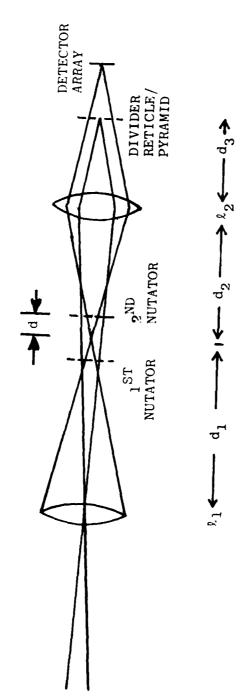
Figure 14. Single pupil image optics.

57

or, at the pupil plane, we want

$$\Delta x = d(\sin 1")(F_4/F_3)^2 \ll 10 \text{ cm} \qquad (17)$$

(2) If the telescope has a 1.5 meter primary @ f/20 for a 5 mm nutator mirror f_3 must be 10 cm. For d - 1 cm the nutation shift, or pupil smear, will be

$$\Delta x \sim (3000/2 \times 10^6) \text{ cm} \sim 4.5 \text{ m\tau} \qquad (18)$$

or about 5% of a subaperture diameter. For Ll of f/10, diffraction smearing is very small, approximately 5 micrometers.
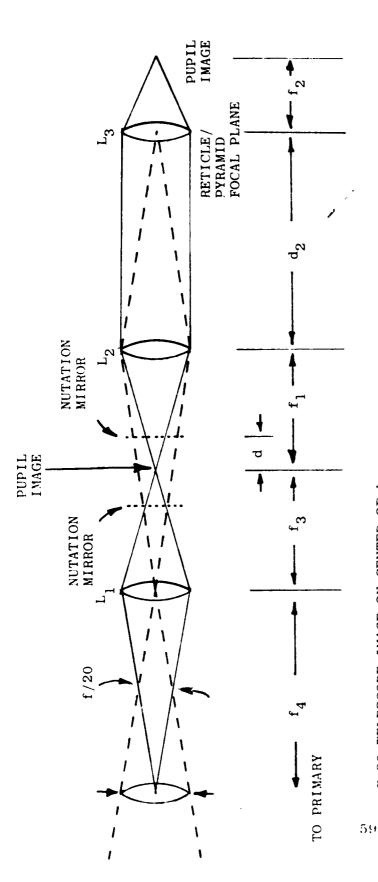
This configuration requires a nutation angular range of

$$15 \text{ waves} \div 5 \text{ mm}$$

or about 1.5 millirads, which is easily achieved with the current nutator.

It is clear that the simple optical design of Figure 14 will *perform amply well* in the approximately 200 subaperture prototype system, with negligible degradation due to subaperture smearing. In order to easily match the detector size to the pupil (a problem of magnification), a field element might be added at the divider plane, as in Figure 15.

The later design was much larger than it had to be because the reimaging lens L_2 could be placed between the galvanometers. Further, there are needless design problems created when the system pupil in a 1:1 imaging system is asymmetrically posi-

F/20 TELESCOPE IMAGE ON CENTER OF L_1

L_1: 10 cm f.l., 1 cm dia.

f_3 approx. 10 cm, F_1 approx. 10 cm

L_2: 10 cm f.l., 1 cm dia.

d_2 approx. 20 cm, d approx. 1 cm

L_3: selected to match detector array size

Figure 15. Single pupil image optics with field lens.

tioned. This pupil location is the telecentric position shown in Figure 15 and all principal rays are collimated on the pyramid side.

All aberrations are present in such an arrangement, and the design must correct all of them, particularly the worst offenders, lateral color and coma.

If the pupil is moved to a symmetric location, there are specific gains, since such systems at unit magnification are free of coma distortion and chromatic difference of magnification. Since the wide optical bandwidth is the most important requirement in a photon limited environment, and since it is difficult to remove all chromatic aberrations with the limited dispersions of glasses available, obtaining freedom from one chromatic aberration is of utmost value is securing an adequate design. In consequence, the symmetric design of Figure 16 was adapted. The galvanometers are placed on either side of a simple symmetric triplet. The actual separation of the galvanometers and the fraction of subaperture smearing that will exist is dictated by the size of the coils and the closeness of the mirrors to the pupil image plane. The positioning of a lens between them will actually decrease the optical distance because of the generally finite separation of principle planes, which. in the case of one design described by Conrady, for the present geometry would be 6.7 mm, reducing the distance of the galvanometer mirror from the pupil image from 10 mm to 6.7 mm and reducing the subaperture smearing from 10% to 6.7%.

The actual lens has not been designed at this time, but the basic form is adequate. It will probably be necessary to intro-
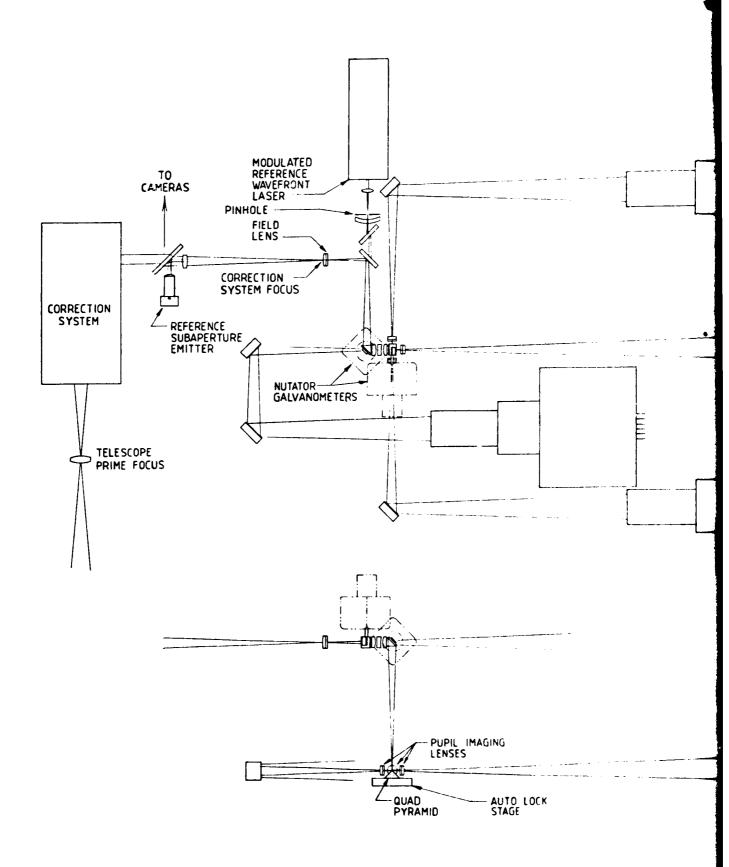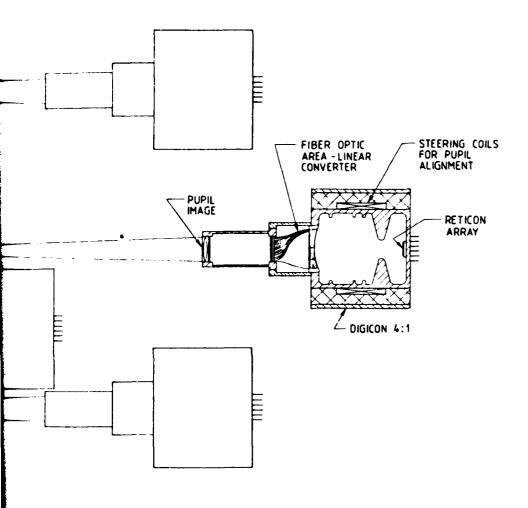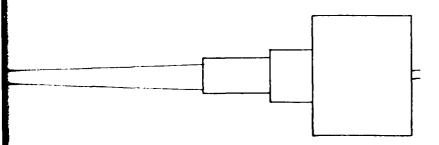
TO
CAMERAS

MODULATED
REFERENCE
WAVEFRONT
LASER

PINHOLE

FIELD
LENS

CORRECTION
SYSTEM FOCUS

CORRECTION
SYSTEM

REFERENCE
SUBAPERTURE
EMITTER

NUTATOR
GALVANOMETERS

TELESCOPE
PRIME FOCUS

PUPIL IMAGING
LENSES

QUAD
PYRAMID

AUTO LOCK
STAGE

Figure 17. AO design.

FIBER OPTIC
AREA - LINEAR
CONVERTER

STEERING COILS
FOR PUPIL
ALIGNMENT

PUPIL
IMAGE

RETICON
ARRAY

DIGICON 4:1

AWS design.

A W S

OPTICAL SCHEMATIC

D   800001   1

61

duce a third glass type and two more elements to make an apochromat to secure the degree of chromatic correction desired.

The optical layout that results is quite compact. Starting at the upper left at the telescope prime focus, the beam diverges and is then collimated for passage through a correction system that includes a tip/tilt corrector and a deformable mirror. The beam is then refocused into the wavefront sensor. Before it is brought to focus, however, the central subapertures, which are occluded by the telescope secondary, are tagged by introducing a beam through a centrally located prism from a modulated subaperture reference emitter. This signal will be used to align all four arrays by the use of coils on the intensifiers. This electronic adjustment will compensate for the small changes in the intensifier which can be significant if they are only a few microns in error. The alignment of the optical system, to ensure registration at the fiber optic input, will require mechanical stability to within 1.3 min of arc (0.0004/1). This is not difficult to obtain.

Following the reference subaperture input, a field lens close to the correction system focus will image the deformable mirror, which is at a pupil image, onto the principal plan of the relay triplet.

Alternately, and preferably except for cost, the use of an anamorphic field lens to place the vertical and horizontal images on the respective galvanometers would eliminate subaperture smearing completely. The respective focal distances are 93.3 mm and 106.7 mm for horizontal and vertical galvanometers. The required anamorphic power is 1.3 diopters, which is an easily obtained amount of cylinder.

After this field lens, an almost completely reflective beam splitter is shown when the reference beam is introduced. The

wavefront is reflected because of its wide bandwidth. The reference wavelength will be derived from a modulated laser. Being monochromatic, the dispersion of the beam splitter is of no consequence. A corrector plate is included to correct the astigmatism. The residual negative spherical will be corrected by an additional element.

Since the reference beam is generated at a pinhole close to the beam splitter, the uncompensatable noncommon path is small, and the stability of the system is assured.

The combined beams proceed to the galvanometer and the relay lens, and are then focused on the quad pyramid. This pyramid is a critical element because its edges must be sharp. With the f/16 system illustrated here, the radius at an edge must not be greater than 2 µm. There is no way to obtain such an edge by polishing, but diamond machining and the use of cleaved crystals seem to provide reasonable means of manufacture.

A large number of tetragonal system crystals (but not diamond) provide natural pyramid corners. Among these are the holosymmetric class, which yield some four faceted corners and include rutile, anatase, zircon and others. This last is commonly synthetically grown and used in jewelery. The pyramid class, yielding the desired crystal, includes wulfenite ($PbMoO_4$).

The size of the quad is defined by the largest object and the amount of nutation to optimize the SNR. For 100 µrad objects, the smallest pyramid required is 5.12 mm. Gems of this size should be easy to acquire, particularly zircon, which accounts for the biggest rocks in the cheap discount stores.

The directions of the paths reflected from the faces will depend on the crystal, so that the final design will require further investigation into the fabrication of pyramids. Continuing along the path, the next element shown is a pupil imaging field lens which forms an image on the input to the pupil divid-

ng optical system. If the preceding fields lens were anamor-
hic, then lenses should be anamorphic as well, with the same
.dd-on cylinder of 1.3 diopters. The images of the pupils in the
livider plane in this case will be 1.125 mm and 0.875 mm because
)f the power changes required to transfer the images add up.
There is no problem in making the lenslet arrays in the pupil
divider rectangular.

The last optical elements are the lenticular lens arrays.
In this group, the first element is a simple achromat, which is
used to collimate the principle rays. This ensures that center
to center distances between lenslets and fibers are all the same.
The double array system shown is used to ensure that the pupil is
imaged on the fiber end, instead of the image of the object on
the pyramid.

This ensures that the distribution of light on the fiber
does not move so that imperfections in the fiber end do not
effect the nutated output. On the other hand, the input angles
into the fiber will change. Since these are always less than the
NA of the fiber, and since mixing occurs, so that all angles up
to the NA are present at the fiber output, this would seem to be
the way to minimize sensitivity to optical variation. It may,
however, be overkill, particularly since the use of the reference
beam essentially calibrates out the effects of imperfections in
each lens, fiber and detector.

The remaining element, the detector system, has been de-
scribed in the preceding section. The simple intensifier de-
sign with the transparent photocathode with a wide but manageable
spectral sensitivity, 0.5 to 0.8 m, is appropriate.

4.1 Reflective Systems

The greatest sensitivity is enjoyed by the intensifier that uses the internal reflector and opaque photocathode. The spectral sensitivity, however, is so wide that obtaining adequate chromatic correction in the optical system may not be possible. Because of this, reflecting systems have been examined and one design chosen. This is shown in Figure 17.
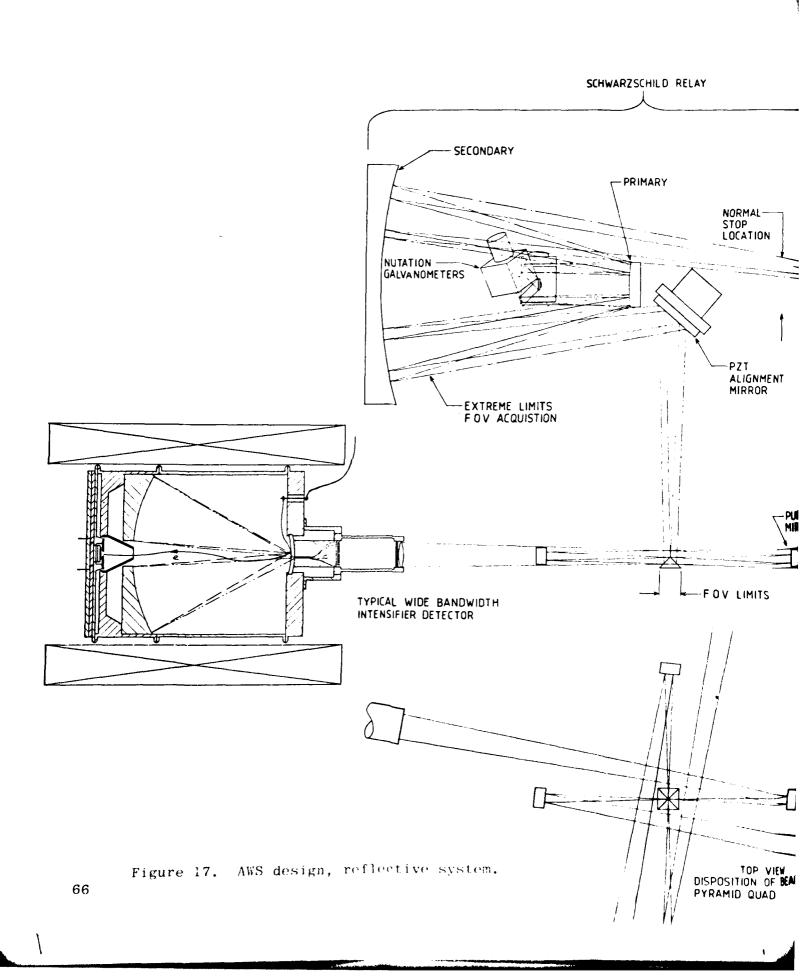
It uses the aplanatic properties of the Schwarzschild telescope to ensure freedom from spherical aberration, astigmatism and coma. Since it uses concentric spherical surfaces, fabrication will be simple and inexpensive. The prescription of the system is R_1 = 1.236F, R_2 = 3.236F, and d = 2F. The design has a focal length F of 80 mm.
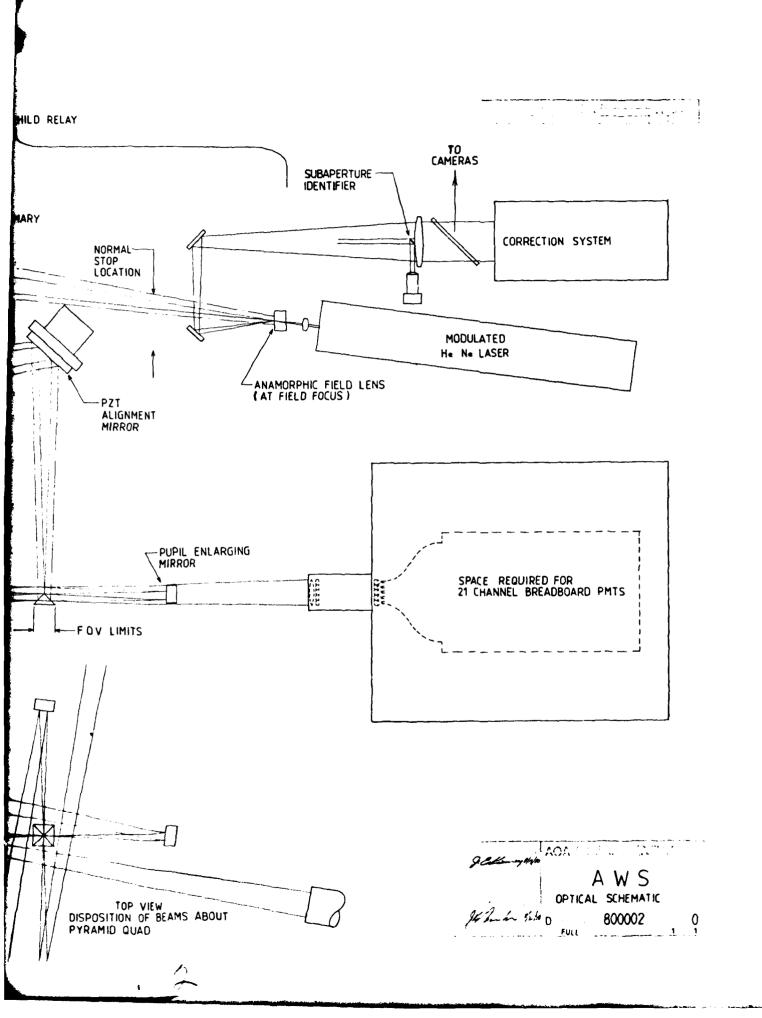
The telescope is used to collimate the beam, with a 5mm diameter. The nutator then reverses the beam direction and brings the return back along the opposite side through the telescope again.

There are a few innovations which further simplify the design. The input beam with the tagged central subaperture is reflected, aligned and focused on a negative field lens which will create an image of the pupil between the galvanometers. The reference beam will be introduced through a 10 μm diameter hole in this mirror. This pin hole in the reflective coating will filter the reference beam, absolutely define where it is, and enhance, to a small degree, the response of the system to small targets. The reason for this is discussed in Section 6.

There is one problem in the design that has not been resolved. The aplanatic solution is correct for a location of the stop at the center of curvature. The galvanometers could be placed at these locations.

The field lens mirror that would be required would be an anamorphic toroid which for an 80 mm focal length Schwarzschild

SCHWARZSCHILD RELAY

SECONDARY

PRIMARY

NORMAL
STOP
LOCATION

NUTATION
GALVANOMETERS

PZT
ALIGNMENT
MIRROR

EXTREME LIMITS
FOV ACQUISTION

TYPICAL WIDE BANDWIDTH
INTENSIFIER DETECTOR

PU
MII

FOV LIMITS

TOP VIEW
DISPOSITION OF BEA
PYRAMID QUAD

Figure 17. AWS design, reflective system.

66

HILD RELAY

ARY

NORMAL
STOP
LOCATION

SUBAPERTURE
IDENTIFIER

TO
CAMERAS

CORRECTION SYSTEM

PZT
ALIGNMENT
MIRROR

ANAMORPHIC FIELD LENS
(AT FIELD FOCUS)

MODULATED
He Ne LASER

PUPIL ENLARGING
MIRROR

SPACE REQUIRED FOR
21 CHANNEL BREADBOARD PMTS

FOV LIMITS

TOP VIEW
DISPOSITION OF BEAMS ABOUT
PYRAMID QUAD

AOA

A W S
OPTICAL SCHEMATIC

D   800002   0

FULL   1   1

design would have a focal length of + 72.73 mm, to image the pupil which is 800 mm upstream, on the first galvanometer and -123.5 mm to place the orthogonal image on the second galvonometer.

The result yields a 5 mm pupil image on the first galvo, but because of the telescope, creates a 39.8 mm pupil image on the second which is too great. Thus the use of galvos in the expected stop locations and proper imaging through them is not possible because of the size limitation on high speed resonant galvanometers. Fortunately, the field of view is small so that actual deviations from the rays shown in the figure about the stop locations are small and any astigmatism that might result from these small deviations about the proper alignment off axis should be small.

Residual aberrations can be balanced and, providing a means for rotating the wavefront and reversing the sign of the astigmatic terms would be desirable. For this reason, and to keep the galvanometers close together, a single mirror plus the two galvanometers are located in the collimated space.

The last fold mirror out of the relay telescope is mounted on a piezoelectrically adjustable mount. This is used to lock the reference beam on the pyramid. The focusing beam now proceeds to the pyramid where it is reflected from the four faces. The telescope itself forms an image of the pupil 115.8 mm from the apex. Consequently, a simple negative element, f = -41.6 mm, at 80 mm from the pyramid will magnify the pupil 7.17X onto the detector lenticular array 257 mm away. A hyperbolic figure is probably required but the size of the field on the mirror of 2.5 mm is so small that a spherical surface may be sufficient. At this point in the optical path, the optics serve only to get the signal to the right detector and performance is not

critical. The arrangement of elements in the layout is compli-
cated only because of the need for the reflected beams to miss
occluding structures.

The design requires a minimum number of elements, two good
spherical mirrors, 5 negative spherical mirrors, and a few fold
mirrors. It is completely free of dispersive elements. Even
the beam splitter and its loss has been replaced by a signal en-
hancing hole. The result is an optical system that is very ef-
ficient. If yttria protected silver mirrors are employed, the
mean reflectance from 0.44 to 0.84 μm will be 0.984. With twelve
reflections, the transmission will be 82.4% from input to the de-
tector.

5.0 SIGNAL PROCESSING ELECTRONICS

The Large Scale I^3 Sensor (LSI^3) electronic processor design is intended to minimize operator intervention. Novel features of the LSI^3 are exploited to permit automatic system calibration, extensive self test, and automatic dynamic alignment during system operation. These extraordinary capabilities are in addition to a signal processor architecture which totally eliminates subaperture level electronic components and adjustment. This proprietary architecture results in a considerable reduction in circuitry compared to the traditional processor per subaperture approach.

5.1 Processor Architecture

The architecture of the LSI^3 electronic signal processor is based on the fact that high speed digital memory is the simplest, most reliable, and least expensive electronic component to use for the design, fabrication, operation and maintenance of a large scale signal processor. Digital memory coupled with high speed digital arithmetic elements permits Time Domain Multiplexing (TDM) and this sharing of processing resources minimizes the circuitry required for signal processing. An additional positive feature is the inherent flexibility of programmable digital arithmetic elements.

There are three major subdivisions to the LSI^3 electronic processor. These are the Front End Processor (FEP), the Programmable Algorithm Processor (PAP), and the System Supervisor Processor (SSP). Figure 18 illustrates the data flow among the processors.

5.2 Front End Processor

The FEP digitizes, normalizes and buffers the detect-
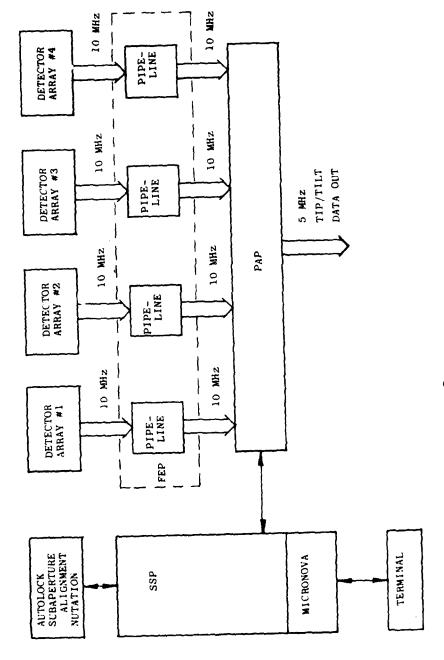
Figure 18. LSI³ signal processing.

70

ed signals. These functions are performed serially at the detector readout rate (10 MHz for 256 subapertures). **Figure 19** illustrates the pipeline approach to the FEP.

The processor architecture was designed so that any of the large scale (up to 256 subaperture) detectors selected for use in a system as described in the next section, can be accommodated. The only changes will be in the detector preamplifiers.

Each detector array requires a charge sensitive preamplifier. For the Reticon RL256C Solid State Line Scanner (SSLS) the maximum charge on any photodiode is approximately 4 picocoulombs. With 10 MHz readout, the resulting current is at most 40 nanoamps. The preamplifier is mounted in close proximity to the diode array and connected via carefully shielded cables to eliminate noise currents due to stray magnetic fields.

The SSLS preamplifier block diagram is given in Figure 20, and Figure 21 shows the timing sequence for charge readout. Each photodiode is precharged to +5V and incident electrons deplete this charge. The output signal is the current required to recharge the diode. Hence, the current to voltage converter output is negative spikes, as shown by V1 of Figure 21.

These spikes are integrated and buffered by the sample and hold (S/H). The two SSLS outputs (even numbered photodiodes on one, odd numbered photodiodes on the other) are combined at the analog multiplexer and sent to the analog to digital converter (A/D).

The A/D is an integrated circuit, 8 bit unit of commercial manufacture and capable of 30 MHz conversion. The 10 MHz readout rate is well within the A/D capability. After this digitization the detected signals are transmitted via 80 MHz fiber optic cable to the normalization and buffer sections of the FEP. Thus, a minimum of electronic circuitry is mounted with the optical package.

71
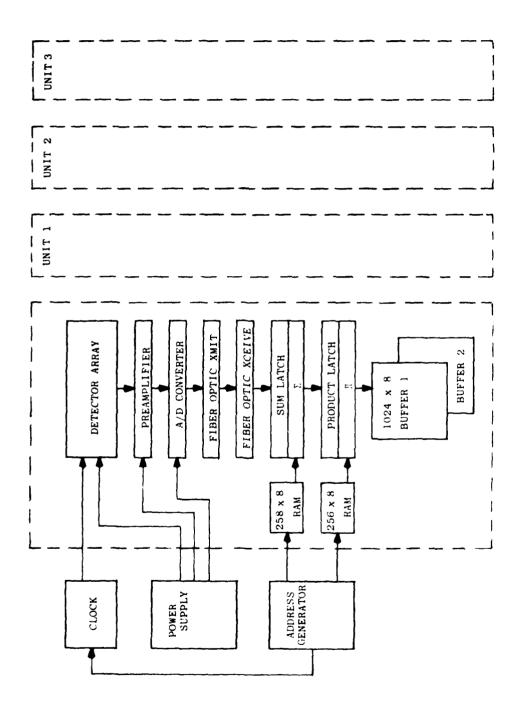
Figure 19. Front end processor.
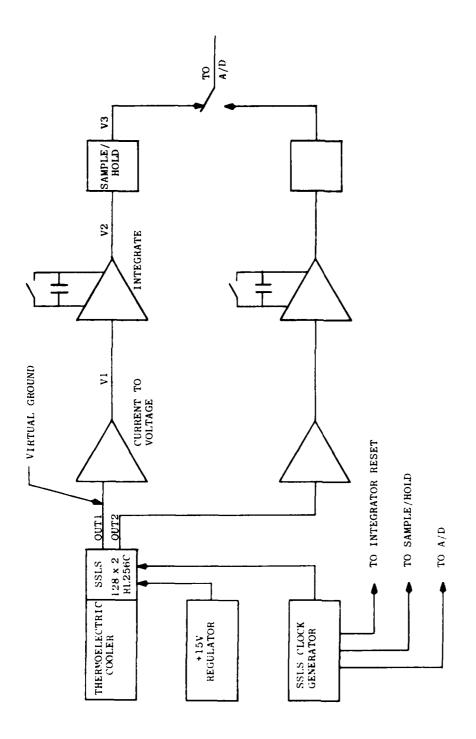
Figure 20. LSI^2 sensor analog electronics.

73
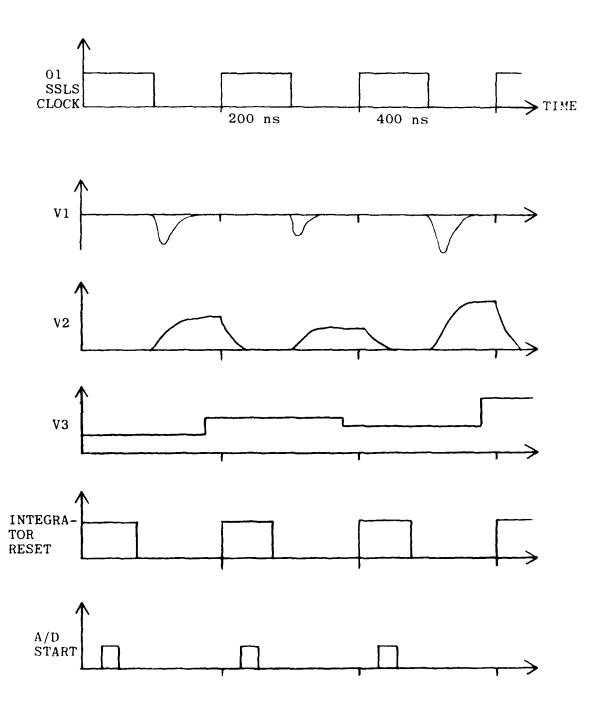
Figure 21. Solid state line scanner preamplifier timing.

74

This minimum circuitry consists of a clock driver
circuit, a +5V regulator, two preamplifiers, two integrators,
two S/H, one A/D, and one fiber optic transmitter per detector
array. The total is approximately 50 integrated circuits which,
with cables, weigh less than a kilogram.

The remainder of the FEP is installed in the same card
cage as the PAP. This remainder consists of 2560 bytes of mem-
ory and two arithmetic elements per detector array. The memory
is organized as two segments of 256 bytes each (one byte per
subaperture) and two buffers of 1024 bytes each (four bytes per
subaperture).

The first 256 byte memory is connected to an 8 bit
digital adder. As each digitized photodiode output is acquired
by the fiber optic receiver, it is latched and the dark signal
contribution is removed. The dark signal for each photodiode
is stored in a separate memory location of the 256 byte RAM.
These RAM constants are determined and loaded by the SSP (see
Section 5.4).

After dark signal subtraction, the new 8 bit word is
latched and the photodiode output is corrected for nonuniform
responsivity of the detector system. This correction is im-
plemented as an 8 bit multiplication using a separate normaliz-
ing factor for each photodiode. The normalizing factors are
stored in a 256 byte RAM and again, the RAM constants are de-
termined and loaded by the SSP (see Section 5.4).

The 8 bit output of the multiplier circuit is stored
in one of the two 1024 byte buffer memories; the other 1024
byte memory is supplying data from the previous nutation cycle
to the PAP. The 1024 bytes are sufficient for 4 samples per
nutation cycle per photodiode (256 photodiodes). The data en-
tering the buffer memory is

$$B(i,k) = R(i)*(P(i,k) - P(i))$$
(19)

75

where $P(i,k)$ is the kth time sample ($1 \leq k \leq 4$) of the ith photodiode, $D(i)$ is the ith dark signal, value and $R(i)$ is the ith responsivity correction constant. Thus, the buffer is filled with the output data of the FEP.

The FEP is a pipeline processor with 6 stages to the pipeline. The first stage is the charge sensitive amplifier and the integrator. The second stage is the S/H unit and the A/D. The third stage is the fiber optic transmitter-receiver. The fourth stage is the dark current removal addition circuit. The fifth stage is the responsivity normalizing multiplication circuit. The sixth and last stage is the buffer memory. Data moves from one stage to the next at 100 nS intervals and hence each photodiode output is amplified, digitized, and normalized 600 ns after readout.

The FEP pipeline is four bytes wide, one byte for each detector array. All four data bytes are processed simultaneously and synchronously; thus a single RAM address generator and a single SSLS clock generator are adequate for all four detector arrays. The digital portion of the FEP (i.e., that portion of the FEP not mounted in the optics package) requires approximately 150 integrated circuits, all operating at a 10 MHz clock rate. All circuits are commercially available.
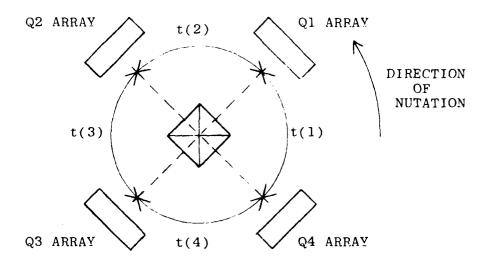
5.3 Programmable Algorithm Processor (PAP)

The digitized photodiode signals must be processed in order to extract the subaperture tip/tilt information. There exist various algorithms for extracting this information (see Section 5.3.2), but all algorithms are similar in that they involve linear combinations of the 16 detected signals (four detectors/ subaperture and four time samples/detector)followed by two ratio computations. The ratio computation (division) normalizes the tip/tilt measurement and hence the final tip/tilt value is independent of optical power. Since all of the algorithms possess similar computation requirements, the Synchronous Centroid Sampling (SCS) algorithm is used as the processor example. Figure 22 illustrates the computation requirements of the SCS algorithm.

Two approaches to algorithm implementation were considered. The first to be presented, full pipeline processing, is straightforward but relatively inflexible. The preferred approach, multiple microprogrammed processors, possesses more complex timing but this is more than offset by the inherent flexibility of microprogramming. Either approach is practical with commercially available circuits.

5.3.1 Pipeline processor.

A fully pipelined processor requires a separate pipeline stage for each arithmetic operation. A pipeline stage consists of a primitive arithmetic function and a data register (latch). Figure 23 illustrates the pipeline implementation of the SCS algorithm computation.

The SCS algorithm requires three primitive arithmetic functions. These are complement (output = -input), sum (output = input1 + input2), and a divide primitive (shift/subtract circuit). Each latch acquires a new data word at 100 ns (10 MHz clock) intervals and all data latches are clocked simul-

(n) is n^{th} ($1 \le n \le 4$) sample period during a nutation cycle.

Q (n) is n^{th} sample from m^{th} ($1 \le m \le 4$) detector array.

Let   S1 = Q1(2) - Q4(2)   1st level
       S2 = Q4(4) - Q1(4)   1st level
       T1 = S1 + S2   2nd level
       S3 = Q2(2) - Q3(2)   1st level
       S4 = Q3(4) - Q2(4)   1st level
       T2 = S3 + S4   2nd level
       XN = T1 - T2   3rd level, x numerator
       XD = T1 + T2   3rd level, x denominator

Therefore

       X = XN $\div$ XD   x tilt

Similarly

       S5 =   Q1(1) - Q2(1)
       S6 = Q2(3) - Q1(3)
       T3 = S5 + S6
       S7 = Q4(1) - Q3(1)
       S8 = Q3(3) - Q4(3)
       T4 = S7 + S8
       YN = T3 - T4
       YD = T3 + T4
       Y = YN/YD

Figure 22. SCS algorithm computation.
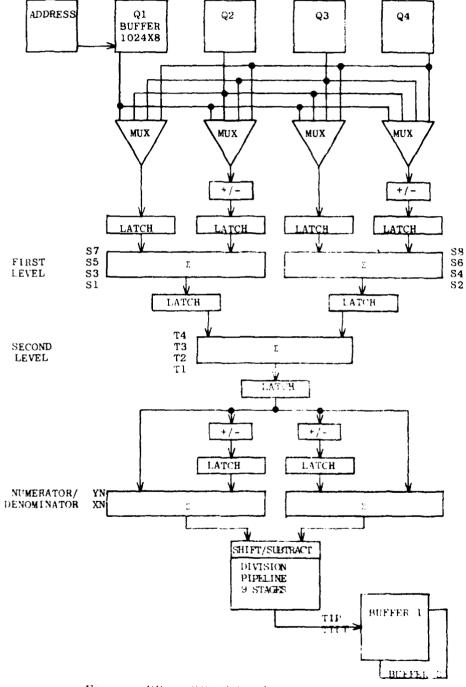
Figure 23. SCS Pipeline.

taneously. Thus, the data for each computational step ripples through the processor as if the data were water flowing in a pipe. The time required for data to pass from input to output is 100 ns x number of pipeline stages, which, in this case, is 13. The first subaperture data is available 1300 ns after the nutation cycle, the second aperture data is available 1700 ns after the nutation cycle, the third is available 2100 ns after the nutation cycle, etc.

After pipeline processing, the data is stored in one of two 512 byte buffer memories; the other buffer memory is supplying subaperture tip/tilt data to the deformable mirror control circuitry. These two buffers interchange their roles at the end of each nutation cycle. The 512 bytes of memory are organized as 256 bytes of subaperture x tilts and 256 bytes of subaperture y tilts.

This pipeline processing technique is the most straightforward approach to algorithm implementation. However, the algorithm is defined by the interconnections of the primitive arithmetic elements, i.e., by the wiring. Even minor changes to the algorithm would require hardware revision and possibly refabrication. For instance, spatial or temporal averaging of the subaperture data would require extensive modifications and additions to the pipeline processor. Furthermore, any averaging implemented by hardwired pipeline processing would involve fixed filter characteristics. Thus, a hardwired filter could not be changed to adapt for differing signal to noise ratios or changing seeing conditions.
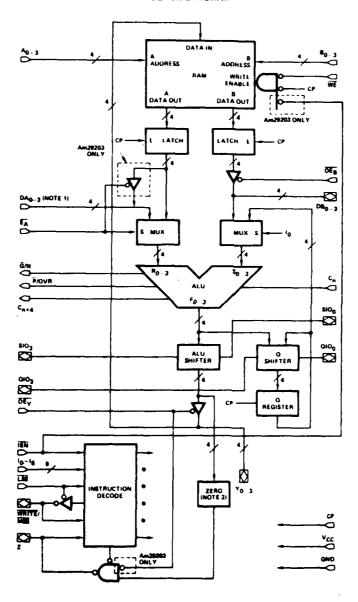
5.3.2 Microprogrammed processor. Flexibility of algorithm definition is a desirable feature for the LSI[3] subaperture signal processor. Commercial bit-slice circuitry has advanced to the stage where microprogrammed arithmetic elements provide a practical mechanism for programmable algorithm definition.

The Programmable Algorithm Processor (PAP) is designed to implement any subaperture signal processing algorithm for which the output signals are a linear combination of the input signals.

The heart of the PAP is the Am29203 four-bit expandable microprocessor slice (See Figure 24). This device is a 48 pin integrated circuit containing 16 storage locations and an Arithmetic Logic Unit (ALU). The storage locations and ALU are equivalent to the latches and primitive arithmetic functions of the pipelined processor. However, the PAP algorithm is defined by a sequence of 32 bit control signals where the pipelined algorithm was defined by wires. The 32 bit control signals (called the microcode) are stored in a RAM and hence the PAP algorithm can be modified by changing the contents of this RAM. Figure 25 illustrates the block diagram of a microprogrammed PAP element.

To illustrate the flexibility of microprogramming approach, consider the implementation of the SCS algorithm. Figure 26 illustrates the microcode required to duplicate the pipeline processor of Figure 23. Each line of microcode requires 100 ns for execution. The entire SCS algorithm (less the division) requires 16 operations or 1600 ns. A 10 kHz nutation, 400 subaperture system requires output at 400 ns intervals, so a full 256 subaperture system would require four arithmetic elements as shown in Figure 25.

81

BLOCK DIAGRAM

Notes 1 DA$_{0-3}$ is input only on Am2903, but is I/O port on Am29203
2 On Am2903, zero logic is connected to Y after the $\overline{OE}_Y$ buffer

Figure 24.   AM2903 bit slice circuit.

82

32 BIT INPUT DATA BUS FROM BUFFER MEMORIES

16X24S253

ISOLATION MULTIPLEXER

1XAm25S558

256
X 8
RAM

2X74367

ISOLATION GATE

32

8

8

8

8

MICROPROGRAMMED BIT SLICE

2XAm2903

ISOLATION GATE

32

ISOLATION GATE

32

32

MICRO-
PROGRAM
256 X 32

8

8

ISOLATION GATE

8 BIT OUTPUT DATA BUS TO BUFFER

5 MEMORIES 256 x 8

3 LSI CIRCUITS

28 MSI CIRCUITS

ALL COMMERCIAL
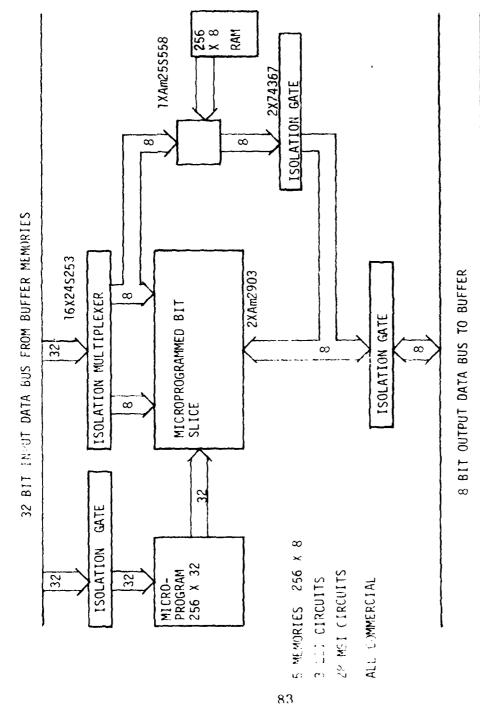
Figure 25. PAP element.

83

$Q_m(n)$ is n^{th} time sample from m^{th} detector array.

Input   R5 =   Q1(1) − Q2(1)   S5

           R7 =   Q4(1) − Q3(1)   S7

           R1 =   Q1(2) − Q4(2)   S1

           R3 =   Q2(2) − Q3(2)   S3

           R6 =   Q2(3) − Q1(3)   S6

           R8 =   Q3(3) − Q4(3)   S8

           R2 =   Q4(4) − Q1(4)   S2

           R4 =   Q3(4) − Q2(4)   S4

(Release input bus)

           R9 =   R1 + R2   T1

           R10 =   R3 + R4   T2

           R11 =   R9 + R10   XN

           R12 =   R9 − R10   XD

           R13 =   R5 + R6   T3

           R14 =   R7 + R8   T4

           R15 =   R13 − R14   YN

           R16 =   R13 + R14   YD

Figure 26.   PAP microcode for SCS algorithm.

Now consider an algorithm change, specifically a derotation as described in Section 6. The pipeline processor would require refabrication in order to implement this function. Two new primitive arithmetic elements (a multiplier circuit and a derotation memory) would be required. The microprogrammed processor would require only a change of microcode, i.e., a softward change. Figure 27 shows the new microcode required to implement the SCS algorithm plus derotation. This new microcode requires 2400 ns, so six arithmetic elements as shown in Figure 25 would be required.

The PAP uses multiple identical programmable processor elements in place of arithmetic hardware dedicated to each subtask of the algorithm processing. The inherent flexibility of programmable processors is easily exploited because new microcode can be loaded in a single nutation cycle. The programmable processors can employ temporal or spatial filter functions, and the parameters of these filters can be changed easily to accommodate the signal characteristics (SNR, seeing, turbulence bandwidth, etc.). The filters could even be changed instantly during a data run simply by switching to a different block in the microcode RAM.

Figure 28 illustrates the PAP architecture. The FEP buffer memories connect to a 32 bit input data bus. The processor elements access this bus sequentially, i.e., P1 acquires the data from subaperture 1. While P1 processes this data, P2 acquires the data from subaperture 2, etc. All processors execute the same microcode, but each processor is out of phase with its neighbors. This arrangement is effectively a pipelined instruction (not pipelined data) architecture because any given microcode step is executed first by P1, then by P2, then P3, etc. By organizing the processors in this manner,

$Q_m(n)$ is n^{th} time sample from m^{th} detector array.

Input	R5 = Q1(1) − Q2(1)	S5
	R7 = Q(4) − Q3(1)	S7
	R1 = Q1(2) − Q4(2)	S1
	R3 = Q2(2) − Q3(2)	S3
	R6 = Q2(3) − Q1(3)	S6
	R8 = Q3(3) − Q4(3)	S8
	R2 = Q4(4) − Q1(4)	S2
	R4 = Q3(4) − Q2(4)	S4

(Release input bus)

R9 = R1 + R2	T1
R10 = R3 + R4	T2
R11 = R9 + R10	XN
R12 = R9 − R10	XD
R13 = R5 + R6	T3
R14 = R7 + R8	T14
R15 = R13 − R14	YN
R16 = R13 + R14	YD

R1 = K1 * R11	K1 = Sin(θ)
R1 = R1 − K2 * R15	K2 = Cos(θ)
R2 = K1 * R12	θ = derotation
R2 = R2 − K2 * R16	
R3 = K1 * R15	
R3 = R3 + K2 * R11	
R4 = K1 * R16	
R4 = R4 + K2 * R12	

Figure 27. PAP microcode for SCS algorithm and derotation.
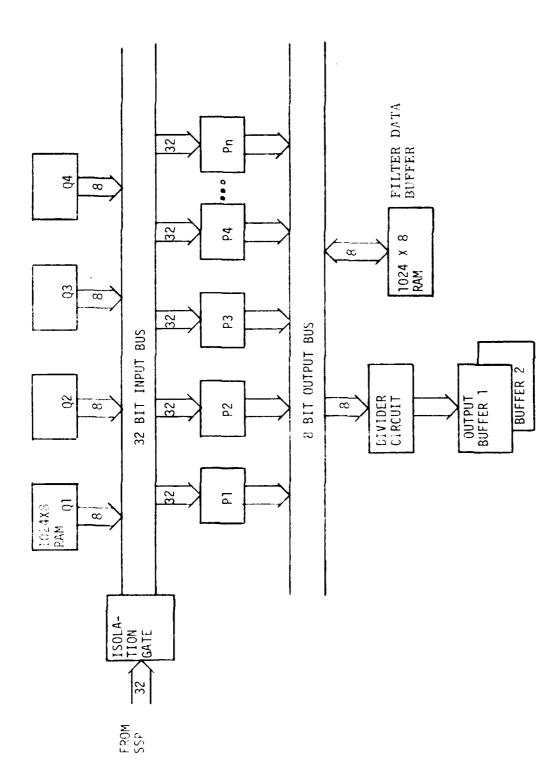
Figure 28. PAP architecture.

87

there is never a condition where two processors simultaneously require the same shared resource (input bus, output bus, etc.). Thus, each processor element is invisible to the other processor elements.

The number of microcoded processor elements required is dependent on the length of the microcode, i.e., the complexity of the algorithm. For 256 subapertures and 10 kHz nutation, the requirement is one processor element per four microcode steps. Eight processor elements identical to the illustration of Figure 25 would be sufficient for 32 microcode steps per subaperture. Programmability makes each element extremely powerful and 32 steps are more than adequate for all algorithms under consideration.

5.4 System Supervisor Processor (SSP)

The SSP supplies general purpose intelligence to the LSI^3 Sensor. The heart of the SSP is a commercial microprocessor, the microNova (see Figure 29). The SSP controls the LSI^3 processor initialization, self test, calibration, nutator mirrors, dynamic subaperture alignment, and autolock.

When the LSI^3 Sensor is turned on, the SSP will download the microcode to the PAP and will download the calibration constants to the FEP. This control information will be used to execute a self test of the processor functions. The full aperture reference LED will be pulses and all detector system elements (thermoelectric cooler, magnetic focus, solid state line scanner, preamplifiers, and A/D converters) will be verified operational.

The SSP will then verify the PAP functionality by applying arbitrary subaperture signals to the input bus and examining the PAP outputs. This test of the FEP and PAP will be
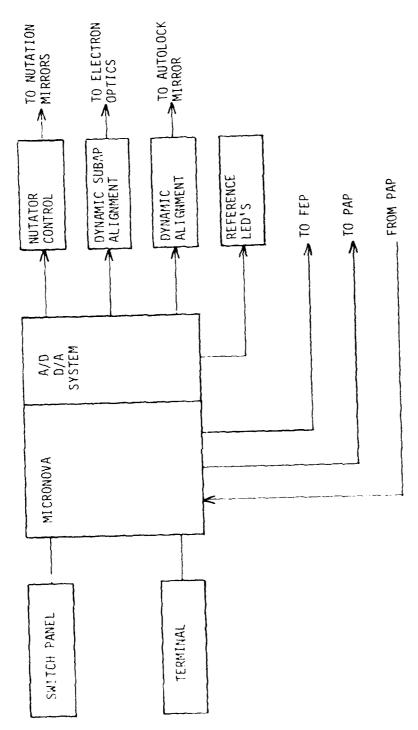
Figure 29. System supervisor processor.

89
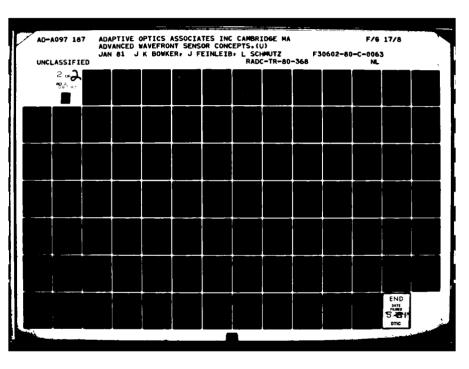
automatic and will require approximately one minute.

If desired, a detector calibration can be initiated. This calibration will use the internal reference LED as an optical source to calculate dark signal and responsivity for each cell of the four detector arrays. The new calibration constants will then be sent to the FEP. A full calibration will require approximately five minutes.
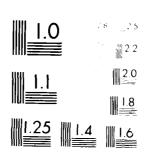
The LSI^3 Sensor will then begin supplying subaperture tilt data. While the FEP and PAP are totally occupied in this task, the SSP is free to monitor the subaperture reference LED signals and will maintain the subaperture alignment using the magnetic deflection elements in the detector arrays. The SSP will also monitor the full aperture reference LED signals and maintain the LSI^3 optical axis alignment using the autolock mirror. The subaperture alignment will not intrude on the wavefront sensing computations; however, the optical axis alignment will involve loss of data for a full nutation cycle. When the full aperture reference LED is pulsed on, the input optical signal is lost. Thus, a nutation cycle is stolen for the dynamic alignment function. A loss of one cycle in 32 would be adequate for 100 Hz dynamic alignment control.

The SSP will also monitor and control the nutation mirrors. The nutation radius can be varied to optimize the signal to noise ratio. It is even possible to use different amplitudes on the x and y nutators for independent optimization. Since the SSP controls the PAP microcode, any tip/tilt scale changes to dynamic nutation control are easily and automatically removed by the microcoded processor elements.

The exact definition of the SSP tasks will change during the LSI^3 fabrication and installation. Nutation and optical alignment parameters are very dependent on the telescope optics.

AD A
097187

The bandwidth required for dynamic subaperture and full aperture alignment is dependent on the telescope mechanics. The self test and calibration procedures may require expansion to include other elements of the overall optical system. Since the SSP functions are defined by micronova programs, the SSP control parameters can be easily modified in software without hardware refabrication. This designed-in flexibility is typical of the LSI^3 signal processing system.

6.0 DETECTOR STUDY

The four detector planes in the LSI^3 sensor are not limited to a specific geometric configuration of detectors, as are the quad cell arrays for the I^3 sensor. Therefore, a wide choice of possible off-the-shelf or special devices may be considered for the detector arrays. The detectors must meet compensated imaging requirements and provide a high speed serial output in order to achieve a configuration with a minimum number of components. High quantum efficiency and a photon limited signal-to-noise ratio can be obtained, in general, only by the use of photomultipliers or similar devices. The high speed serial output sensors that are available and which meet the minimum hardware requirements are the integrating sensor arrays such as the CCD's and self-scanned diode arrays.

The marriage of silicon arrays and intensifying devices would meet the objectives of the program. This is the subject of this study.

The variety of methods of intensification and transferring the resulting charge that is generated to a detector can be categorized by the method of coupling the amplifier to the detector. These categories, including direct (nonintensified) photon detection, are

(1) direct mode: nonintensified direct photon detection (silicon arrays);

(2) electron bombardment (EB) mode: the photo-electron is accelerated 20 kV to 30 kV and strikes silicon, directly creating electron hole pairs;

(3) photon coupled mode: the photo-electrons are amplified in an intensifier and strike a phosphor. The photons emitted are then fiber optically coupled to the array.

(4) Electron coupled mode: the detector array is designed as an array of anodes to collect the current generated by an

intensifier.

(5) Discrete element arrays: this stands for photomultipliers and represents a fall back position that can be used for small arrays for breadboard purposes.

These categories, which will be discussed in detail in the following sections, are illustrated in Figures 30 through 34. The complications are a consequence of applying means to preserve all of the photoelectrons that will be generated at a cathode, or to permit the use of existing commerically available devices. The conclusion of the following study was that the configurations of Figures 31b and c were optimum for the LSI^3 system, and that photomultipliers, Figure 34, would provide a cost effective solution for small breadboard systems.

The quantities required for evaluating the various methods are simple.

(1) Detection quantum efficiency (QE = η): sensitivity of cathode or fraction of photons yielding a photoelectron.

(2) Collection quantum efficiency (η_c): fraction of photoelectron pulses that get to detector.

(3) Noise factor: a consequence of variation of gain in intensifying devices.

(4) Detection noise (η_e).

The phase variance of all of the wavefront sensors including those not studied in this program are given by

$$\sigma_\phi^2 \propto \frac{f(object,sensor)}{(SNR)^2} \qquad (20)$$

In the photon counting limit, $(SNR)^2$ = number of detected photons, N_d, which is given by $N_{total} \cdot \eta\eta_c/F$. Thus, the phase variance is proportional to

93

a. Simple surface channel array.

b. Buried channel with cylindrical condensers.

c. Small fiber area-linear transform.

d. Large fiber transform.

RECOMMENDED DESIGN: DISCRETE FIBER SETS ARE INEXPENSIVE
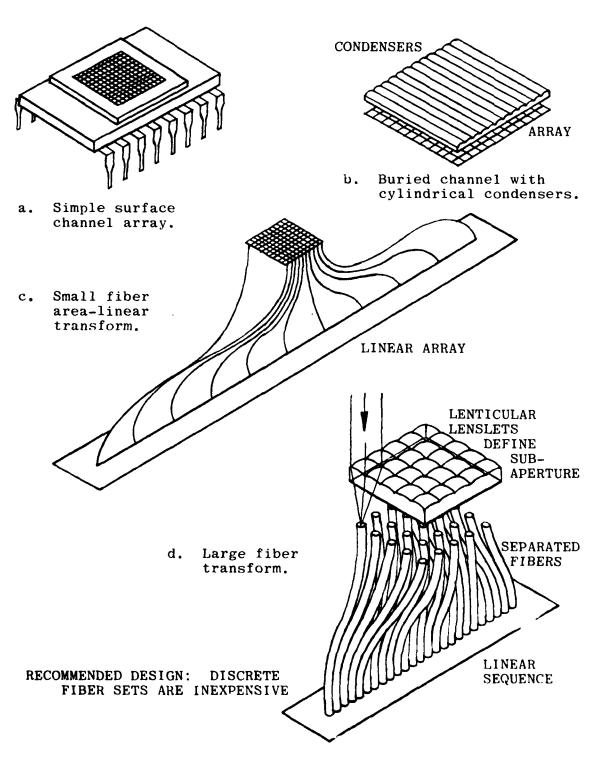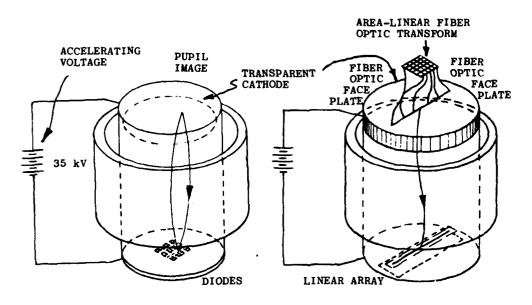
Figure 30. Direct detection coupling

94

a. Area to area image tube.

b. Image tube with linear array.

c. Image tube wtih opaque cathodes.
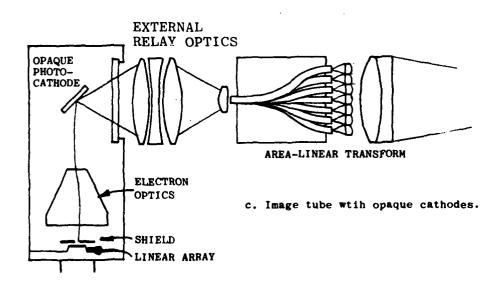
Figure 31. Electron bombardment coupled.
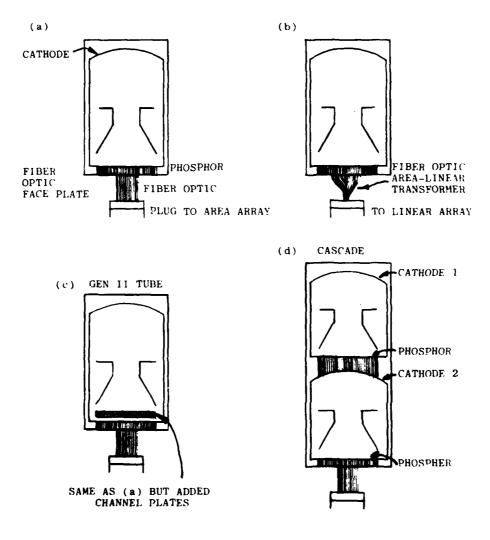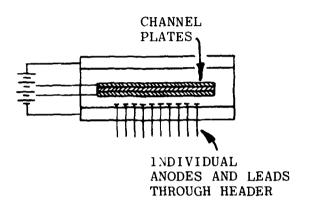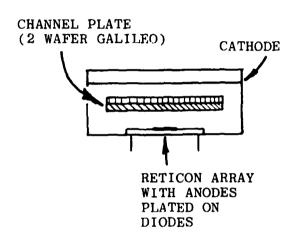
Figure 32. Photon coupled devices.

CHANNEL
PLATES

INDIVIDUAL
ANODES AND LEADS
THROUGH HEADER

CHANNEL PLATE
(2 WAFER GALILEO)

CATHODE

RETICON ARRAY
WITH ANODES
PLATED ON
DIODES
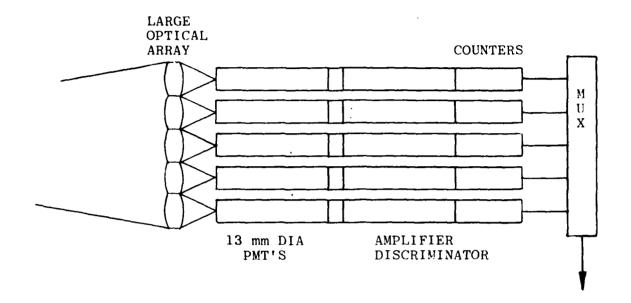
a. ITT multianode array.   b. Reticon array

Figure 33. Anode arrays.

LARGE
OPTICAL
ARRAY

COUNTERS

M
U
X

13 mm DIA
PMT'S

AMPLIFIER
DISCRIMINATOR

21 FIBERS COUPLED TO TUBE

LENSLETS

POTTING
HOLDING
FIBERS

FIBER

PRISM
COUPLING

CATHODE

INTERNALLY REFLECTED PHOTONS
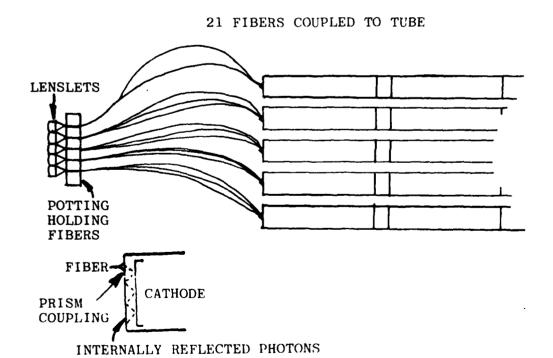
Figure 34.   PMT arrays for breadboard.

98

$$\sigma_\phi \quad \propto \quad \frac{F}{\eta \eta_c} \quad \left(1 + \frac{\eta_e/g}{N_d} \right) \tag{21}$$

where η_e is the number of noise electrons and g is the gain.

Going back to the five sensing systems, we find a basic difference in the sensing employed. In the first category, almost all photosensitive methods are applicable. Basically, however, because of the devices, silicon is the main contender.

In all of the other categories, the same photocathodes are required. Thus, for comparing the last four categories, a simple value of η will be sufficient and it could be ignored or simply set to 1.

Since η is a function of wavelength, the evaluation of detectors in case (1) is complicated by the fact that we must integrate over the bandwidth and consider the effect of wavelength on the measurements.

6.1 Direct Mode Systems

We are concerned here with the efficiency of simple silicon based sensors and will analyze CCD's, the CID and the self-scanned diode array. The possible value of these devices over current photocathodes can be seen by comparing the number of photoelectrons that will be generated. The detector sensitivities and the solar flux as seen through the atmosphere is shown in Figure 35. The total photoelectron count for the different sensors integrated over the spectrum is decidedly better for the silicon array. The result of the integration is given in Table 4.

The plain silicon devices are seen to be five to ten times more productive than the cathodes that provide photoelectrons for intensification.
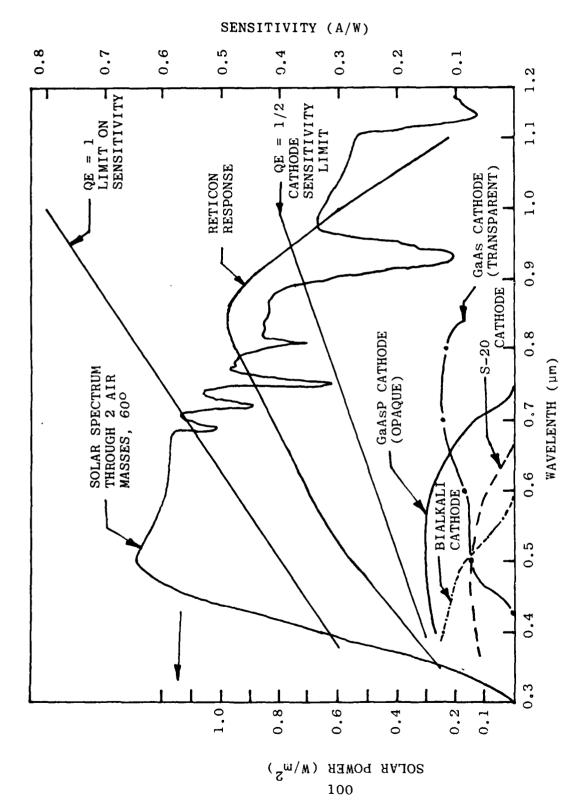
Figure 35. Solar spectrum and detector sensivities.

TABLE 4. INTEGRATION RESULT, TOTAL PHOTO-ELECTRON COUNT.

Cathode	Fraction of Maximum # of Photoelectrons			Tilt Measurements Relative Variance	Relative Phase Variance	Phase @ λ = 550 µm
	$\Delta\lambda$	$\bar{\lambda}$	ε	$1/\varepsilon$	$1/\gamma^2\varepsilon$	
GaAsP (Varian Type s)	0.280	0.550	0.37	2.70	6.92	6.92
GaAs (Varian Type m)	0.44	0.64	0.40	2.51	16.87	22.8
Transparent GaAs	0.34	0.69	0.31	3.21	7.73	12.2
Bi Alkali	0.13	0.465	0.109	9.17	10.62	7.59
GaAsP (cut-off at 0.575)	0.17	0.487	0.228	--	8.00	5.65
Silicon (80% QE)	--	--	1.16	--	--	--

The accuracy of tilt measurements in a quantum limited systems is dependent on object image size and on the resolution of the optics. If the object image width, including diffraction, is approximated by

$$\alpha^2{}_{image} = \alpha^2{}_{obj} + (\lambda/D)^2 \tag{22}$$

where D is the full telescope aperture, and the power received in a measurement with a subaperture L is given by

$$B\alpha_{obj}{}^2 L^2 \tag{23}$$

where B is the brightness, so that the number of photons is

$$B\alpha^2 L^2 \eta/h\nu \tag{24}$$

the variance on a tilt measurement is proportional to

$$\sigma_\alpha{}^2 \simeq \{\alpha_{obj}{}^2 + (\lambda/D)^2\}$$
$$= (h\nu/\lambda BL^2)\{1 + (\lambda/D)(1/\alpha_{obj})\} \tag{25}$$

We find that, if the quantum efficiency is constant for all targets of interest, $\alpha_{obj} > \lambda/D$, the accuracy will improve with wavelength. If the sensitivity is constant, then the number of photoelectrons is $N_e = S \cdot Pd$ and it is important to measure over as wide a spectral band as possible.

The tilt variance induced by the atmosphere is given by

$$(1/2) \langle \alpha \cdot \alpha \rangle = \langle \alpha_x{}^2 \rangle = \langle \alpha_y{}^2 \rangle = 0.975(F/k)^2 \{D_\phi(2a)\}/(2a)^2 \tag{26}$$

where the structure function for the aperture is D (2a) and is given by

$$2.9k^2 r^{5/3} \cdot \int_0^c C_n(z)dz. \qquad (27)$$

The function is independent of wavelength, thus it does not matter what wavelength is used for a wavefront tilt measurement. In a shearing interferometer, where optical phase is measured instead of tilt, long wavelength measurements are less effective than short because the tilt is given by $\phi \cdot \lambda / L$ so that the tilt variance is

$$\sigma_\alpha^2 = (\lambda/L)^2 \sigma_\phi^2 \approx (\lambda/L)^2 (1/N) \qquad (28)$$

The result of this is to reduce the effectiveness of some of the wider sensitivity cathodes. This is shown in the second row of Table 4.

If tilt and phase measuring sensors were to use the same cathode, the other considerations described in Section 3 on performance would apply. The increased capability of a tilt sensor to utilize wide optical bandwidths effectively will produce an improvement in tilt variance by factors of 3 to 5 if opaque cathodes can be used.

Another possibility, if a suitable geometry can be devised, is to use opaque cathodes such as GaAsP (Varian's S-type cathode) which has a quantum efficiency of 40% at 450 μm (theoretical maximum for a cathode is 50%). The relative number of photoelectrons and the improvement in variance are given in the last column of Table 4. The improvement in performance is sufficiently great to warrant consideration of a special tube design.

The silicon devices are still a great deal more
effective. The SNR for CCD's can be quite large for moderate
signals because of the small number of rms noise electrons
that can be expected. Some CCD's have as few as 30 noise
electrons/bucket. The reticon arrays can be held to 800.

The phase variance for a nonintensified diode is

$$\sigma_\phi^2 \propto \frac{\eta_e^2 + N_{Si}}{N_{Si}^2} \tag{29}$$

when N_{Si} is the number of photoelectrons seen by the diode, and
η_e are the noise electrons.

For the intensified diode

$$\sigma_\phi^2 \propto \frac{1}{N_{cathode}} \tag{30}$$

when N_{cat} is the number of cathode photoelectrons. Using the
ratios Si/bi-alkali of 11.5 and 5.28, obtained from Table 4,
we can find the minimum count and rate below which intensifica-
tion is required for various readout noise levels. These are
given in Table 5.

Since the flux for CI objects and similar cathodes
provides from 10^4 counts/sec to 5×10^7 counts/sec, we find
that intensification will be required.

This is not an absolute conclusion, however. At the
low noise levels, the CCD is very competitive. From 10 to 30
noise electrons per sample (NES) have been reported in buried
channel CCD shift registers. In the Fairchild 256 linear array,
noise levels of 150 electrons per charge packet have been
obtained, and, at low temperatures (160 K) at telephone rate
(15 kHz), the NES was about 25.

Consequently, although the present conclusion indicates

TABLE 5

Bi-alkali cathode counts and rates to be exceeded if nonintensified arrays are to be superior (25 μs integration time).

If $^{Si}/_{BiA}$ ratio is

		11.6		5.28	
		Count	Rate	Count	Rate
Best CCD	5	0.21	8 kHz	1.1	44 kHz
	10	0.83	33 kHz	4.4	177 kHz
	30	7.45	298 kHz	39.8	1.59 MHz
	100	82.8	3.3 MHz	443	17.7 MHz
Reticon	300	745	30 MHz	3,980	159 MHz
	1,000	8,282	330 MHz		

a need for intensification, the matter is not entirely closed, and the future development of CCD's should be watched carefully. The comments on CCD geometry in the following section are as relevant in choosing a detection technique as the question of sensitivity.

There is one further consideration; cathodes are improving and it may be possible to obtain 50% quantum efficiencies in the future as the development of III-V cathode materials proceeds. If this happens, cathodes with intensification will be superior.

6.2 Geometries and Processing Requirement

Before discussing the coupling techniques for the EB mode or the photon-coupled mode, a discussion of the geometries of the arrays and the processing required is desirable in order to define how to use them.

The specifications that apply to the devices are simple. Each array must be read out every 25 μsecs in order to provide a complete data set at a 10 kHz rate. The number of elements in the array then are limited by the speed of the device.

High speed devices provide 10 MHz video (and some as high as 25 MHz), consequently, 256 element arrays can be used.

Four different kinds of arrays are to be considered. These are (1) buried channel charge coupled devices, BC-CCD; (2) surface channel charged coupled devices, SC-CCD; (3) the charge injection device, CID; and (4) the self-scanned diode array, SSDA. Some of the characteristics of the first three of these are summarized in Tables 6 and 7.

The devices that are commercially available are relatively large area arrays, 100 x 100, being typically the smallest

TABLE 6. COMPARISON OF SURFACE CHANNEL AND
BURIED CHANNEL*

	SURFACE CHANNEL	BURIED CHANNEL
Limiting temporal noise	Surface trapping > 100 electrons	Bulk trapping > 10 electrons
Limiting pattern noise	Nonuniform background > 100 electrons	Nonuniform dark current, limp, sensitive
Detectivity limit	> 100 electrons	> 10 electrons
Speed limit	< 10 MHz	∿ 25 MHz

TABLE 7. TRADEOFFS BETWEEN FRAME TRANSFER CCD,
INTERLINE TRANSFER CCD, AND CID AREA ARRAYS*

	FRAME TRANSFER CCD	INTERLINE TRANSFER CCD	CID
Versatility	Front or back illumination	Front only illumination	Random read-out, front illumination
Sensitivity	High silicon quantum efficiency	Lower quantum efficiency	High quantum efficiency
Problems	High speed vertical transfer	Complex cell	Pattern noise

---

*D.F. Barbe, "Charge Coupled Device and Charge Injection Device Imaging," IEEE, Vol ED23, 177 (1976).

107

in CCD arrays, and 32 x 32 in the SSD arrays.
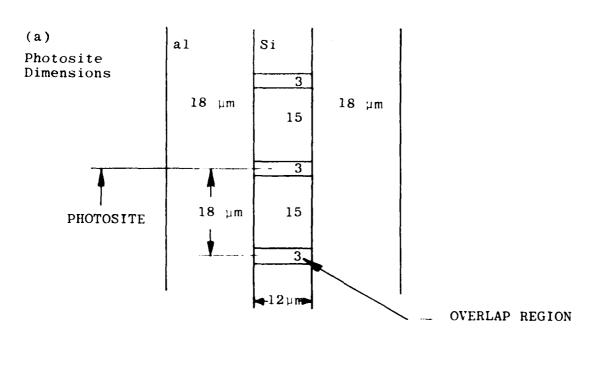
Devices that have as few as 256 elements that can be read out at the required rates are limited to linear arrays.

It is possible to obtain custom arrays at a cost. We have not pursued this except for an anode array discussed below in Section 2 because we found no reason to do so.

The structures of four area arrays are shown in Figures 36, 37 and 38. The first of these is a buried channel CCD, the Fairchild 190 and 244 area imager. Since the photosite region is separated from the transfer lines, the device is relatively inefficient. In this case, the image area is 14 x 16 providing a sensitive area utilization of only 46%. There is a second problem; only every other photosite is read out at any one time. The array is interlaced, all of the even numbered cells "A" are read out in one frame, and then, once the transport channels have been cleared, the other frame would be read out. The result of such a readout would be two sets of data which would have to be processed differently. One set of data would integrate from 0° to 90°, the other from -45° to $+45^O$, then 90° to 180°, and 45° to 135°.

The geometry, providing two cells in one direction and only one cell in the other, is difficult to use because the subapertures are square. Thus, two cells and a blank space would cover one subaperture. On chip addition could be used to consolidate the subapertures. Instead of shifting out all of frame A before reading frame B, one could shift one pulse vertically, then transfer frame B, thus adding A and B into the same bucket. This technique was successfully used by the author in a CCD wavefront sensor for another project.

The readout of a 32 x 16 array could then proceed at a 10 MHz rate or slightly faster to make up for the transfer times.

(a)
Photosite
Dimensions

al | Si

3

18 μm | 15 | 18 μm

3

PHOTOSITE | 18 μm | 15

3

|←12 μm→|

OVERLAP REGION

(b)
Organization
transfer gates

A
B
A
B
A
B

SUBAPERTURE SMEAR
REQUIRED IF DEVICE
TO BE USABLE.

ADD TOGETHER FOR ONE

VERTICAL TRANSFER CHANNEL

HORIZONTAL
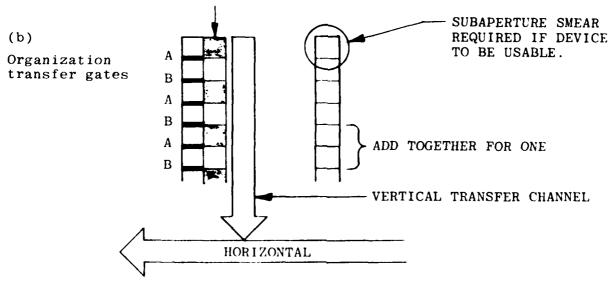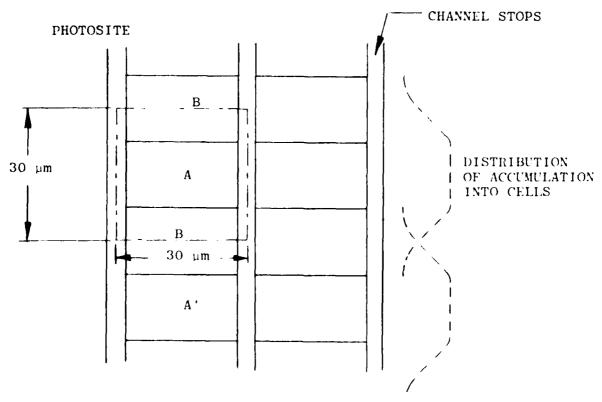
Figure 36. Buried channel CCD structure.

PHOTOSITE

CHANNEL STOPS

B

A

30 μm

B

30 μm

A'

DISTRIBUTION
OF ACCUMULATION
INTO CELLS

A.   ELECTRODS INTEGRATING
B.   ELECTRODS SLIGHTLY NEGATIVE TO DRIVE CHARGE
     TO A OR A'

STRUCTURE (32 x 16 ARRAY)

ACTIVE AREA

FRAME
TRANSFER
32 PULSES

SHIELDED STORAGE AREA

HORIZONTAL
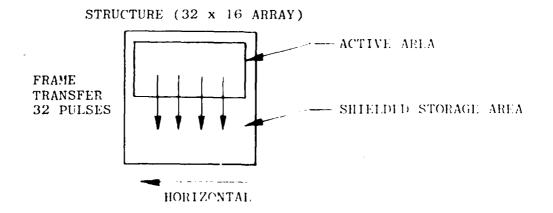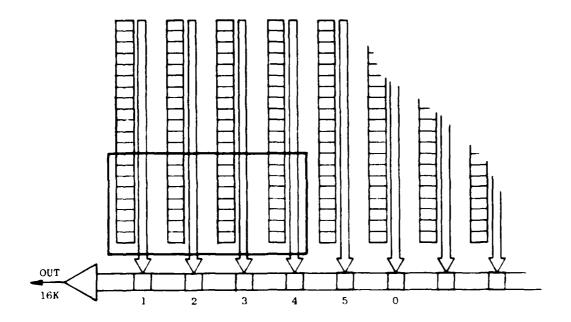
Figure 37.   Surface channel CCD structure.

110
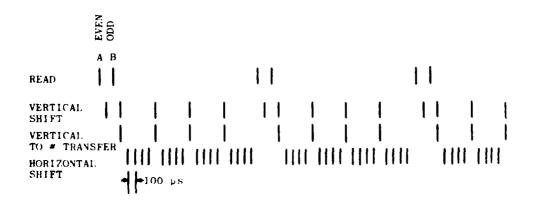
Figure 38. Array array subset readout technique for a
4 x 4 array.

The subaperture areas would be 30 x 36 μm. The transfer of frames A and B would occur just before and after the desired transfer time to average the errors out.

The buried channel device with its capability of adding the contents of a photosite to a transport line bucket and then to read out at high speed allows the array to be used as a smaller array. If only one corner of the array is used, and if a part of transfer pulses are given after 256 vertical and horizontal transfers, then the area observed will be the sum of the sets of 32 x 16 elements that can be extracted. The pulsing sequence is shown in Figure 38 where the method is shown for a 4 x 4 subaperture set out of a 20 x 8 array. The array is masked so that only the lower left hand corner can receive an exposure. All of the other photosites will generate a dark current which would add to the readout and which will need to be suppressed by cooling. The readout sequence is initiated by shifting all of the charge in the even cells into the vertical shift buckets. Then, after one vertical shift, all of the odd cell charges are added to the even cell charges. The next vertical shift brings the line of the first sum into the horizontal buckets. This line is read out using four pulses. At this point, the fifth horizontal bucket is the first position and, on the next vertical transfer, will receive the charge contents of vertical cells 3 and 4. This signal will be added to the dark current from cells 1 and 2 in column 5. If this is small, the addition will be trivial and the result will be as if a 4 x 4 array had been used. There is very little time lost in the process. Three pulses are required for cell addition, 4 for vertical and 16 for horizontal transfers, a total of 23 time increments for 16 elements. In a 16 x 16 array, we still have 3 for addition, 16 for vertical and 256 horizontal shifts, requiring 275 pulses in all. The result is an effective increase

in the cell size by 2X, a reduction in the size of the array at
a trivial cost in speed. The process can be extended to enlarge
the added pixel size further to yield 4 x 3 element subapertures,
for example, but at a cost reduction of 3 in video bandwidth
(but not 12, one dimension being compensated but not the
horizontal), which is fixed by the readout rate.

The smallest Fairchild area array presently available
is the CCD 211 with 244 x 190 elements with 18 μm vertical and
30 μm horizontal spacings. With two-fold additions, the cell
size would be 36 x 30 μm. The collection efficiency is 47%.
The dark current in each output bucket, because of the
repetition addition averages over about 85 elements, is the
same as it would be in normal video use, and would be 0.3% of
saturation.

The Fairchild 244 x 190 device can be driven at 15 MHz.
The second configuration, the surface channel CCD, is that of
the RCA imager. In this device, there seems to be no structure
at all because the photosites are the transfer channels. The
device is 100% efficient because there are no covering elements.

Alternate photosites "A" accumulate the charge. The
intervening photosites "B" are biased slightly negative so that
charges generated in these regions will end up in the adjacent
site A or A'. Normally, the readout is interlaced, A then B,
but there is no need to do this here, as there is in the BCCCD.

The one difficulty in the method of transport is that
if the device is not blanked during frame transfer to the storage
area, charge will be accumulated during transfer, creating a
smear. In a 16 x 16 element array, the smear time will be 1/16
of the frame rate. Such smear may limit phase accuracy in one
dimension because the charges accumulate only in the biased
photosite.

113

The biggest difficulty with the device is that it is slow. The 3 MHz video rate would restrict the device to 75 subapertures or less. Finally, tricks such as those used on the buried channel device cannot be used.

The third device, the CID manufactured by General Electric, and the fourth, the self-scanned diode array made by Reticon, are different from the CCD's in that the photosensitive elements must be addressed sequentially. The entire field cannot be addressed at one time, as it can with the CCD's. The problem with sequential samples is that it places restrictions on the algorithms that can be used. This problem will be dealt with in the next section.

The structure of the CID is shown in Figure 39. The design of a high speed device is shown here. The operation of readout consists of transferring a charge from one capacitor, the photosite, to another, and measuring the displacement current. In the high speed device, the signal charge for a whole line is transferred in parallel to the column electrodes which are then scanned sequentially.

There is a problem of lag due to residual charge if the injection is insufficient. This takes time and is the limiting factor in speed of operation. 5 MHz seems to be the upper limit.

The photosite area of one 32 x 32 array consists of 43 x 43 μm picture elements. This is a slow array, however, because of the capacitance. There is not enough data on available arrays to suitably characterize the device for the AWSC application.

The Reticon self-scanning diode array is schematically shown in Figure 40. Like the CID, each diode is addressed by an x and y gate. The charge is sensed directly, however, and the
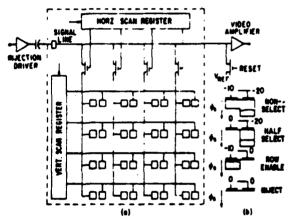
Diagram of basic *X-Y* accessing scheme for a CID imager. (a) Schematic diagram of a 4 X 4 array. (b) Sensing site cross section showing silicon surface potentials and location of stored charge for various operating conditions.

Figure 39.   CID block diagram.

* H. K. Burke and G. J. Michon, "Charge-Injection Imaging: Operating Techniques and Performance Characteristics", Electron Devices, Vol. ED-23, No. 2 (Feb 76), p. 190.

115

*
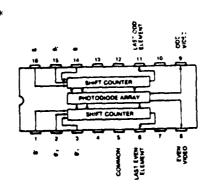
Figure 40. SSDA block diagram, RL-256A.

*Reticon Corporation data sheet 27100

diode is completely discharged. All of the photoelectrons are collected on the diodes which, in the 32 x 32 array, are 100 μm apart. In the area array, the sample rate is 5 MHz. The quantum efficiency is high because there are not surface electrodes which can create reflection losses, as in the CID. The basic problem with the area array is the high video line capacitance of 100 pf. This produces a larger ICTC noise and a NES of about 500 electrons.

The problem with all of the area devices is the unavailability of small arrays. Only the buried channel CCD can be used like a small array. Other than this case, a custom design at an appropriately high cost would be required, which may not be justifiable in terms of the few devices that would actually be used in compensated imaging systems.

There are two linear devices that have 256 elements that can be read out at rates of 10 MHz. These are the Fairchild CCD 110/110F linear image sensor, shown in Figure 41 and the Reticon RL 256S SDDA's, shown in Figure 40. One version of the Reticon C series arrays is expressly designed for electron bombardment.

The CCD photoelement is small, 13 x 17 μm. The Reticon element which has been specially designed for spectroscopy is 25 μm wide center to center, and 430 μm long.

Both devices are equally efficient optically, with all of the photoelectrons collected in the photosite on a diode.

Both devices use two video lines carrying odd and even elements separately. The big difference in the devices is that all of the elements are shifted into the transfer line simultaneously in the CCD array.

In the Reticon device, the diodes are read sequentially so that the integration period of each starts and ends at different point in a nutation cycle.
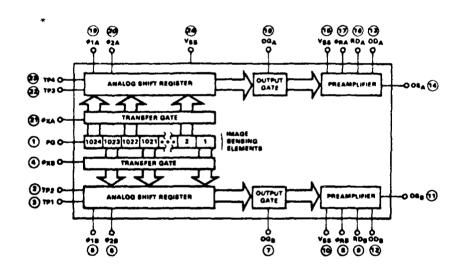
Figure 41. Fairchild linear CCD block diagram.

* Fairchild Semiconductor data sheet 254-11-0005-127 5M
CCD 110/110F 256 element linear image sensor.

6.3 Signal Processing

The basic array options are the two linear arrays, the Fairchild CCD 111, which can be photon coupled, and the Reticon array, which can be used in the EB mode, and one area array. The Fairchild CCD 211, or a CCD 202, a 100 x 100 element array which is not made any more, can be used with the small area sampling technique described above, and would be photon coupled.

The signal processing that would be used for the CCD's would be about the same, whether linear or square, except for the transfer line clocking. In the photon coupling mode, there will be a delay due to phosphor decay, which will affect frequency response. But, this will not affect the use of the array. All readouts will be done together in synchronization with the nutation cycle.

The signal processing for the Reticon array is more complicated because of the fact that the diodes are read out sequentially. This is the major concern. Otherwise, the signal processing is quite similar to the CCD signal processing.

6.3.1 CCD signal processor. The CCD detector selection is governed principally by the data readout rate. For 10 kHz nutation, there are four readouts per photocell per nutation cycle. For 256 subapertures, a 10.24 MHz readout is required. This constraint immediately eliminates surface channel CCD's because the transfer inefficiency increases dramatically above 5 MHz.

The buried channel CCD (BC-CCD) architecture can easily support the 10 MHz readout rate. The potential difficulties in BC-CCD's include dynamic range, dark current, cell uniformity, readout noise, and preamplifier noise. These will be dealt with separately below, using the Fairchild CCD 111 device

119

characteristics. It will be shown that the preamplifier is the principal area of concern.

Dark signal. There are random electron hole generations in the doped silicon used to construct CCD's. These minute charges, called dark signal, are collected in the cells exactly as photoelectrons would be collected. The statistics governing this charge generation indicate that total dark signal is proportional to integration time and is strongly dependent on temperature.

For a 10 kHz nutation rate, the integration time is 25 μs. For a CCD 111 at 25°C, this integration time generates a maximum dark signal of 3.2 x 10^{-4} of V_s, the saturation voltage. This dark signal will halve for each approximately -18°C in temperature.

Cell uniformity. CCD's are fabricated on relatively large (approximately 1.2 mm^2) silicon dies using multiple mask exposures. Large area diffusion inhomogeneities and mask misalignments lead to nonuniform responsivities and nonuniform dark signals for the various CCD cells and photosites. Dark signal nonuniformity in the CCD 111 is a maximum of 2 5% of the saturation voltage. This nonuniformity is not due to time domain statistical fluctuations but rather to device inhomogeneities. Thus, dark signal nonuniformity is removable in real time as a separate dark signal parameter is stored for each cell.

The responsivities of the photosites vary by a maximum of ±6%. Again, this is not a time-varying parameter and hence is removable using a cell-by-cell scaling factor in the signal processor. Using digital scaling with 8-bit accuracy, responsivity uniformity can be reduced to, at most, ± 0.2%.

It should be noted that this scaling will most likely not be necessary. The I^3 sensor measures wavefront tilts relative to an optical reference. The optical path and electronic

processing are identical for the source and reference beams and hence any responsivity scaling factors operate equally on two measurements. If both measurements are scaled or biased equally, then the difference signal will still indicate a proper null for servo control systems. Thus, uncompensated responsivity nonuniformity should have no effect worse than approximately 10% uncertainty in the absolute magnitude of the subaperture tilts.

Dynamic range. CCD dynamic range is specified as the ratio of the saturation voltage to the peak-to-peak noise equivalent exposure. This specification does not take into account the dark signal or the dark signal nonuniformity. For the CCD 111, the typical dynamic range is 500.

The AWSC I^3 sensor will be designed for photon noise limited performance. The microchannel amplifier should amplify the incoming signal to generate at least twice the peak-to-peak noise equivalent exposure for each event, or about 5,000 electrons per photon. This is 8 - 12 times the rms CCD noise signal and hence reliable detection of a single photon is possible.

The dark current and dark current nonuniformity also affect dynamic range. The dark current itself is negligible; however, the worst case nonuniformity of 2.5% saturation voltage results in a dynamic range of 40. This worst case value can be made a negligible 1/2 the noise equivalent exposure by cooling the CCD approximately 60°C to -35°C. Note that typical dark signal nonuniformtiy is 0.5% of saturation. Cooling the CCD by about 18°C to $+7^{\circ}$C will, in general, be adequate to remove all dark current effects from the calculations. This is well within the capabilities of thermoelectric cooling mechanisms.

By removing dark current effects, a dynamic range of 0 - 250 photons is possible within the CCD. The system dynamic range is at least this value times the AGC capabilities

of the microchannel amplifier. With readouts of 40 kHz, this
yields a peak flux of 5 m. The AGC range needs to be only 10:1.

<u>Readout noise</u>. The transfer of charge from one
cell to another is not 100% efficient in a CCD. An electron
left behind by one cell will most likely be picked up by the
next cell, and hence transfer noise is correlated from one cell
to the next but is uncorrelated from one readout cycle to the
next.

Typical charge transfer inefficiencies for BCCD's
are 10^{-5} to 10^{-4}. The total transfer is then $S \cdot N \cdot \varepsilon$ (for
$N \cdot \varepsilon \ll 1$), where S is the total signal, N is the number of
transfers, and ε is the charge transfer inefficiency. The CCD
111 uses two output CCD's for the 256 photosites and hence
N = 130 transfers (the two extra transfers are to move the charge
from the photosites to the CCD's and from the CCD's to the out-
put). Thus, $0.0013 \leq N \leq 0.013$ and for a worst case of $N\varepsilon$ =
0.013 and S = saturation voltage (250 source photons by system
design), the transfer noise of 0.013 x saturation is much less
than the photon noise of $(250)^{-1/2}$ = 0.063 x saturation. For
the photon noise limited system, transfer noise in a BCCD is
negligible.

Another source of readout noise is reset clock
feedthrough in the output charge detector-preamplifier. The
charge detector is a diode which is precharged to a fixed voltage
by a reset clock signal. The diode potential then changes
linearly with the quantity of charge delivered from a CCD bucket.
This potential is applied to the gate of an MOS output transistor.

The desired signal is the difference between the
MOS transistor output during precharge and the MOS transistor
output after the CCD charge has been accumulated. Any change in
reset clock duty cycle or reset voltage will directly affect the
output during precharge and hence this precharge value must be

sensed dynamically.

The accepted method for this dynamic sensing is correlated double sampling (CDS). At 10 MHz, CDS has the disadvantage or requiring accurate capacitor charge-discharge in 25 ns. The Fairchild CCD 111 removes this necessity by supplying an on-chip dummy output which involves a precharge diode and MOS output transistor identical to the on-chip CCD preamplifier. Thus, the reset signal and the output signal are available simultaneously and simple, nonstorage subtraction is adequate to recover the signal. This output structure is a strong positive feature of the CCD 111.

Preamplifier. The CCD 111 is 2.3 cm long by 0.75 cm wide. This results in the two 5 MHz transport clocks and the 10 MHz reset clock being physically very near (approximately 0.2 cm) the sensitive output and dummy output. Capacitive coupling of the high speed clocks to the output is a sever problem. However, this problem can be reduced with good engineering and careful layout; no technological developments are required. The newer 110F has this clock at a different location.

All hardware, even breadboard, will require double-sided printed circuit boards incorporating a ground plane. Isolation etching around output pins will be required. The 1K ohm output impedences will immediately be lowered to approximately 10 ohm using matched pair emitter followers. The output and dummy signals can then be sent to a commerical quality differential amplifier. The approximately 400 µV output noise voltage of the CCD 111 will dominate any diffential amplifier noise. After amplification, the differential signal can safely be sampled and held and converted to an 8-bit digital signal.

6.3.2 Reticon signal processing. This subject must
be considered in two parts, the electronic processing requirements in which much is similar to the CCD processing requirements,
and the algorithm dependent requirements.

The readout requirements of the Reticon 256 element self-scanned diode array are substantially the same as the
requirements for the 256 element CCD. The dark signal effect,
cell to cell nonuniformity, and dynamic range considerations are
identical. The bandwidths and sensitivities of the detector
preamplifiers are also comparable.

The major difference between the CCD and the
diode array is the readout noise mechanism. The CCD suffers
from transfer inefficiency and the diode array does not. However, the high output capacitance (approximately 25 pf) of the
diode array will be a problem at the 10 MHz readout frequency.
The 25 pf capacitance must be totally discharged within 100 ns
and this may require a cooled preamplifier. The preamplifier
must possess an effective input resistance at 10 MHz at less
than 100 ohms.

The effect of sequential sampling on the
algorithms. Because this problem was analyzed before the
optimum algorithm had been developed, only the LSI^3 and MSI^3
algorithms were studied. The analysis assumed a square flat
distribution object, a nutation radius less than the half width,
and a large quad cell. This analysis, which showed that the
sampling techniques created an effective rotation of the coordinate system, also showed that it did not affect the errors.
The MSI^3 algorithm, however, was shown to be defective, and could
not be used if the sampling techniques were employed. The calculation for the optimum algorithm will follow.

In the Reticon arrays, all diodes are
connected to a single video line through gates. These gates

are turned on sequentially, reading one diode charge at a time.
All of the other diodes are integrating while one is being
output. Thus, the output of the nth cell with a light input
$I(t,x)$ where x is the location along the array, is

$$I_n(t_o) = \int_{(n-N)\Delta t}^{n\Delta t} I(t,x)dt \qquad (31)$$

where N is the number of elements in the array and $\Delta t = 1/f$ is
the readout interval. The output is obtained at $t_o = n\Delta t$.

In the use of the I^3 sensor, four readouts
must be obtained for each nutation cycle.

The optical input to the detectors is given
by

$$4\rho \Delta x \sin\theta + 4\rho\Delta y\cos\theta + 4\rho^2\sin2\theta + DC \text{ terms} \qquad (32)$$

where

$$\theta = 2\pi t/T \quad (\text{with } T = \text{nutation period}) \qquad (33)$$

I will assume four arrays operating simultaneously, with the
outputs of cells I - II + III - IV summed as usual.

Three correlating outputs are obtained in
time sequence. These are weighted by

$$++--, \quad +--+, \quad +-+-$$

For the nth detector, the periods are

125

$$(\pi n/2N) \pm (\pi/4)$$
$$(\pi n/2N) + (\pi/2) + (\pi/4)$$
$$(\pi n/2N) + (\pi) \pm (\pi/4) \qquad (34)$$
$$(\pi n/2N) + (3\pi/2) \pm (\pi/4)$$

The integrals are

$$4 \sum_{j=1}^{4} W_j \rho \int_{\frac{\pi n}{2N}+\theta_j-\frac{\pi}{4}}^{\frac{\pi n}{2N}+\theta_j+\frac{\pi}{4}} (\Delta x \sin\theta + \Delta y \cos\theta + \rho^2 \sin 2\theta) d\theta \qquad (35)$$

For different θ's in sequence, the weights in the sum are given by

WEIGHT	0	$\pi/2$	π	$3\pi/2$
$W_j = S_j$	1	1	−1	−1
$W_j = C_j$	1	−1	−1	1
$W_j = 2S_j$	1	−1	1	−1

With the S weight we obtain

$$4 \cdot 2\sqrt{2} \left\{ \Delta x \left[\sin(\pi n/2N) + \cos(\pi n/2N) \right] + \Delta y \left[\cos(\pi n/2N) - \sin(\pi n/2N) \right] \right\} \qquad (36)$$

and with the C weight

$$4 \cdot 2\sqrt{2} \left\{ \Delta x \left[\sin(\pi n/2N) - \cos(\pi n/2N) \right] + \Delta y \left[\cos(\pi n/2N) + \sin(\pi n/2N) \right] \right\} \qquad (37)$$

These can be rewritten as

$$\int S = 16\rho \left[\Delta x \sin(\pi n/2N + \pi/4) + \Delta y \cos(\pi n/2N + \pi/4) \right] = 16\rho \Delta y'$$

$$(38)$$

$$\int C = 16\rho \left[-\Delta x \cos(\pi n/2N + \pi/4) + \Delta y \sin(\pi n/2N + \pi/4) \right] = 16\pi \Delta x'$$

$$(39)$$

As before, the $\int S$ yields the Δy term and $\int C$ the Δx term.

The denominators must now be obtained. First, to obtain the MS denominator, simply apply the 2S weight, which yields

$$\int 2S \rightarrow 16 \rho^2 \sin(\pi n/N) \qquad (40)$$

This is not usable at any angle, but at 0 or $n = N/2$. At the end point it yields a zero. The rate of change of the null is twice as fast as the change in the other terms.

The denominators in the standard I^3 formulation are better behaved. Adding the terms $I + II - III - IV$ for y denominator and using the S weighting, we have

$$\Sigma S_j = 2w_0 \int_{\frac{\pi n}{2N} + \theta_j - \frac{\pi}{2}}^{\frac{\pi n}{2N} + \theta_j + \frac{\pi}{2}} \sin\theta \, d\theta = 2\sqrt{2} \cdot 2 \left[\sin(\pi n/2N) + \cos(\pi n/2N) \right]$$

$$(41)$$

127

$$= 8w\rho \sin(\pi n/2N + \pi/4)$$

Taking the ratios, we have

$$R_x = \frac{\int S(I-II+III-IV)}{\int S(I+II-III-IV)} = \frac{16}{8w}\left[\Delta x + \Delta y \cdot \left(\frac{\cos(\pi n/2N + \pi/4)}{\sin(\pi n/2N + \pi/4)}\right)\right]$$

(42)

The other ratio yields

$$R_n = \frac{2}{w}\left[\Delta y - \Delta x\left(\frac{\cos(\pi n/2N + \pi/4)}{\sin \pi n/2N + \pi/4)}\right)\right]$$
(43)

There is a cross talk induced by the phase of the gates. If we transform the deviations into a coordinate system for each pixel determined by the turn off angle for the gate

$$\chi = \pi n/2N + \pi/4$$
(44)

and the turn on angle

$$\chi = \pi/2$$
(45)

then

$$\int S = 16\rho(\Delta x \sin\chi + \Delta y \cos\chi)$$
(46)

and

$$fC = 16\rho(-\Delta x\cos\chi + \Delta y\sin\chi) \tag{47}$$

The displacements Δx and Δy are obtained by the inverse transformation. Since the ratios

$$R_x = (2/w)(\Delta x + \Delta y\cot\chi) \tag{48}$$

and

$$R_y = (2/w)(\Delta y - \Delta x\cot\chi) \tag{49}$$

we obtain

$$x = \sin\chi \cdot (w/2)(R_x\sin\chi - R_y\cos\chi). \tag{50}$$

Does this change the errors in the measurement?

Since

$$\phi_x = x/\lambda, \tag{51}$$

the phase variance is

$$\sigma_{\phi_x}^2 = (w/2\lambda)^2\sin^2\chi(\sigma_{R_x}^2\sin^2\chi + \sigma_{R_y}^2\cos^2\chi) \tag{52}$$

Since

$$\sigma_{R_x}^2 = \frac{\sigma^2_{\text{num } x}}{D_x^2} \qquad \text{and} \qquad \sigma_{R_y}^2 = \frac{\sigma^2_{\text{num } y}}{D_y^2} \tag{53}$$

129

then

$$\sigma_{\phi_\lambda}^2 = (w/2\lambda)^2 \sin^2\chi (\sigma_{num}^2/D^2)(1 + R^2) \qquad (54)$$

If we normalize the object brightness and integration time, we can express the object size in terms of photon counts. Let this value be $N = vw = w^2$, if square. Since $\qquad (55)$

$$D = 8w\rho\sin\chi = 8N(\rho/w)\sin\chi \qquad (56)$$

The variance on the numerator for this flux is

$$\text{var} \int S(I-II+III-IV) = \int S^2(\sigma_I^2 + \sigma_{II}^2 + \sigma_{III}^2 + \sigma_{IV}^2) \qquad (57)$$

Since

$$\sigma_I^2 = N_I = wv/4 + (w^2/2)(\rho/w)\sin\theta + (v/2)(\rho/v)\cos\theta \qquad (58)$$

Because $S^2 = 1$, it does not matter where the integration begins; consequently

$$\text{var(num)} = 2\pi N = N_T \qquad (59)$$

and

$$\sigma_{\phi_\lambda}^2 = (w/2\lambda)^2 \sin^2\chi \ \frac{N_T}{(8/2\pi)^2(N_T^2)(\rho.w)^2\sin^2\chi} \qquad (60)$$

at the minimum

$$\rho/w = 1/2 \qquad (61)$$

$$\sigma_{\phi_\lambda}^2 = (w/2\lambda)^2(1/N)(2\pi^2/8) \qquad (62)$$

and we find that the **accuracy** is independent of where the sub-aperture is sampled.

The optimum algorithm with CCD and reticon

readout. The optimum algorithm weighting functions are composed of DC and AC terms. This introduces a disparity between DC and AC results because the axis of the AC measurement may be rotated, but the DC axis would not. In order to evaluate this effect, a power dependent calculation must be made.

First, the CCD readout of a nutated square object using an optimum algorithm will be derived and then the algorithm will be modified for the Reticon and the results will be compared.

The actual photon flux N_i on the detectors, following the notation of Figure 42 to define the geometry of a rectangular object with width w and depth v with a brightness B, so that the total number of photons over a nutation period is

$$N_T = \eta Bvw/h\nu = \int_0^{2\pi} \Sigma N_i d\varphi \tag{63}$$

is given by

$$N_1 = (\eta B/h\nu 2\pi) \{ (w/2 + \Delta x)(v/2 + \Delta y) +$$
$$+ (w/2 + \Delta x)(\rho \sin\theta) + (v/2 + \Delta y)\rho \cos\theta +$$
$$+ (\rho^2 \sin\theta \cos\theta) \}$$

$$N_2 = (\eta B/h\nu 2\pi) \{ (w/2 - \Delta x)(v/2 + \Delta y) +$$
$$+ (w/2 - \Delta x)(\rho \sin\theta) + (v/2 + \Delta y)(\rho \cos\theta)$$
$$- (\rho^2 \sin\theta \cos\theta) \}$$
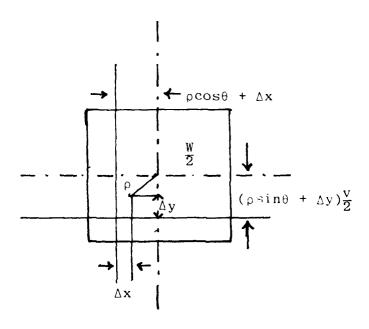
Figure 42. Rectangular object.
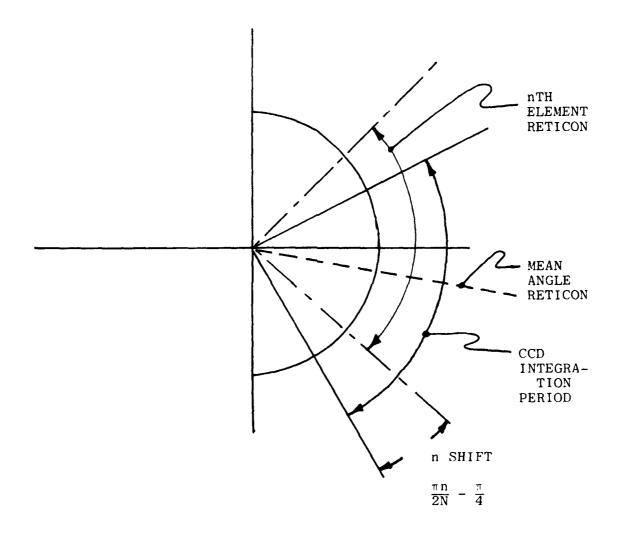
Figure 43. SSD weighting function, $1 + \sin\bar{\theta}$, where
$\bar{\theta} = 0$, $\pi/2$, π, $3\pi/2$. Number of elements = N.

133

$$N_3 = (\eta B/h\nu 2\pi) \{ (w/2 - \Delta x)(v/2 - \Delta y) - (w/2 - \Delta x)(\rho \sin\theta)$$

$$- (v/2 - \Delta y)(\rho \cos\theta) + (\rho^2 \sin\theta\cos\theta) \}$$

$$N_4 = (\eta B/h\nu 2\pi) \{ (w/2 + \Delta x)(v/w - \Delta y) - (w/2 + \Delta x)(\rho \sin\theta)$$

$$+ (v/2 - \Delta y)(\rho \cos\theta) - (\rho^2 \cos\theta\sin\theta) \}$$

$$(64)$$

One set of optimum weighting functions for the numerators and denominators is shown in Table 8.

134

TABLE 8

	for Δx		for Δy
S_{1x}	$= 1 + \sin\theta$	S_{1y}	$= 1 + \cos\theta$
S_{2x}	$= -1 - \sin\theta$	S_{2y}	$1 - \cos\theta$
S_{3x}	$= -1 + \sin\theta$	S_{3y}	$-1 + \cos\theta$
S_{4x}	$= 1 - \sin\theta$	S_{4y}	$-1 - \cos\theta$
and D_{1x}	$= 1 + \sin\theta$	D_{1y}	$= 1 + \cos\theta$
D_{2x}	$= 1 + \sin\theta$	D_{2y}	$= 1 - \cos\theta$
D_{3x}	$= 1 - \sin\theta$	D_{3y}	$= 1 - \cos\theta$
D_{4x}	$= 1 - \sin\theta$	D_{4y}	$= 1 + \cos\theta$

TABLE 9

CCD WEIGHTS

Mean angle	0		90		180		270	
limits of integration	$-\frac{\pi}{4}$ to $\frac{\pi}{4}$		$\frac{\pi}{4}$ to $\frac{3\pi}{4}$		$\frac{3\pi}{4}$ to $\frac{5\pi}{4}$		$\frac{5\pi}{4}$ to $\frac{7\pi}{4}$	
weights	x	y	x	y	x	y	x	y
S_1	1	2	2	1	1	0	0	1
S_2	-1	0	-2	1	-1	2	0	1
S_3	-1	0	0	-1	-1	-2	-2	-1
S_4	1	-2	0	-1	1	0	2	-1
D_1	1	2	2	1	1	0	0	1
D_2	1	0	2	1	1	2	0	1
D_3	1	0	0	1	1	2	2	1
D_4	1	2	0	1	1	0	2	1

In CCD processing the samples are read out whenever the nutation is at a 45° angle and a different weighting is applied to each depending on the mean angle of the integrated sample. Thus, the weights are as shown in Table 9.

Applying these weights to the detector outputs and integrating over a nutation cycle, we obtain the x numerators:

$$\int_0^{2\pi} \sum_{i=1}^{4} N_i S_i = (\eta B/h\nu)\left[2\Delta x v + (8/2\pi)\sqrt{2}\Delta x_f\right] \tag{65}$$

and the denominator

$$\int_0^{2\pi} \sum_{i=1}^{4} N_i D_i = (\eta B/h\nu)(wv + 4\sqrt{2}/2\pi + w_f) \tag{66}$$

so that the ratio is

$$r = 2\Delta x/w \tag{67}$$

Thus, the displacement is

$$\Delta x = rw/2\lambda \tag{68}$$

and the phase is waves is

$$\Delta\phi_\lambda = rw/2 \tag{69}$$

The variance on the phase is

$$\sigma_{\phi_\lambda}{}^2 = (w/2\lambda)^2 \sigma_r{}^2 \tag{70}$$

where the variance of the ratio is given by

$$\sigma_r{}^2 \left[\sigma_{num}{}^2/(\text{Den})^2 \right] (1 + r^2) \tag{71}$$

The variance of the numerator is

$$\sigma_{num}{}^2 = \sum_{i=1}^{4} \int_0^{2\pi} \sigma_{N_i}{}^2 S_i$$

where

$\qquad\qquad\qquad\qquad\qquad\qquad\qquad\qquad$ (72)

$$\sigma_{N_i}{}^2 = N_i = N_t = \eta B v w/h\nu$$

Thus, the phase variance is

$$\sigma_{\phi_r}^2 = (w/2\lambda)^2 \cdot \frac{\eta Bvw/h\nu}{(\eta B/h\nu)^2 - (wv)^2\left[1 + (2\sqrt{2}/\pi) + (\rho/v)\right]^2}$$

(73)

$$= (w/2\lambda)^2(1/N_t) \cdot \frac{1}{(1 + 2\sqrt{2}\rho/\pi v)^2}$$

When this calculation is applied to the Reticon readout, two values are obtained for the AC and DC calculations. The integrations are over the intervals

$$\pi n/2N) \pm (\pi/4) + (I - 1)(\pi/2)$$

(74)

where I is the segment, n the number of the diode and N the number of diodes.

If this is done using the weighting functions described above, the results are discordant.

The DC term is not rotated, but the AC term is. In the case of a square object used here, and using the results of the preceding discussion substituted into the optimum algorithm

138

AC term, we would find

$$r_n = \frac{(2\Delta x v) + \rho(8\sqrt{2}/2\pi)\left[\Delta x \sin(\pi n/2N + \pi/4) + \Delta v \cos(\pi n/2N + \pi/4)\right]}{wv + \left[4\sqrt{2}/2\pi)\rho w \sin(\pi n/2N + \pi/4)\right]}$$

(75)

The result is now complicated not only by ρ but
by shape factors w and v, which in general are unknown. The
rotation cannot be removed easily. If the weighting function
were to contain the phase of the readout location, the derotation
may be obtained before the ratio is obtained. A similar set of
functions to those used with the CCD but the mean angle of inte-
gration would be used for weighting.

The weights are no longer integers and a table
can be constructed similar to the one given for the CCD (refer
to Table 10).

The integrals for each period for the 'x' numera-
tor are
for mean angle 0:

$$\sin\alpha \left[4\Delta x \rho \sqrt{2}\sin\alpha + 4\Delta y \rho \sqrt{2}\cos\alpha\right]$$

(76)

for angle 90°:

$$\cos\alpha \left[4\Delta x \rho \sqrt{2}\cos\alpha - 4\Delta y \rho \sqrt{2}\sin\alpha\right]$$

(77)

for angle 180°:

$$-\sin\alpha \left[4\Delta x \rho(-)\sqrt{2}\sin\alpha + 4\Delta y \rho(-)\sqrt{2}\cos\alpha\right]$$

(78)

TABLE 10

Reticon nth element (x weights)

$$\alpha = (\pi/2)(n/N - 1/2)$$

i =	1	2	3	4
Mean Angle of Group	0°	90°	180°	270°
Integration	$-\frac{\pi}{4} + \alpha,\ \frac{\pi}{4} + \alpha$	$\frac{\pi}{4} + \alpha,\ \frac{3\pi}{4} + \alpha$	$\frac{3\pi}{4} + \alpha,\ \frac{5\pi}{4} + \alpha$	$\frac{5\pi}{4} + \alpha,\ \frac{7\pi}{4} + \alpha$
S_1	$1 + \sin\alpha$	$1 + \cos\alpha$	$1 - \sin\alpha$	$1 - \cos\alpha$
S_2	$-1 - \sin\alpha$	$-1 - \cos\alpha$	$-1 + \sin\alpha$	$-1 + \cos\alpha$
S_3	$-1 + \sin\alpha$	$-1 + \cos\alpha$	$-1 - \sin\alpha$	$-1 - \cos\alpha$
S_4	$1 - \sin\alpha$	$1 - \cos\alpha$	$1 + \sin\alpha$	$1 + \cos\alpha$
D_1	$1 + \sin\alpha$	$1 + \cos\alpha$	$1 - \sin\alpha$	$1 - \cos\alpha$
D_2	$1 + \sin\alpha$	$1 + \cos\alpha$	$1 - \sin\alpha$	$1 - \cos\alpha$
D_3	$1 - \sin\alpha$	$1 - \cos\alpha$	$1 + \sin\alpha$	$1 + \cos\alpha$
D_4	$1 - \sin\alpha$	$1 - \cos\alpha$	$1 + \sin\alpha$	$1 + \cos\alpha$

140

and for angle 270°:

$$-\cos\alpha \quad 4\Delta x\rho(-1)\sqrt{2}\cos\alpha \quad + \quad 4\Delta y\rho\sqrt{2}\sin\alpha \tag{79}$$

and, the sum is

$$8\sqrt{2}\Delta x\rho/2 \tag{80}$$

which is independent of α.

A similar calculation for the denominator yields for mean angle 0:

$$\sin^2\alpha \cdot 2w\rho \cdot \sqrt{2} \tag{81}$$

for $\pi/2$

$$\cos^2\alpha \cdot 2w\rho \cdot \sqrt{2} \tag{82}$$

for π

$$-\sin^2\alpha \cdot 2w\rho \cdot \sqrt{2}(-1) \tag{83}$$

and $3\pi/2$

$$-\cos^2\alpha \cdot 2w\rho(-1)\sqrt{2} \tag{84}$$

with the sum

$$4\sqrt{2}w\rho/2\pi \tag{85}$$

Adding these to the DC terms, we obtain exactly the same result that was obtained with the CCD algorithm.

In conclusion, the use of a Reticon with sequential readout will not affect the results if the appropriate

weighting functions are applied for each diode. What this implies is a look-up table and two multipliers before division. Derotation is not required.

Finally, since the readout angle or axis rotation angles do not appear in either numerator or denominator, the variance of measurement will not be affected by readout angle.

6.4 Input to Arrays: Techniques

With the assurance obtained from the preceding discussions that buried channel two-dimensional arrays, linear CCD's and self-scanned diode arrays can be used, methods of efficiently introducing light to the sensitive elements must be found. Some of these are shown in Figure 30. The buried channel CCD has dead columns and is only 47% efficient. Two strategies are possible. One, shown here, is to use cylindrical condensing elements, either directly to the array or to a cathode which is then imaged on the array. The cylindrical lens elements are only 30 micrometers wide and would need to be made by deposition or by some photoresist technique. If the window to a cathode were 1 mm thick, a SiO_2 deposit only 0.16 micrometers thick would be sufficient to form a lens.

The other technique would be to create big photons by diffusion of an amplified signal so that its width would be equal to the detector subaperture area. This would occur, for example, in photon coupling because of loss of resolution in the phosphor. The result would be an effective overlap of subapertures which, if matched to a deformable mirror influence function, would be an advantage in the accuracy of wavefront reconstruction. The disadvantage would be an increase in the width of the pulse height distribution and consequently an increase in the noise factor of 10 to 25%. The problems will be discussed further under photon coupled systems.

The coupling of the linear arrays to a two-dimensional subaperture area is more difficult. Two options, both of which can be handled by fiber optics manufacturers, are shown in Figure 30b. The first of these is a drawn fiber bundle made of face plate material with 7 micrometer fibers and with a high transmission. The only problem is that no one will use the fine fused materials which would be much smaller than the subaperture size. The coarser materials that manufacturers will use have 50 micrometers or greater diameter cores and substantial cladding, at least equal to the core. This would create a very inefficient bundle. The solution is to go one step further; separate the fibers by a millimeter and provide a 16x16 mm lenticular lens array to input the subaperture field to the fiber. This can be done efficiently. The author has made one such array by milling spherical indentations in copper and then casting a positive in plastic. The result was a precision array of foci which were nearly diffraction limited at f/10.

The other end of the fibers would be arranged in a coherent line 25.6 mm long and the assembly encapsulated. Galileo has given us a budgetary quote for an assembly of $250 each, plus a tooling charge of $250.

We feel that the area to linear conversion is technically reasonable and that it can be done as efficiently as anti-reflection coatings will permit.

The output spacing would be at least 100 micrometers.

6.5   Electron Bombardment Mode

The development of devices which utilize the electron hole pairs generated by absorbing a high speed electron began with beta particle silicon and germanium detectors in the early sixties. The idea of using the method for detecting photo electrons inside an image intensifier originated with Beaver and

McLlwain of U.C., San Diego, and Choissoir of Electric Vision in 1970.[*]

The first device consisted of a cesium antimonide cathode at one end of a vacuum tube and a 38-element diode array at the other. Focusing was magnetic. A potential difference of 20 kV was applied to the tube. Since an electron hole pair is generated for every 3.66 eV loss in the material, the potential number of pairs generated in the semi-conductor will be 5700 if the 20 kV is completely absorbed in the depletion region. Deducting a 3 kV loss in a 1.7 micrometer thick dead layer on the diode the tube had a gain of 4800. Since the tube had a noise component equivalent of 7 keV, single photon initiated events could be detected.

The pulse height distribution for such a device is quite narrow, and the noise factor will be low -- about F = 1.016, because the variance in the number of photoelectrons generated is E/E_O = 4800.

Since the first tube, a large variety of configurations has been built, mostly with arrays of discrete diodes - up to 500 in the case of the space telescope detector.

There has been a large number of attempts to introduce scanned arrays into intensifiers. So far, however, there seems to have been only one successful solution. The structure of silicon array devices is complicated and includes conductors, insulating layers and active elements. The diodes in the early tubes were relatively unaffected by the bombardment, since there was nothing in the focal plane except diodes and conductor leads through the header.

---

[*]"A Digital Multichannel Photometer", Edward Beaver and Carl McLlwain, Rev. Sci. Inst., 42, 1321.

The complicated devices contain switches, electrodes, clock circuitry, etc., all of which would be permanently affected by the creation of electron hole pairs inside them.

The first problem that was solved was to find a way to prevent contamination of the silicon devices by the alkali metal cathode material. This was first successfully accomplished by Electron Vision, and then by a variety of firms, including ITT, The methods are described in their literature.

The most important question of all is whether the arrays can survive direct electron bombardment. In photon imagery, the photons create hole pairs only in absorbing media such as silicon, and travel through transparent insulators and electrodes without effect. The electron beams, on the other hand, crash through the materials leaving a trail of electron hole pairs everywhere.

The resulting ionization becomes trapped at insulated interfaces, causing increases in leakage currents, creates fields that must be overcome by increasing gate voltages which must get progressively greater until the limits of the materials are exceeded. Experiments with buried channel devices which are directly exposed show that at 10^5 rads/cm^2 they become unusable. This value, translated into the compensated imaging exposure levels of 100 photons/cycle/subaperture, would be reached in 1.8 minutes. Most of this failure is incurred in the electrode transport line structure. Things may be better if these channel are protected by very heavy aluminum barriers 10 micrometers or more thick. The life in this case could be extended to 3 hours.

Because of this, considerable effort has been expended to create thinned CCD's which can be exposed through the base. The expectation is that the exposure will be confined to the silicon depletion layer below the electrodes. Leakage currents still increase, however, and measurements show that leakage reaches 6% of saturation at 4×10^9 electrons/pixel. This is

not bad and is about 10^4 better than the front side illumination. But, the device in the CIS environment would be completely dead in 1.8×10^4 minutes and would be unusable for weak targets (one photon/cell) after three hours of the moderate exposure.

The only devices that have survived the radiation are the discrete diode and the shielded linear Reticon self-scanned diode arrays. This is because there are no electrodes -- just a conductor -- to lead the charge out to the protected gates.
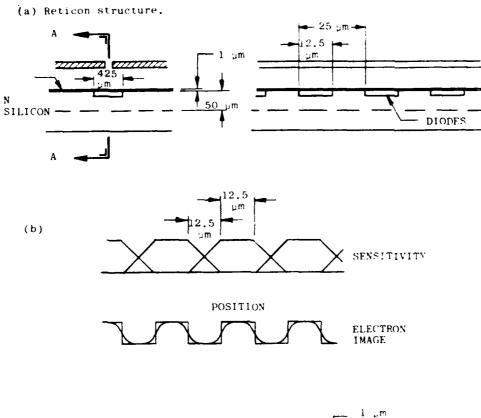
The reason this device would work and a shielded CCD would not is due to the structure of each photosite, diagrammed in Figure 44.

In the Reticon, there is a simple pin junction forming a diode which is protected by a 1 microcmeter thick layer of SiO_2. Above this is a mechanically separate metal shield which is easily aligned because the diode widths are 425 to 600 micrometers.

The diffusion region, in which electron hole pairs can be created and whose charge will be accrued to the junction, is 50 micrometers deep. This permits the use of up to 77 kV electrons. The SiO_2 layer on top is normally 3 micrometers, but Reticon will process the arrays to provide the thinner layer for electron detection.

In the lateral directions, the 12.5 micrometer diodes are separated by N type silicon so that electrons which are created in this space between will flow to both junctions, dividing the current between them in proportion to the distance to them. This creates an overlapping sensitivity between the diodes, as shown.

This spreading can provide an advantage if it matches the influence function of a preceding adaptive optical element. Unfortunately, the spreading is one-dimensional and continuity from element to element at the edges of the input array requires

(a) Reticon structure.

(b)

SENSITIVITY

POSITION

ELECTRON IMAGE
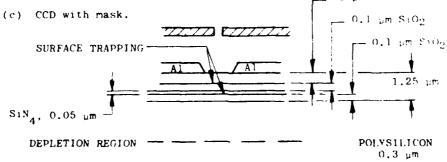
(c) CCD with mask.

Figure 44. Photosite structure.

that the fiber arrangement be uncoiled to a line from the square in a serpentine manner. This organization is exactly what happens when a flat piece of paper (like a wide ribbon of fibers) is folded to form a fan.

The spreading unfortunately will increase the width of the pulse height distribution and, for this reason, should be prevented. The large fiber area linear converter with 50 micrometer cores spaced at 100-125 micrometer intervals will be reduced 4 to 5 times onto the array. The resolution of the electron optics will cause this image to spread. Fortunately, the resolution capability of electron optics is very good, particularly in the small 6 mm long fields considered here, so that the image spots should not spread appreciably. (Poor performance of intensifiers is due to the phosphors as much as anything else.) Cross talk and pulse width increases should be minimized.

The linear CCD's might be treated in the same way as the Reticon, using a thick external shield to protect the transfer lines. The structure of the CCD which is plowed by the high energy electrons, in the second sketch of Figure 44, is composed of a sequence of layers starting with a 1 micrometer SiO_2 insulator, then a 0.3 micrometer polysilicon layer, a 0.05 micrometer silicon nitride electrode, another SiO_2 insulator, and then the depleted region in which the usable electron hole pairs are generated.

This last layer is about 7 micrometers deep, limiting the gain to 7800 and the optimum electron beam energy to 32 kV.

The failure mechanism is surface trapping of carriers between the layers.

The first of the self-scanned linear devices was

obtained by Tull and Nathan[*] at the University of Texas in 1974 and is still operating in the photon counting mode.

The efficiency of the two designs are basically dictated by the photocathode which will be 20% to 30% in our case and 40% in the other. The difference in optical bandwidth will make the opaque photocathode three times as efficient as the other design. This is worth the cost of providing a complex input optical lens.

---

[*]"The Self Scanned Digicon," Tull, Choisser, Snow, Applied Optics, 14, #5, May 1975.

6.6 Photon Coupled Systems

A variety of image intensifier tubes and optically
coupled solid state image device configurations are shown in
Figures 32a-e. The basic device, Figure 32a, consists of a sim-
ple intensifier with a fiber optic plate on the output. This
is coupled directly to the solid state array by a fiber optic
plug. The array is assumed to be a buried channel device be-
cause that is the only configuration that can be made to operate
like a small array at high speed by the technique described in
Section 6.4.

The resolution of intensifiers is often the result of
a trade-off. The efficiency of the phosphor increases with
thickness because higher energy electrons can be used. On the
other hand, the resolution decreases with thickness because of
multiple scatter. The relatively low resolution that results
can be used to advantage in the AWS as a means of creating photon
initiated blobs which can be large enough to bridge over the
opaque areas above the CCD transport registers. In consequence,
if the resolution is matched to the CCD subaperture cell size,
at least 50% of the photon induced signal will be detected. In
consequence, the quantum efficiency will not be reduced but the
noise factor due to a wide pulse height distribution will in-
crease.

The size of the Fairchild CCD elements in the 190 x
244 array are 18 x 14 micrometers. The added pair plus the
opaque region yields a subaperture size of 36 x 30 micrometers.
The resolution of typical image intensifiers, ranging from 20 to
50 1/mm, is compatible with this subaperture area.

The fraction of photons which is emitted by a phosphor
and which emerges from the tubes is quite small because of frus-
trated internal reflection at the final glass/air surface. Loss-
es from the electron beam side are prevented by thin aluminum

coating on the phosphor. If n is the index of the phosphor, the fraction of photons that can escape at all angles from an aluminized tube is $1/n^2$.

Since the index of refraction for most phosphors is quite high, only a small fraction can escape. This is avoided by fabricating the phosphor as a powder. The particles then scatter the emitted photons until they are scattered into the face plate. As a result, up to 45% of the light in an aluminized tube can be emitted over a full hemisphere. If this output were coupled to the array by f/1 optics, the total efficiency would only be 4.5%. The use of fiber optics to optically couple the arrays to the tube and avoid internal reflection losses increases the efficiency dramatically. The face plate must be an Extra Mural Absorption (EMA) type (fibers imbedded in a black matrix) to preserve resolution; the transmittance of a D-14 type with 6 micrometer fibers from a Lambertian source is 45%. The spectral transmittance to the array cuts off at 0.4 micrometers (@42%) and is gone at $\lambda = 0.35$ micrometer. This is shown in Figure 45.

The simple structures of the photon coupled arrays are then fairly well represented by Figures 32a and 32b. In the first, described above, there is a simple cathode, then a fiber face plate to an area array. The second is identical but uses a fiber area linear transformer to a linear array. The area linear transformer must be made of very fine 6 micrometer or less fibers, however. Manufacturers that were contacted did not feel that this was reasonable. The feasible area linear transformer would be made of large fibers (50 micrometer core) with substantial cladding creating 100 micrometers center to center spacing. Such a large bundle is incompatible with direct connection to an array. The third design with the transformer up front with a lenticular lens array for efficient input, is pre-
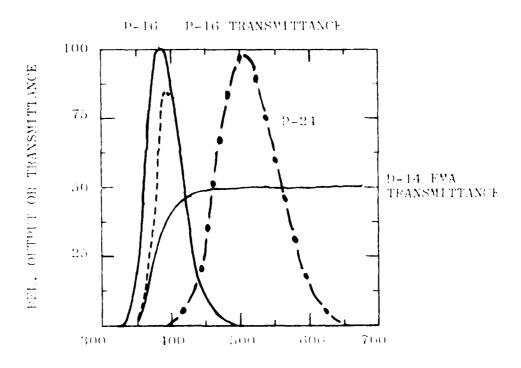
Figure 4.5. Phosphor spectral output and fiber
optics plate transmittance.

ferred. The intensifier electron optics provides the necessary change of scale to the small linear array.

None of these designs provide much gain; however, 30 to 50 luminous gains are typical for single stage tubes; consequently second generation intensifiers or cascaded tubes in Figures 32c or 32d are desirable.

The basic problem of the second generation tube is the fact that the microchannel plate has a fairly coarse structure which has opaque regions and only 65% of the primary photoelectrons get amplified. This direct loss of quantum efficiency should be avoided, and thus a cascade arrangement with a low gain Gen I tube preceding the Gen II tube to provide a fat photon pulse is desirable. There are severe problems in the use of microchannel plates which will be reviewed in the next section, and this use is not recommended.

The preferred photon coupled design uses an array, and two stages of gain. The low resolution precludes the use of detectors with small elements, 30 to 40 micrometers being as small as practical.

The last question to be studied is whether phosphor decay affects the measurements of tilt in a nutating image.

In the case of time delayed sampling, which is a consequence of the use of self scanned diode arrays, the resulting effect was equivalent to a rotation of the coordinate system. This deviation was corrected by the use of a weighting function that included the rotation of time delay angle.

There is a difference between time delay and phosphor decay because a delay is well defined, while decay introduces a smear.

The effect on the signal can be derived simply by using the square uniform object, and by separating AC and DC terms

in numerator and denominator, as before. Assuming a simple decay so that the output of the processor using the simple integrator weighting functions is given by the convolution

$$\int_0^\infty \alpha e^{-\alpha t}\left[4\Delta x\rho\sin\omega(t-t') + 4\Delta y\rho\cos\omega(t-t') + 2\rho^2\sin2\omega(t-t')\right]dt'$$
(86)

where α is the decay constant. The convolution yields the I^3 sum

$$\sum_I = (4\alpha\Delta x\rho/\alpha^2 + \omega^2)(-\alpha\sin\omega t + \omega\cos\omega t)$$

$$+ (\quad " \quad)(\alpha\cos\omega t + \omega\sin\omega t)$$

$$+ (2\rho^2\alpha/\alpha^2 + 4\omega^2)(\alpha\sin\omega t - 2\omega\cos\omega t)$$
(87)

If this is evaluated by the I^3 weighting and applying the appropriate integrals

$$\int C = \int_0^\pi - \int_\pi^{2\pi}$$
(88)

for the y deflection and

$$\int S = \int_{-\pi/2}^{\pi/2} - \int_{\pi/2}^{3\pi/2}$$
(89)

for the x deflection we obtain

$$f\Sigma C = \frac{16\rho}{1 + (\omega/\alpha)^2}\left[\Delta y + (\omega/\alpha)\Delta x\right] \tag{90}$$

and

$$S = \frac{16\rho}{1 + (\omega/\alpha)^2}\left[-\Delta x + (\omega/\alpha)\Delta y\right] \tag{91}$$

The coordinate axis rotation is given by the ratio of nutation frequency to decay frequency.

The denominators for fc and fs weightings become

$$\frac{8w\rho}{1 + (\omega/\alpha)^2} \quad\text{and}\quad \frac{8v\rho}{1 + (\omega/\alpha)^2} \tag{92}$$

so that the I^3 ratios are

$$r_s = (2/w)\left[\Delta x - (\omega/\alpha)\Delta y\right]$$

$$\text{and} \tag{93}$$

$$r_c = (2/v)\left[\Delta y + (\omega/\alpha)\Delta x\right]$$

The values for Δx and Δy are given by

$$\Delta x = \frac{w}{2\left[1 + (\omega/\alpha)^2\right]}\left[r_s + (\omega/\alpha)r_c\right] \qquad (94)$$

The variance on the measurement of tilt is

$$\sigma_{\Delta x}^2 = \frac{w}{2\left[1 + (\omega/\alpha)^2\right]}\left[\sigma_{r_s}^2 + (\omega/\alpha)^2\sigma_{r_c}^2\right] \qquad (95)$$

$$\sigma_{r_s}^2 = \sigma_{r_c}^2 = (\sigma_{num}^2/D^2) = (N/2D^2)$$

where N is the total number of photons. In terms of N,

$$D = \frac{N}{2\left[1 + (\omega/\alpha)^2\right]} \qquad (96)$$

Thus

$$\sigma_{\Delta}^2 = (w/2)^2(2/N)\left[1 + (\omega/\alpha)^2\right] \qquad (97)$$

The consequences of the smear caused by decay is an increase in the variance. It simply means that the contrast of the signal is lower. There is one problem here; the persistence of cathode-luminescence is not generally simple. The decay curves for these fast phosphors are shown in Figure 46. These are the P16-P15 and P24. All of these are best described by two time constants so that the intensity is described by

$$I = Ae^{-\alpha t} + (1 - A)e^{-\alpha 2 t} \qquad (98)$$
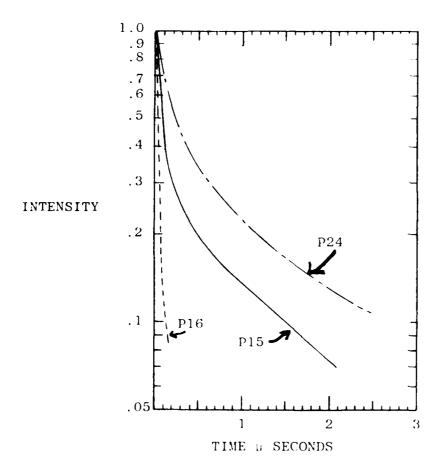
Figure 46. Phosphor decay curves.

For the P16,

$$\tau_{1.5} = 0.028 \ \mu s \quad \text{and} \quad \tau_{2.5} = 0.09 \ \mu s \tag{99}$$

So that

$$\alpha_1 = 24.8 \times 10^6 \quad \text{and} \quad \alpha_2 = 0.77 \times 10^6 \tag{100}$$

$$\text{and } A \simeq 0.75$$

The P15 and P24 are both zinc oxide. The P15 has a UV compo-
nents, but the P24 does not and emits entirely in the blue green.
Its time constants are

$$\alpha_1 = 6.93 \times 10^6 \tag{101}$$
$$A \simeq 0.75$$
$$\alpha_2 = 0.77 \times 10^6$$

Most of the emitted energy is in the second term, since

$$E_{total_1} \propto A/\alpha_1 = 0.11 \tag{102}$$
$$E_{total_2} \propto (1 - A)/\alpha_2 = 0.33$$

The magnitude of the rotation term for the P24 $\frac{\omega}{\alpha}$ for 10 kHz nu-
tation is 0.082. This is small enough so that a modification to
the weighting function could be used to remove the mean rotation

angle. The fact that the proportion of light from each decay mode is a function of temperature and beam intensity is not crucial because the rotation angle is so small.

The P16 decay is faster but half the UV light will be lost in the fiber optic plug. This is illustrated in Figure 45 where the relative brightness of the P16 and P24 phosphors are shown.

The second curve for the P16 shows the effect of absorption in the fiber optic face plate. The relative losses in the UV at the CCD further reduce the value of the P16 output. In consequence, the P24 is preferred, in a two tube cascade, coupled to an area CCD.

6.7 Electron Coupled Mode

The development of the microchannel plate, which is a honeycomb of electron multiplier tubes, increased the gain of image intensifiers immensely and permitted the development of adequate single stage and proximity focus devices.

The device provides current rather than voltage gain. Thus, a sensor can simply collect the current rather than provide the means of converting the high voltage to current and then collecting it as well. The configurations are shown in Figures 33 A and B. The first of these consists of a parallel array of anodes in a proximity focus microchannel plate intensifier. This tube is manufactured by ITT and is probably the only device that can be obtained without any more special effort than changing the pattern of anodes. In this device, the anodes would be 0.9 mm square plates with 0.1 mm separation. Each anode is led through the ceramic header to a pin.

The electronics for each anode would consist of a 100 MHz amplifier discriminator and a counter. The counters would

be buffered and read into the processor in serial stream.

The second version uses a self scanned diode array in which each diode is covered by an aluminum plate. This would be a Reticon device similar to the SSANACON[1] that flew on Voyager as a part of a UV spectrometer.

The anodes in this second device are very small, 0.1 mm square with 0.01 mm gaps between them.

The final electrons out of the MCP with about 100 eV have too little energy to penetrate this device and there is little possibility of damage.

The gain that can be obtained is high, 10^5 to 10^7, and there is little question about the value as a photon counting detector. The possibility of obtaining an array was explored with EG&G Reticon, and they proposed a 16 x 16 element device using 16 parallel channels of 16 anodes in each. The channels would be read at 1 MHz in parallel, providing a 16 MHz overall data rate. The budgetary estimate for a dozen of these arrays with nonrecurring costs included would be 100K and with delivery 9 months after receipt of order.

Closer analysis of the characteristics of microchannel plates revealed some critical problems. These are

  1. Life

  2. Slow response

A microchannel plate consists of a honeycomb glass structure with a secondary emissive coating on the channel surfaces. The structure is formed by three glasses with different viscosity.

During the drawing and fusing steps the outer glass, or

---

[1] The SSANACON – a self scanned anode array with a mocrochannel plate electron multiplier. A, L. Broadfoot, B. R. Sandel, APPLIED OPTICS.

cladding glass, glows in such a way that external force and sur-
face tension deform the glass matrix to the final hexagonal
shape. The process of the different manufacturers leads to
slightly different shapes and sizes.

The Galileo MCP's have 12 to 38 μm diameters and open
area ratios of 55%. ITT's MCP's have channels 12 μm in diameter
and an open area ratio of 63%. Only electrons striking the open
area are multiplied; thus, if no other factors modify this, the
quantum efficiency is 55% (or 63%) of the cathode efficiency.
Secondary electron emission from the web faces can increase this
efficiency up to 85%.

One of the problems with the structure is that the pos-
itive ions can be accelerated in the opposite direction. These
will poison the cathode if they are permitted to leave the chan-
nel plate.

The life end point will be between 0.01 to 0.1 C/cm^2.
Under CIS conditions, with 10^6 photons/sec and gains of 10^5 for
photon counting with 1 mm anodes, this would correspond to a life
range of 1.5 hours to 15 hours. In the Reticon anode array, the
lower noise might permit one to run at a 10^4 gain, but the life
would only be 10 minutes to 100 minutes.

To cure this, a thin film is placed over the input end
of the channel plate which prevents the ions from escaping, but
permits the higher energy electrons to pass through. Unfortu-
nately, this decreases the secondary electron flux, reducing the
quantum efficiency. The life is extended by a factor of about
1000. This is marginally acceptable for the large anode array,
but not for the small array.

The second problem, slow response, is even worse. The
microchannel plate behaves just like a photomultiplier, which
uses discrete dynodes. The potential on each dynode is usually

provided by a resister chain. In such tubes, the resistance is chosen to provide sufficient current to the dynodes to handle the signal level. In the MCP, the same situation exists, but the resistance chain is the channel wall itself.

This impedance is high, about 5×10^{14} ohms/channel. In a single plate intensifier with 1000 V across it and a gain requirement of 10^5, the number of pulses that could be generated would be only 125/sec. The effective dead time is 8 millisecs.

There are a lot of channels, however, 5×10^5 per cm^2, so that the maximum flux at 10^5 gain for the 1 mm anode is 6.3 $\times 10^5$, 63 events per nutation cycle, or S/N ≤ 8. With the smaller anode, even if lower gain of 10^4 is usable, the smaller area limits the flux to 6.3×10^4 events, or S/N ≤ 2.5.

Operation near saturation is not reasonable because the responses will be nonlinear. The noise factors will go up, and linearity will be lost.

The MCP is thus seen to be less efficient than other schemes, and cannot take the flux levels anticipated for compensated imaging. These levels, varying from 10^4 events/sec to 5 $\times$ 10^7 events/sec, will generally overwhelm the electron coupled detector using microchannel plates.

The only electron coupled mode that will work and, indeed, the only tried sensing mechanism that can be purchased off-the-shelf, is a photomultiplier array. This is not recommended for the full 256 channel system, but it is recommended for a 21 channel breadboard system.

The basic arrangement is shown in Figure 34. A digital photon counter will be used instead of an analog integrator. The amplifier discriminator will be a single integrated circuit chip. This is followed by a 12 bit counter and a 12 bit buffer. This parallel arrangement will be read sequentially into the pipeline

processor.

The only drawback in the use of PMT's is the slightly lower quantum efficiency that is a result of mass production.

6.8   Recommended Detector Design

There are three recommended designs; two designs use electron bombardment and differ only in the nature of the optical system.   The third design is a photon coupled arrangement.

In addition, the recommended experimental system for twenty-one channels uses photon multipliers because it presents the least expensive way to prove the performance of the sensor and processing techniques.

The three designs are shown in Figures 47, 49 and 50.

The most efficient photocathodes that have been developed are opaque.   Normally, this has prevented their use in image tubes because it is difficult to arrange for parallel conjugate planes, although one device with a Schmidt telescope objective inside an intensifier was used in a UV spectrometer on an Apollo mission.   The occluded center image plane was the cathode.

The fact that the final image on the cathode is linear because the detector arrays are linear permits simplifications, since the arrangement need only provide for parallel conjugate lines.   The cathode can then be narrow and tilted at an angle so that the optical axis and electron imaging axis can be at right angles.

6.8.1   Design 1   Internal Optics EB Mode.   The first
and preferred design uses an elliptical mirror inside of the image intensifier to collect the photons from the fiber optics linear array and to image these back on the closely adjacent photocathode.   The optical element for a very large numerical aperture may be an ellipsoid of revolution about an axis between the line of fiber optic and the GaAs cathode.

The value of this design can be judged by the efficiency of the optical system to collect all of the photons from the fibers and reimage these on the cathode.   Thus, in order
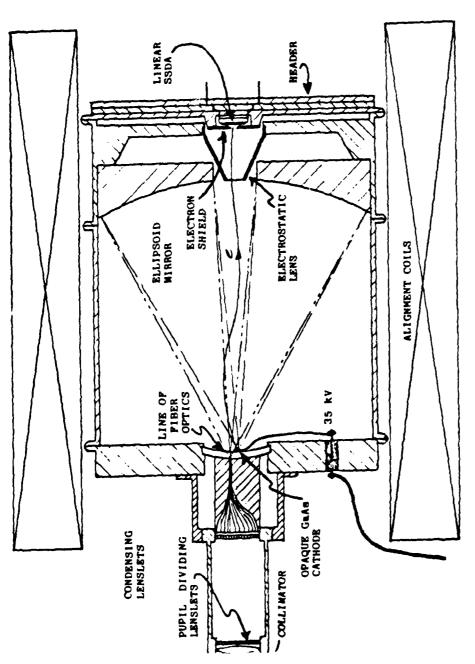
Figure 17. Preferred FB mode detector internal optics.

LOW Na FIBER OPTIC
AREA-LINEAR TRANSFORM

KARL RELAY LENSES

ELECTRON
LENS

GaAs
CATHODE
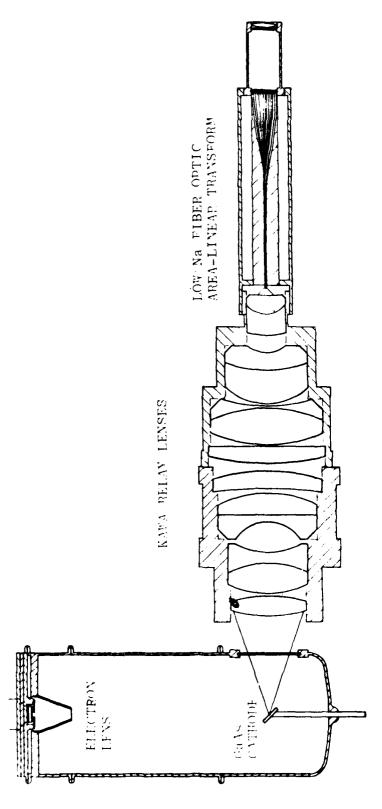
Figure 49.   EB mode detector, external optics.

FIBER AREA-LINEAR TRANSDUCER

CLAMSHELL LENS

SEE FIGURE 50b FOR CLOSE-UP

ELECTRON LENS

Figure 50a. ER detector with clamshell input optics.

GaAs CATHODE, OPAQUE

MIRROR
COATING
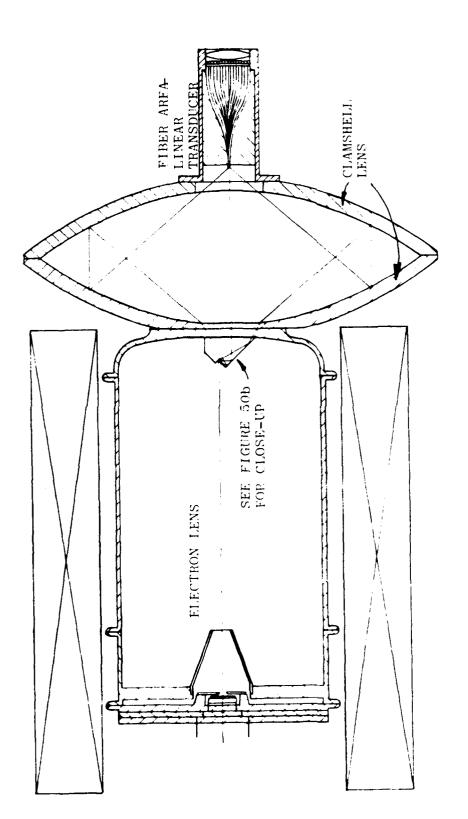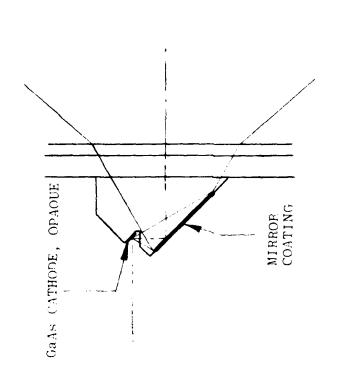
Figure 50b. EB detector with clamshell input optics, close-up.

168

to evaluate the design, we must obtain an estimate of the numerical aperture the optics can handle.

The calculation for the focal plane assumes a curved field, and for simplicity, a spherical element. If h is the distance off-axis of the source point, displaced toward the mirror by a distance δ, and if h' is the image distance or ray intercept from the axis in the plane normal to the axis including the source for unit magnification and if θ is the angle of a ray from the source relative to the axis, the relation for h and h' is

$$(h + h') \left[\cos\theta + \sin\theta \left(\frac{h\cos\theta + \delta\sin\theta}{R} \right) \right]$$

$$= 2h\cos\theta + 2\delta\sin\theta$$

(103)

At *minimum aberration*, $h + h' - 2h$, so that one obtains the curvature of the field
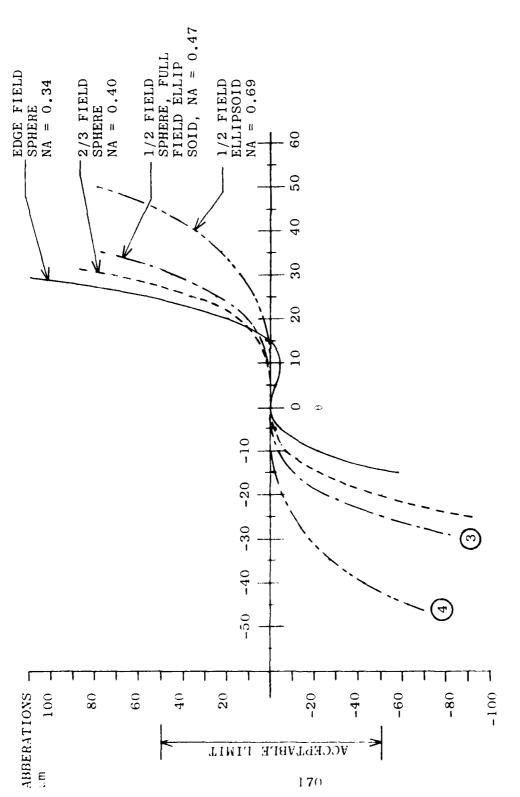
$$\delta = h^2/R$$

(104)

where R is the radius of the sphere. The radius of the focal surface is $R_f = -R/2$, which is typical of spherical mirror systems.

With this field curvature assumed, the aberration for a spherical mirror is given by

$$\Delta h - (2h^2/R) \left[\tan\theta(1 - \frac{h}{r}\sin\theta) - \sin\theta) \right]$$

(105)

The evaluation is given in Figure 18. If the allowed deviation is not to exceed $\pm$ 50 micrometers, which is half

Figure 48. Aberrations of spherical and ellipsoid mirrors
at 1:1 magnification. Field ± 12.8 mm,
radius = 100 mm.

170

the spacing between fibers, then the numerical apertures at the extreme elements h = 12.5 mm and R = 100 mm is limited to NA = 0.34.

At other field positions closer to the center, the numerical aperture increases so that at h = 8.3, NA = 0.40. At h = 6.25, NA = 0.47; at h = 3.125, NA = 0.69; and at the center, of course, NA = 1, since the point is at the center of curvature. This point is not achieved, however, because the fibers and cathode are separated by a few millimeters so that the greatest numerical aperture will probably be about 0.7.

Obviously, better performance can be obtained by using an ellipsoid which provides two fully corrected field points instead of the one that is provided by the sphere. If these points are located at ± 1/4 of the field, then the extreme point aberrations are given by curve 3, and the best points by curve 4. Assume, then, the spherical case gives a good estimate of small deviation errors about a design point. The overall average NA will probably be about 0.60.

This is completely compatible with the optics at the input to the fiber optics, and with the numerical aperture of single fiber elements. If the input to the fibers is constrained to f/2, NA = 0.24; if the fiber NA ~ 0.5 and tight bends are avoided, all of the light from the fibers, except for that lost in the open center of the ellipsoid (NA < 0.06 (a 2% loss) where the electrons go through the mirror), will reach the cathode.

The efficiency of the system, as long as the numerical aperture is ≤ 0.5, is dictated by the antireflection coatings that can be obtained for the wide bandwidth 0.42 to 0.85 μm sensed by the GaAs cathode, which if fully utilized will provide photoelectrons for 40% of the solar photons. The wide bandwidth will prevent the use of very efficient coatings so that one can probably only achieve 98% average transmission per sur-

171

face. Thus, with four lenticular lens surfaces, two fiber sur-
faces, one mirror with protected silver coating, and a 2% loss
through the central hole, the system transmission will be about
84%.

The properties of the design are summarized in
Table 11. The noise factor is low because the variance on the
gain, which is given by the reciprocal number of photoelectron
pairs generated, is small. This is unlike a PMT, where the vari-
ance on gain is given by the reciprocal number of electrons gen-
erated in the first dynode.

With gains ≥ 1000, the noise factor is 1 +
$(1/\sqrt{1000})$.

The biggest problem in the design may be the de-
sign of the electron optics, which must provide a 4X reduction
onto the array and a worst case resolution of 40 1/mm. This
problem has been discussed with Electron Vision and ITT, and
little concern over the problem was expressed--but whether they
realized the full extent of the internal optics or not is uncer-
tain. The present effort has not studied the electron imaging,
and consequently, the design of the electron optics must be con-
sidered a cost problem.

The last element in the comparative table is a
relative net S/N value given by $\sqrt{T \cdot \eta}/(NF)$ where T is the trans-
mission, η the solar spectral efficiency and (NF) the noise fac-
tor.

6.8.2 Design 2 External optics, EB mode. The second
design listed in the table avoids the problem of optics inside of
the image tube, but introduces other problems. The obvious first
solution is to use fast relay optics and this solution is shown
in Figure 49. Kawa relay lenses are shown here because the de-
signs were available. The picture tells all; there are 30 op-

TABLE 11.   RECOMMENDED DETECTORS

DESIGN:	1	2		3	4
MODE	EB	EB		PC	EC
OPTICS	Internal	External		None	None
AREA-LINEAR CONVERTER ARRAY	Reticon linear SSDA	Reticon SSDA		Fairchild CCD	Parallel detector
CATHODE	Opaque GaAs	Opaque GaAs		Trans. GaAs	Bi-alkali
$= \dfrac{\int S(\ )B(\ )d^2}{\int S(OE4)B(\ )d^2}$	0.40	Refractors 0.40	Clam-shell 0.40	0.31	0.11
TRANSMISSION	0.84	0.55	0.79	0.99	0.97
DETECTOR RISK	None	None (all off shelf)		None	None
INTENSIFIER DESIGN DIFFICULTY	Greatest	Medium		None, off the shelf	None
NOISE FACTOR (FAT PHOTON PROBLEM & PULSE HEIGHT DISTRIBUTION)	1.03	1.03		1.2	1.19
COST PROBLEMS	Design of electron optics	Collection efficiency of lenses, chromatic aberrations		Resolution if 3 tubes required	None
NET S/R	0.563	0.455	0.546	0.462	0.27

tical surfaces in all, and if each surface reflects 2%, the transmission would be only 55%. The design of these lenses is probably not compatible with the very wide spectral bandwidths used to obtain full advantage of the GaAs cathode.

The one advantage, though, is that the back focal length is great enough so that the designs of the relay and the electron optics are independent.

Another possibility shown in Figure 50 is the clamshell lens. The device is completely reflective and chromatic aberrations are not present. The numerical aperture of a design which has the input and output in contact with the parabolic surfaces is 0.94. If a space is created so that the output can get through the face plate and be reflected onto the cathode that is tilted, the numerical aperture will be considerably less.

The biggest problem is getting from the clamshell to the cathode. A configuration with the clamshell axis at right angles to the electron tube axis, with the cathode at 45°, would place the large conductive surface at the edge of the electron trajectory, and it is doubtful that the arrangement could be made to work. The other arrangement, as shown, would image directly onto the end of the tube, where a mirror element would direct the light sideways onto the long and narrow photocathode. In order to work, the focused line on the cathode will need to be flat. In consequence, it may be difficult to design the electron optics. Finally, the last right angled bend will restrict the numerical aperture in one dimension. This restriction, as seen in the insert to Figure 50, can reduce the numerical aperture to 0.6. In consequence, although the clamshell has the capability of NA = 0.94, the realization will be no better than the internal ellipsoid configuration.

If this were not enough of a problem, the making of the cathode and the application of the cesium material on the GaAs with the mirror present, masking the areas that need to be clear, may pose practical difficulties. For these reasons, the clamshell is less attractive than the internal mirror design.

6.8.3 Photon coupled system.

The third choice, the photon coupled system, has one major advantage: it does not use an area linear converter and thus has no loss elements before the cathode, except for the tube face itself. The photocathode, however, must be transparent and will consequently be less sensitive, providing only 31% of the possible number of photoelectrons. Thus, in Table 11 the expected flux number is $0.31 \cdot 0.99 = 0.307$, which must be compared to the $0.4 \cdot 0.84 = 0.336$ value obtained from the best EB system.

The big differences between the PC and EB systems is the gain mechanism. The PC system, with a gain of about 25 per stage, will require three cascaded image tubes to produce a quantum limited signal. With this low gain in the first stage, the noise factor becomes significant and will be at least 1.2. In consequence, the net SNR is the least of all of the recommended systems, 0.462 vs. 0.563. Except for the problem of resolution, the system has few problems, and can be put together entirely using off-the-shelf devices.

In the last column of Table 11 an evaluation of photomultipliers with a bialkali cathode has been included. Few photoelectrons are obtained, but the input efficiency can be good. The noise factor will be the worst because of the low voltage to the first dynode; 100 V usually producing 27 secondaries yields a factor of 1.19, thus the net SNR is 0.27.

The conclusion is that the preferred designs all

represent a factor of two gain in SNR and in tilt or phase accuracy over wavefront sensors that must use PMT's to provide an optimum response.

7.0 THE 21 ELEMENT BREADBOARD SYSTEM

The purpose of a breadboard system is to test the concepts and design of a large scale system. The characteristics of the AWS that should be tested are as follows.

(1) The LSI^3 configuration accuracy as a function of photon count, target size and wavelength.

(2) The ability of a single serial processor to produce phase error signal from 256 elements, in 100 μs.

In order to achieve these goals, it is necessary to process that data from only one subaperture if the subaperture data are processed with the same algorithms that are applied to the full array and at the same speed. A 21 element breadboard would not be any more complex, except for more detectors, but it would yield wavefront data that could be applied to a closed-loop system.

The AWS consists of three elements: an optical system, a detection system and the electronic processor. Of these, the design of this optical system is not dependent on the number of subapertures.

The nature of the detection system is the major variable in the design of a breadboard. If the breadboard is to represent a full system and demonstrate its performance, then it should be quantum noise limited. This level of operation can only be obtained by using photomultiplier tubes with noise-free gain, such as those discussed in Section 6.

All of the detectors which are recommended for the full system require some degree of development, and it would be wasteful to implement any of these as a 21 element system, although the crossover might be at approximately 64 subapertures. If a special intensified self scanned disk array is to be designed and built, a 256 element chip may as well be used.

Because of this and because of the cost, it is recommended that
photomultipliers be used in the breadboard The cost per channel
will be relatively high. At $200 per tube, including photon
counting circuit, with four tubes per subaperture, the detector
system cost would be $16,800 for 21 channels. Since no engineer-
ing time would be required to build the tubes, this would
probably be the least expensive system.

The major difference between the use of an intensifier
and an array of PMT's is size. The smallest photomultipliers
are the Hamamatsu R6471 13 mm diameter tubes. These are 13
times larger than the lenticular array lens elements which
serve to divide the pupil in the proposed optical system.
An enlarging optical system could be used instead of the fiber
optical area-linear transducers. The subaperture size for a 21
channel system covering the same pupil area as a 200 channel
system is 3.2 times larger. The size of a detector array is
only 75 mm in diameter and the length, including socket,
resistance ladder network for dynode voltage, preamplifier in
discriminator chip and resettable counter would be about 150 mm
This is about the size of the intensifiers discussed in Section
6. A straightforward enlarging optical system using a conven-
tional eyepiece would not be overly large and would be cost
effective.

An alternate method, providing a better test of the pupil
dividing optics of the full system, would be to use a fiber
optic bundle with lenslets at the input, and then, instead of
bringing the fibers together into a line, spread then out,
taking one fiber to each photomultiplier. These would be
optically coupled to the end windows

If the fiber is coupled to the tube through a small 45^{0}
prism, then a majority of the photons that would otherwise pass
through the semitransparent photocathode would would be inter-

nally reflected, and pass through the cathode material many times as it reflects off both surfaces. This will enhance the real response of the multi-alkali cathodes that can be obtained in the 1/2 inch tubes, so that there is some spectral similarity to the GaAs cathodes to be used in the final system.

The rest of the detection system would consist of an amplifier-discriminator, which can now be obtained in a single chip and provide a 100 MHz maximum count rate, a 12 bit counter and some kind of buffer memory for each tube. These simulate the integrators, the on-chip analog sampling circuits, and the A/D converter. After these circuits, the electronics become identical to the AWS circuit.

The AWS circuitry, described in Section 5, consists of three major elements: the Front End Processor (FEP), the Programmable Algorithm Processor (PAP), and the System Supervisor Processor (SSP).

The FEP is largely replaced by the parallel circuitry of the detector system. The normal buffer in the FEP is a random access memory which can be used because the data is obtained serially regardless of the type of detector -- whether a self-scanned diode array or a CCD. The parallel structure of the detectors permits simulation of the sampling process of the self-scanned arrays or the CCD's by using the approximate timing Because CCD detectors are gated into transfer lines in parallel, simulation of the process will required buffer registers which would then be read out in serial fashion directly into another memory or to the PAP, depending on the algorithm.

In the simulation of self-scanned arrays, parallel buffer registers will not be required, the data being available in a sequence. One buffer for each detector array will be required, however, but this is required in any case in the normal FEP.

The PAP is functionally identified to the full AWS, but

can be smaller because the amount of data is only a tenth as great. In the AWS PAP, four arithmetic units were required in each processor unit to handle 256 subapertures at a 10 kHz field rate. In the breadboard, only one AU will be required. Further, the instruction set in each microprogrammed processor can be larger so that the number of processors can be proportionally fewer. The validity of the PAP is not reflected by the size. The speed of the PAP will, in all cases, be the same.

The System Supervisor Processor will be unchanged in building the breadboard. Once the breadboard has been completed, a large amount of the full system will have been completed. The optics will be done. The detector modules and fiber optics interface elements will simply need to be replaced to turn the breadboard into a 256 subaperture system.

The electronics for the AWS will have been at least half completed at the breadboard stage, and the critical element designs will have been done. The changes in upgrading to the AWS will mainly consist of upgrading the FEP.

The relationship of the breadboard to the full AWS is summarized in Table 12. The major element in building a full 256 element system will be the procurement of the detectors Because of the detector interchangeability, we propose that the breadboard be a little more than a model so that the optics need be done only once.

TABLE 12

ITEM	BREADBOARD	AWS
OPTICS	Full System Complete	
Detectors	4 sets of 21 PMT's (interchangeable sizes)	4 intensified arrays
Electronics		
FEP	Special for parallel PMT's	serial processor for arrays
PEP	$\frac{1}{4}$ full system	full system
SSP	full system complete	
PRINCIPLE COST ELEMENTS	$\frac{1}{3}$ OPTICS $\frac{1}{3}$ PMT's $\frac{1}{3}$ ELECTRONICS	$\frac{1}{2}$ DETECTORS $\frac{1}{4}$ FEP $\frac{1}{4}$ PEP EXPAND

8.0 CONCLUSION

The objective of this study was the evolution of a new sensor concept, the LSI^3 sensor, for potential cost and engineering improvements over the CIS system presently under development. The results of analysis have shown that the wavefront sensor will not only significantly reduce the cost of the sensor system and provide a greatly simplified data processing, but will also improve the performance by a factor of two for low target signal levels. The features of the system include the following.

Detectors: The recommended detector system designed for the 256 subaperture application uses a photocathode electron multiplier tube with direct electron bombardment of a linear self scanned diode array. The detector configuration employs internal reflective optics so that an opaque, wide banded GaAs photocathode can be utilized so that full utilization of available solar illumination in the 0.45 to 0.85 μm band is achieved.

Optics: The optical system as designed is a highly compact, all-reflective system to take advantage of the wide band detector capability. Two small galvanometer nutation devices are the only moving elements in the sensor system. Using a single prism divider as the critical alignment element, and a local reference input, auto-alignment of the system is achievable.

Sensor concept: The LSI^3 sensor makes use of the best features of both DC Hartmann and AC shearing interferometer wavefront measurement systems. The Hartmann technique allows complete utilization of photon for highest plane measurement accuracy for low SNR levels, while the AC shearing interferometer avoids many of the object shape dependencies of the d.c. Hartmann. In the LSI^3, AC modulation is obtained by nutation of the full aperture image on a quad division prism while the measurement uses both AC and DC components in a Hartmann-like quad-cell tilt detection algorithm. And optimizing this algorithm allows

the LSI^3 to achieve a factor of two improvement over the shear-
ing interferometer system.

Processing: The optimized algorithm along with the use of
quantum efficient self scanned detector array system is compati-
ble with high speed serial data processing. Thus, instead of a
processor per channel, as in the CIS system, only 4 flexible ser-
ial processors are required for 256 subaperture measurements.
The measurement update rate is at the nutation frequency of
10 kHz.

LSI^3 sensor design therefore successfully achieves the
goals of the study and is recommended for consideration in all
visible light, large scale image compensation systems.

MISSION

of

Rome Air Development Center

RADC plans and executes research, development, test and selected acquisition programs in support of Command, Control Communications and Intelligence (C^3I) activities. Technical and engineering support within areas of technical competence is provided to ESD Program Offices (POs) and other ESD elements. The principal technical mission areas are communications, electromagnetic guidance and control, surveillance of ground and aerospace objects, intelligence data collection and handling, information system technology, ionospheric propagation, solid state sciences, microwave physics and electronic reliability, maintainability and compatibility.

END

DATE
FILMED

5-81

DTIC